Toward the Direct Detection of Continuous Gravitational Waves from Compact Stars

学位論文

Toward the Direct Detection of Continuous Gravitational Waves from Compact Stars

（連続重力波の直接検出実現に向けた研究）

平成28年12月博士（理学） 申請

東京大学大学院理学系研究科
物理学専攻

枝 和成

Abstract

This thesis is a compilation of the author's study on continuous gravitational waves (GWs) which are long-duration, nearly periodic gravitational waves from a compact star. A rapidly spinning neutron star is believed to be the most interesting emitter of a detectable continuous GW by second generation ground-based interferometric GW detectors. Detections of continuous GWs would give clues to GW generation mechanisms and equations of state of neutron stars that are yet unclear.

First, we focus on a torsion-bar antenna (TOBA) that is a low-frequency terrestrial GW antenna. A unique feature of a TOBA is the ability to explore a low-frequency region inaccessible by the current large-scale interferometric detectors due to seismic noise. We give an overview on a newly proposed multi-output TOBA. Subsequently, we perform a first all-sky search for low-frequency continuous GWs in the frequency range from 6 Hz to 7 Hz using data from a phase-II TOBA that is a prototype of the multi-output TOBA.

Next, we turn to the first Japanese km-scale interferometric GW detector, KAGRA that is now under construction at Kamioka Mine in Gifu Prefecture, Japan. Unlike the currently existing other interferometers, KAGRA will operate in underground and in a cryogenic temperature, which would reduce seismic noise and thermal noise, and thus would provide quiet and stable environment for GW observations. We perform a targeted search for known isolated pulsars with data from the initial KAGRA test run. The main purposes of this study are to validate the search pipeline, to find program-related problems at the early stage, and to prepare for the full configuration operation of KAGRA. And then, we report the results of the end-to-end test for the targeted search and summarize future prospects for continuous GW search using KAGRA.

Finally, we propose a new veto method for continuous GW search for electromagnetically undiscovered sources. Our veto method aims to exclude sharp spectral noise lines that frequently hampers detection sensitivity to continuous GW signals. The main feature of our veto method is the applicability to a single-detector search and coincident lines in a multi-detector network. We conduct performance tests of our veto method using an actual data set from the initial LIGO. We show that the new veto method excludes line noise effectively and improve detection efficiency in noisy data.

Contents

Glossary

Symbol

c	Speed of light	2.99792458×10^8 m/s
G	Gravitational constant	6.674018×10^{-11} m^3/kg/s^2
$M_\odot$	Solar mass	1.9984×10^{30} kg
M_E	Earth mass	5.9722×10^{24} kg
R_E	Earth radius	6.371×10^3 m
R_ES	Distance from the Earth to the Sun	1 AU $= 1.496 \times 10^{11}$ m

Acronym

AU	Astronomical unit
BH	Black hole
BS	Beam splitter
CBC	Compact binary coalescence
CW	Continuous wave
CDF	Cumulative distribution function
DECIGO	DECi-herz Interferometer Gravitational wave Observatory
EM	Electromagnetic
GW	Gravitational wave
IMBH	Intermediate-mass black hole
LAL	LIGO Algorithmic Library
LIGO	Laser Interferometer Gravitational wave Observatory
LISA	Laser Interferometer Space Antenna
NS	Neutron star
MGF	Moment-generating function
PD	Photodetector
PDF	Probability distribution function
SFT	Short-time-baseline Fourier transform
SNR	Signal-to-noise ratio
SSB	Solar system barycenter
TOBA	TOrsion-Bar Antenna

Chapter 1

Introduction

Gravitational-wave astronomy

One hundred years after Einstein predicted the existence of gravitational waves (GWs), the first direct detection of GW was accomplished by the advanced Laser Interferometer Gravitational-wave Observatory (LIGO) during its first observing run [1]. The observed GW signal, GW150914, was emitted from two merging black holes (BHs) with masses of $36M_\odot$ and $29M_\odot$ located at a distance of about 410 Mpc [2, 3]. Subsequently to the discovery of GW150914, the LIGO and Virgo collaborations announced the second GW observation, GW151226, that originated from a binary BH system composed of $14.2M_\odot$ and $7.5M_\odot$ BHs [4].

GW astronomy is expected to provide information much different from and complementary to conventional electromagnetic (EM) one. Since EM waves cannot penetrate dense matter, EM observations enable us to obtain information only on the surface of observed objects. Also, EM waves are vulnerable to absorption and scattering by gas and dust in the interstellar medium during the propagation. In contrast, thanks to weakness of the interaction, GWs can help us explore astronomical phenomena masked by dense matter such as the interior of a supernova explosion, the center of a nebula surrounded by disks of gas and dust, and the inside of a neutron star (NS). Thus, GW astronomy is often referred to as a new window to the Universe [5].

Detectors

The first attempt to directly detect GWs was made by Joseph Weber from the early 1960s [6, 7]. He devised and developed a resonant-bar GW detector composed of a cylinder-shaped aluminum bar with a radius of 1 m, which is called the Weber bar antenna. The fundamental vibrational mode of the resonant bar is excited by an incident GW at or near the resonance frequency of the bar. The GW signals are read out by converting the vibrations of the bar into electric signals with a transducer as shown in the left panel of Fig. 1.1.

After the pioneering work of Weber, concept of a laser interferometric GW detector was devised and developed [8, 9]. GW signals are read out by measuring tiny distance variations between a central beam splitter (BS) and two end test mass mirrors by means

of optical interference effects. As shown in the right panel of Fig. 1.1, an input laser beam is split into two orthogonal beams by the BS, and after bouncing at the end mirrors the two beams are recombined at the BS. Temporal change of difference in the arm lengths due to the passage of a GW is measured by a photo-detector (PD) placed in the direction away from the laser. A laser interferometer is a wide-frequency-band detector for GW and is sensitive to GW at frequencies from tens to hundreds Hz as opposed to a resonant bar antenna. At the present time, several large-scale laser interferometric GW detectors have been constructed or are being constructed around the world, including the advanced LIGO [10], advanced Virgo [11], KAGRA [12], and LIGO-India [13].

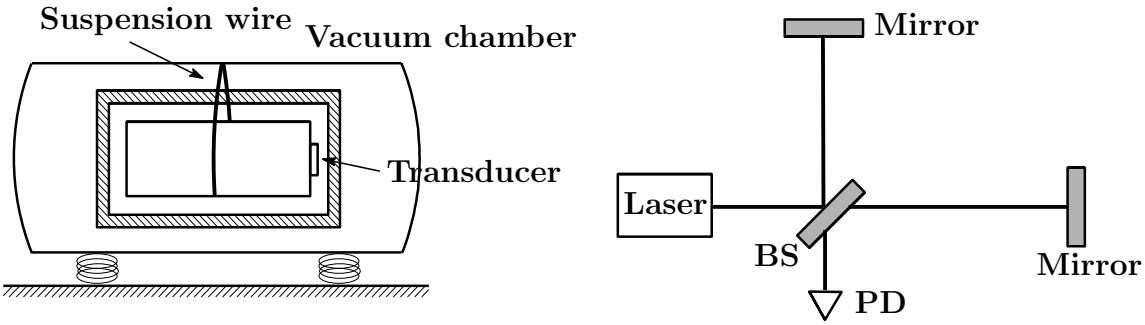

Figure 1.1: The layout of a Weber bar and a simple Michelson interferometer.

Continuous waves

Continuous waves (CWs) are long-lived nearly periodic GWs and are considered to be one of the most interesting detectable targets for GW observations. Such CWs are potentially produced from steadily rotating systems. A rapidly spinning NS is believed to radiate a CW due to some non-axisymmetry around its spin-axis that is detectable by the aforementioned advanced ground-based GW detectors. Also, orbiting binary systems composed of compact stars such as NSs and BHs long before coalescence produce low-frequency CWs although they are inaccessible by the advanced ground-based GW detectors due to seismic noise in low-frequency region.

CW search is generally divided into two classes: a targeted search and a wide-parameter-space search. A targeted search aims to detect CW signals emitted from pulsars that have been already discovered by EM observations. In advance of CW search, pulsar parameters such as the sky position, the spin frequency, and the spin-down rates are already measured electromagnetically. In this case, there are no search parameters and we can perform the most optimal search method. For the Crab and Vela pulsars, previous searches conducted by the initial LIGO and Virgo have surpassed the upper limits on GW strain amplitudes inferred from energy conservation law, so-called the spin-down limits [14]. The advanced GW detectors are expected to beat the spin-down limits for several tens more known pulsars.

In contrast, a wide-parameter-space search aims to detect CW sources undiscovered in previous EM searches. So far, about 2,500 radio pulsars have been discovered by EM observations within our galaxy even though these are only a tiny fraction of all the expected pulsars [15]. In fact, the number of electromagnetically undiscovered pulsars within 5 kpc is estimated to be of the order of 10^{6-7} inferred from the birth rate, part of which are expected to have spin-frequencies within the sensitive frequency band of the current GW detectors [16]. Since source parameters are not known completely, exploring a wide-parameter-space in a brute-force manner is required to extract unknown weak CW signals buried in noisy data, which results in a computationally intractable number of signal templates. Hence, we have to perform sub-optimal search method at the cost of reduced sensitivity. In addition to heavy computational cost, a wide-parameter-space search entails another problem. Sharp spectral noise lines often appear in detector noise and mimic CW signals. Lines would bring about a high-false alarm rate and degrade detection sensitivity. Vetoing unpredictable lines is also one of the central problems in unknown CW search.

Outline of this thesis

This thesis is organized as follows. Chapter 2 briefly reviews CW sources and data analysis methods to extract CW signals submerged in detector noise that will be employed in the next three chapters. In Chapter 3, we focus on a torsion-bar antenna (TOBA) that is a recently proposed terrestrial low-frequency detector. TOBA enables us to explore low-frequency GWs inaccessible by the ground-based laser interferometers because of seismic noise. We give an overview of our paper [17] regarding a multi-output TOBA including short updates. Subsequently, we report the results of all-sky search for low-frequency CWs with a newly developed TOBA based on [18]. In Chapter 4, we turn to the first Japanese km-scale interferometric GW detector, KAGRA. We carry out a targeted CW search using data from iKAGRA test run and validate the search pipeline we have developed. In Chapter 5, we propose a new veto method for a wide-parameter-space search to deal with line noise problems based on [19]. The main feature of our veto method is applicability to a single-detector case and multiple lines appearing in two or more segments. We investigate performance of our veto method using an actual data set from the initial LIGO. Finally, Chapter 6 is devoted to conclusion.

Chapter 2

Basics of CW search method

2.1 CW sources

2.1.1 Pulsar

CW is GW whose amplitude and frequency are nearly constant during observations. A CW is expected to be one of the most detectable interesting targets for GW detections. For ground-based GW detectors sensitive to frequencies between 10 Hz and 2,000 Hz, a main source of CW is a rapidly rotating NS that produces GW due to its non-axisymmetry around its spin axis. There exist various generation mechanisms of CWs: the non-axisymmetric crust of a NS, the non-axisymmetric instabilities inside the NS such as r-mode instability, and the free precession of the NS itself. Because the relation between a spin frequency and a GW frequency depends on its generation mechanism, an origin of a CW from a NS that is already discovered by EM observations can be identified.

A pulsar is considered to be a rotating NS born from a core collapse supernova explosion after the gravitational collapse of a massive star. A typical radius and mass of a NS are 10 km and $1.4M_{\odot}$, respectively, so that its mass density is roughly estimated to be 6.7×10^{14} g/cm^3 assuming uniform density profile, which is comparable to normal nuclear density. Pulsars produce radio emissions at the expense of their rotational kinetic energies. As a result, in addition to the observed spin frequencies, time evolutions of the spin frequencies, namely spin-down rates, are also observed. Figure 2.1 depicts about 2,500 currently known pulsars on a f-$\dot{f}$ diagram that gives plenty information about the pulsar's properties such as magnetic field strengths and pulsar ages. Roughly speaking, pulsars reside in two islands on this diagram. Pulsars occupying the region around $f = 2$ Hz are often referred to as normal pulsars, whereas pulsars around $f = 200$ Hz are called millisecond pulsars. Assuming that all the loss of the rotational energy is due to the magnetic dipole radiations, the strength of B-field and pulsar age can be inferred from $B \propto \sqrt{P\dot{P}}$ and $\tau \propto P/\dot{P}$, respectively[1]. These indicate that normal pulsars have weaker B-field and older ages than millisecond pulsars do. An additional important difference between normal and millisecond pulsars is whether or not they form binaries. While

[1] The pulsar age and the strength of the dipole magnetic field at the pole on the NS surface are

normal pulsars are likely to be solitary, most millisecond pulsars form binary systems as shown in Fig. 2.1.

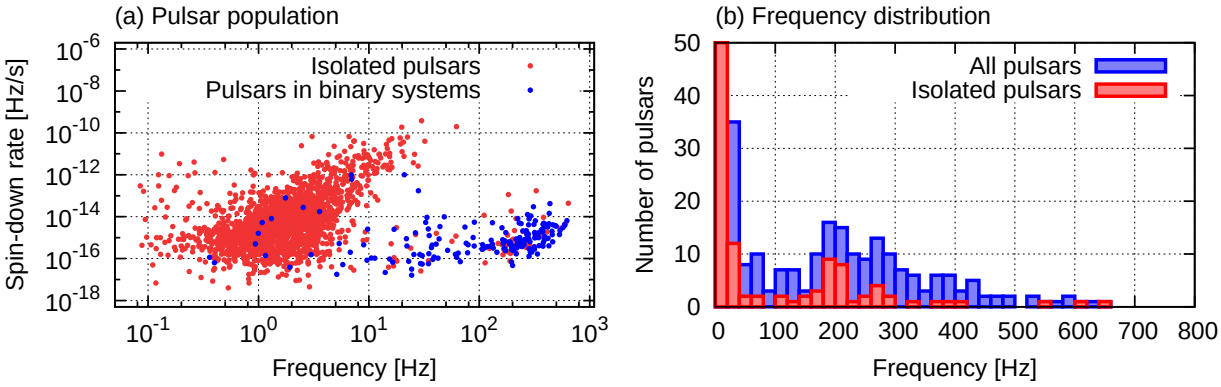

Figure 2.1: Left: f-$\dot{f}$ diagram for pulsars. The red dots represent isolated pulsars and the blue ones represent pulsars in binary systems. Pulsars populate at around $f = 2$ Hz are classed as normal pulsars, whereas pulsars at around $f = 200$ Hz are classed as millisecond pulsars. Right: Histograms for the numbers of all pulsars and isolated pulsars as a function of frequency. Pulsars with lower spin frequencies are likely to be solitary. These data are taken from the Australia Telescope National Facility (ATNF) catalogue [15].

2.1.2 CW sources

Let us consider a rapidly rotating NS to be modeled as a rotating triaxial ellipsoid of a rigid body. If the NS has axisymmetry around its spin axis, no GWs are emitted from it. In contrast, if there exists some non-axisymmetry, this leads to the production of GWs. It mainly originates from non-axisymmetric distortions on the NS surface, non-axisymmetric instabilities inside the NS such as r-mode instability, and free precession of the NS itself. Generally, a non-axisymmetry of the NS around its spin axis is characterized by a single parameter ε called ellipticity, which is related to the NS's principal moment of inertia by

$$\varepsilon = \frac{I_{xx} - I_{yy}}{I_{zz}}, \tag{2.3}$$

estimated to be [20]

$$\tau = \frac{P}{2\dot{P}} \simeq 15.8 \text{ Myr} \left(\frac{P}{1 \text{ s}}\right) \left(\frac{\dot{P}}{10^{-15}}\right), \tag{2.1}$$

$$B = \left(\frac{3Ic^3 P\dot{P}}{8\pi^2 R^6}\right)^{1/2} \simeq 3.2 \times 10^{12} \text{ G} \left(\frac{P}{1 \text{ s}}\right)^{1/2} \left(\frac{\dot{P}}{10^{-15}}\right)^{1/2}, \tag{2.2}$$

respectively, where we assume that the NS's spin-down is caused by the dipole radiation and the spin period at the birth is much shorter than the present value. The radius and the moment are assumed to be $R = 10$ km and $I = 10^{38}$ kg m^2, respectively.

where the z-axis is assumed to align with the spin axis. The parameter ε has information on to what extent NS is distorted around its spin axis. The case of $I_{xx} = I_{yy} = I_{zz}$ corresponds to a spherically symmetric NS. In the case of $I_{xx} \neq I_{yy}$, namely a non-axisymmetric NS, GWs are generated from the NS. In the following, we give a brief review of bumpy NSs, freely precessing NSs, and accreting NSs.

Bumpy NS

A NS is considered to be born as a result of a catastrophic supernova explosion, which would bring some deformation to the NS. Although such a deformation relaxes gradually over time, the NS's crust can sustain the non-axisymmetric deformation at a critical level u_{break}, which is called the breaking strain. Owing to the high density of the NS, the outer crust is considered to form a body-centered cubic Coulomb lattice composed of iron ^{56}Fe nucleus [21]. Non-axisymmetric distortions can be supported by the electrostatic force, or the Coulomb force. The maximum value of ellipticity is roughly estimated to be [22]

$$\varepsilon_{\max} \simeq b u_{\text{break}} \sim 10^{-6} \left(\frac{u_{\text{break}}}{0.1}\right) \left(\frac{\Delta R}{1\ \text{km}}\right) \left(\frac{R}{10\ \text{km}}\right)^3 \left(\frac{1.4 M_\odot}{M}\right)^2, \tag{2.4}$$

where M, R, and ΔR denote the NS's mass, the NS's radius, and the thickness of the crust, respectively. Roughly speaking, the rigidity parameter b is the ratio of the crustal electrostatic binding energy E_C to the gravitational binding energy E_G[2]. Because $E_C \sim \mu V_{\text{crust}} \sim 4\pi\mu R^2 \Delta R$ and $E_G \sim GM^2/R$, the rigidity parameter b scales as in Eq. (2.4), where V_{crust} is the volume of the crust, and μ is called the mean shear modulus whose typical value is 10^{29} J/m^3. Thus, the smallness of $b \sim 10^{-5}$ is due to the fact that the electromagnetic energy stored in the crust is much smaller than the gravitational one in the NS [25]. Whereas the rigidity parameter is relatively well-understood, the breaking strain u_{break} is highly uncertain, beyond which the crust will crack. The maximum possible value of u_{break} in the NS curst is estimated to be around 0.1 by molecular dynamics simulations in [26]. It is widely believed that NSs are composed of a solid crust and a fluid core. On the other hand, some exotic alternatives to conventional NSs that contain solid cores have been proposed. If this is the case, allowable maximum deformation could

[2] This is because the shape of a NS is determined such that the total energy of the NS is minimized. According to [23, 24], NS's total energy is written as a function of ε:

$$E(\varepsilon) = E_0 + \frac{J^2}{2I_0(1+\varepsilon)} + A\varepsilon^2 + B(\varepsilon - \varepsilon_0)^2, \tag{2.5}$$

where E_0, I_0 are the energy and the moment of inertia in a non-rotating spherical case and J is the total angular momentum. The last two terms are related to the gravitational binding energy and the strain energy stored in the crust, respectively. Setting $\partial E(\varepsilon)/\partial\varepsilon$ to be zero leads to $\varepsilon = \varepsilon_\Omega + b\varepsilon_0$, where $\varepsilon_\Omega \equiv J^2/[4(A+B)I_0] \simeq I_0\Omega^2/4A$ is a deformation caused by centrifugal force and $b \equiv A/(A+B) \simeq A/B$ denotes the rigidity parameter.

be much larger than indicated by Eq. (2.4) (e.g. $\varepsilon_{\max} \sim 4 \times 10^{-4}\,(u_{\rm break}/10^{-2})$ for solid strange-quark stars [27] and $\varepsilon_{\max} \sim 10^{-3}\,(u_{\rm break}/10^{-2})$ for NSs with crystalline color-superconducting core [28]). Hence, the maximum possible value of ellipticity depends on the crustal structure and the core equation-of-state. Future prospects for what upcoming GW detectors will tell us about NS's equations-of-state from known pulsar searches are discussed in [29].

Also, strong magnetic field that is misaligned with the spin-axis can sustain the NS's deformation and distorts the NS in a non-axisymmetric manner. When a NS is modeled as a uniform-density star composed only of non-superconducting component, the magnitude of a magnetic distortion can be roughly estimated by a back-of-the-envelope formula [30]:

$$\varepsilon_B \simeq \frac{E_B}{E_G} \sim 3 \times 10^{-13} \left(\frac{B}{10^{12}\ \mathrm{G}}\right)^2 \left(\frac{1.4 M_\odot}{M}\right)^2 \left(\frac{R}{10\ \mathrm{km}}\right)^4, \tag{2.6}$$

where $E_G \sim GM^2/R$ is the gravitational binding energy and $E_B \sim B^2R^3$ is the magnetic energy stored within the NS. Figure 2.1 indicates the estimated magnetic field strength ranges between 10^9 and 10^{12} Gauss under the assumption that NS's spin-down is attributed to magnetic dipole radiation. So, magnetic distortion is not large enough to produce detectable GW signals as is evident from Eq. (2.6). On the other hand, if a NS consists of a type-I superconducting core, the strength of GW signals is estimated to be much stronger [31]. Since magnetic field lines cannot penetrate through the type-I superconducting core, the magnetic field is confined to the crustal region composed of the normal component (see Fig. 5 in [31]), in which case the internal magnetic fields would be much larger than the external magnetic fields. The resulting magnetic ellipticity would be much larger than indicated by Eq. (2.6). Because the internal structure of a NS has yet to be well-understood and also because magnetic deformation depends on the interior magnetic field structure and the core equation-of-state, to what extent the magnetic field distorts the NS is yet unclear. Hence, observation of a GW signal would give a hint to the NS physics.

Freely precessing NS

CW observations usually assume a pulsar model whose spin axis aligns with its principal axis, in which case a CW is monochromatic at twice the spin frequency. However, if there exists the misalignment between both axes, the NS is expected to freely precess and emit GWs at once and twice the spin frequencies [32][3]. Cutler and Jones [33] considered the effect of GW back-reaction on NS's precessing motion and showed that a damping time of the wobble angle due to GW radiation is much longer than previously thought [34].

[3] Strictly speaking, frequencies of a CW from a precessing NS are $f_{\rm rot} + f_{\rm prec}$ and $2f_{\rm rot}$, where $f_{\rm rot}$ and $f_{\rm prec}$ denote the spin frequency and the precession frequency, respectively.

However, the subsequent work proved that freely precessing NSs are not appropriate CW sources [35]. When a NS is more realistically modeled as a thin elastic crust containing a superfluid core in place of a rigid body [36], internal dissipation arising from a mutual friction between the crust and the superfluid core tends to damp the wobble angle much more rapidly compared with the GW back-reaction. On the other hand, observational evidence for freely precessing NSs was reported in the studies of PSR B1828–11 [37] and PSR B1642–03 [38][4]. Cutler [39] examined wobbling motion of a NS caused by internal strong toroidal magnetic fields. Because the toroidal B fields act on the NS like a rubber belt and tighten the NS's waist, the NS would be distorted into a prolate shape. Since such a NS would be unstable, the wobble angle is expected to grow up until the angular momentum axis becomes orthogonal to the magnetic axis. Recently, phase modulations in pulsations of the Magnetars 1E 1547.0 — 5408 and 4U 0142+61 in the Suzaku X-ray data were reported by Makishima *et al.* [40, 41]. They interpreted that the phase modulations can be traced to free precessions of the magnetars caused by strong toroidal B fields. Jones [42] proposed the possibility that a NS containing a pinned superfluid core would emit GWs at once and twice the spin frequency even if there is no electromagnetic signature of free precession. Motivated by these observations and the theoretical proposal, Ono, Eda, and Itoh [43, 44] investigated the possibility of estimating the mass of an isolated NS using two-component CWs. They estimated the measurement accuracy of NS mass using Monte Carlo simulations and found that the mass of the NS with its spin frequency 500 Hz and its ellipticity 10^{-6} at 1 kpc is typically measurable with an accuracy of 20% using the Einstein Telescope. Although a two-component model for a CW signal is still controversial as discussed above, a detection of a CW from a known pulsar would elucidate the existence of a freely precessing NS or a NS containing a pinned superfluid core.

Low mass X-ray binaries

Low mass X-ray binary (LMXB) composed of a NS and a low-mass companion being on the main sequence is considered to be one of the most attractive targets for CW search. In this system, gas and dust are stripped from the companion star and accrete on the NS surface. The gravitational potential energy of the accreted matter on the surface of the NS is converted into the energy source of the X-ray emission of the LMXB. The resulting X-ray flux observed at the Earth is roughly estimated to be $F_{\rm X} \sim GM\dot{M}/4\pi Rd^2$, where the accretion rate, the distance to the NS, and the radius of the NS are denoted by $\dot{M}$, d, and R, respectively. Meanwhile, the NS would rotate more rapidly by gaining torque exerted by the matter accretion, $N_{\rm acc} \sim \dot{M}\sqrt{GMR}$. Such a NS's spin-up is expected to last until the spin frequency reaches a break-up frequency of the order of 1.5 kHz

[4] The wobble angles are estimated to be $\theta \simeq 3$ degrees for PSR B1828–11 and $\theta \simeq 0.8$ degrees for PSR B1642–03 [37, 38].

beyond which the NS would be broken by the centrifugal force. However, the maximum spin frequency estimated by EM observations falls much below the break-up frequency contrary to the naive expectation [45]. These observational results indicate the existence of a suppression mechanism that prevents a NS from spin-ups. Bildsten [46] suggested the mechanism stems from gravitational-radiation loss. If this is the case, the angular momentum carried by mass accretion is expected to be in a state of equilibrium with gravitational-radiation loss[5]. Consequently, the GW amplitude h_0 can be related to the observed X-ray flux $F_{\rm X}$ by

$$\begin{aligned} h_0 &= \left(\frac{5}{3}\frac{F_X G R^3}{M f_{\rm rot}}\right)^{1/2} \\ &= 5.5\times10^{-27}\left(\frac{F_{\rm X}}{F_{-8}}\right)^{1/2}\left(\frac{R}{10\ {\rm km}}\right)\left(\frac{1.4\ M_\odot}{M}\right)^{1/4}\left(\frac{300\ {\rm Hz}}{f_{\rm rot}}\right)^{1/2}, \end{aligned} \tag{2.9}$$

where $F_{-8} \equiv 10^{-8}$ erg cm^{-2} s^{-1} [47]. As Eq. (2.9) indicates, Sco X-1 [48] that is the brightest stellar X-ray source in the sky is considered to potentially emit strong CW. So far, GW from Sco-X1 has been investigated by the initial LIGO data [49, 50]. Data analysis methods focusing on Sco X-1 were investigated by several authors including Sideband method [47], TwoSpect method [51], Cross-Correlation method [52], and Stacked $\mathcal{F}$-statistic method based on Einstein@Home [53]. These search methods were compared with each other via a mock-data challenge in [54].

2.2 CW signal model

2.2.1 General form of CW waveform

CW waveform

Generally, CW waveform from a rapidly rotating NS can be characterized by the two independent polarization modes of $h_{\mu\nu}$ as

$$h_+(\tau) = A_+\cos\Phi(\tau), \quad h_\times(\tau) = A_\times\sin\Phi(\tau), \tag{2.10}$$

[5] The torque exerted by the gravitational-radiation loss can be expressed by

$$N_{\rm GW} = \frac{32G(\varepsilon I_{zz})^2\omega_{\rm rot}^5}{5c^5}. \tag{2.7}$$

The GW amplitude h_0 is related to the GW torque $N_{\rm gw}$ by

$$h_0^2 = \frac{5G}{8c^3d^2\omega_{\rm rot}^2}N_{\rm gw}. \tag{2.8}$$

where $\Phi(\tau)$ is the GW phase observed at the Solar-system barycenter (SSB). The amplitudes $A_{+,\times}$ correspond to the two polarization modes and are defined as

$$A_+ = \frac{1}{2}h_0\left(1+\cos^2\iota\right), \quad A_\times = h_0\cos\iota, \tag{2.11a}$$

$$h_0 = \frac{4\pi^2 G}{c^4 d}\varepsilon I_{zz} f_{\mathrm{gw}}^2, \tag{2.11b}$$

where h_0 and ι denote the overall amplitude and the inclination angle that is defined as the angle between the line-of-sight and the spin axis of the NS, respectively [55]. The parameters c, d, G and f_{gw} represent the speed of light, the distance to the source, the gravitational constant, and the GW frequency, respectively. Equation (2.11b) indicates that a more rapidly rotating NS with larger ε produces a stronger CW signal.

CW signal

CW signals are written as a linear sum of h_+ and $h_\times$,

$$\begin{aligned} s(t;\mathcal{A},\boldsymbol{\lambda}) &= \sum_{A=+,\times} F_A h_A \\ &= F_+(t;\hat{\boldsymbol{n}},\psi)\,A_+\cos\Phi(t;\boldsymbol{\lambda}) + F_\times(t;\hat{\boldsymbol{n}},\psi)\,A_\times\sin\Phi(t;\boldsymbol{\lambda}), \end{aligned} \tag{2.12}$$

where the coefficients $F_{+,\times}$ are called the antenna pattern functions that depends on both the position and direction of the detector with respect to the source. The parameters $\mathcal{A}$ and $\boldsymbol{\lambda}$ are the collections of the amplitude parameters $\mathcal{A} = \{A_+, A_\times, \psi, \phi_0\}$ and the Doppler parameters $\boldsymbol{\lambda} = \{\hat{\boldsymbol{n}}, f, \dot{f}, \cdots\}$, respectively. The sky position of the source is specified by the unit vector $\hat{\boldsymbol{n}} \equiv (\cos\delta\cos\alpha, \cos\delta\sin\alpha, \sin\delta)$, where α and δ are called the right ascension and the declination, respectively. The antenna pattern functions $F_{+,\times}$ represent the response of the detector to incident GWs and are expressed by

$$F_+(t;\hat{\boldsymbol{n}},\psi) = \sin\zeta\left[a(t;\hat{\boldsymbol{n}})\cos 2\psi + b(t;\hat{\boldsymbol{n}})\sin 2\psi\right], \tag{2.13a}$$

$$F_\times(t;\hat{\boldsymbol{n}},\psi) = \sin\zeta\left[b(t;\hat{\boldsymbol{n}})\cos 2\psi - a(t;\hat{\boldsymbol{n}})\sin 2\psi\right], \tag{2.13b}$$

where ζ is the angle between two arms of the detector, ψ is the polarization angle, and two time-dependent functions $a(t)$ and $b(t)$ are often referred to as the modulation amplitudes. The concrete expressions for the modulation amplitudes are given in Appendix C. The definitions of $\hat{\boldsymbol{n}}$ and ψ are illustrated in Fig. 2.2. As shown in Eqs. (2.12), (2.13a), and (2.13b), the CW signal strength is proportional to $\sin\zeta$. This factor implies that compared with a 90°-interferometer, a signal-to-noise ratio (SNR) is reduced by a factor of $\sqrt{3}/2$ in the case of a 60°-interferometer such as the Laser Interferometer Space Antenna (LISA) and the Einstein Telescope because the SNR scales as the CW amplitude as will be

discussed later. In what follows, ζ is assumed to be $\pi/2$.

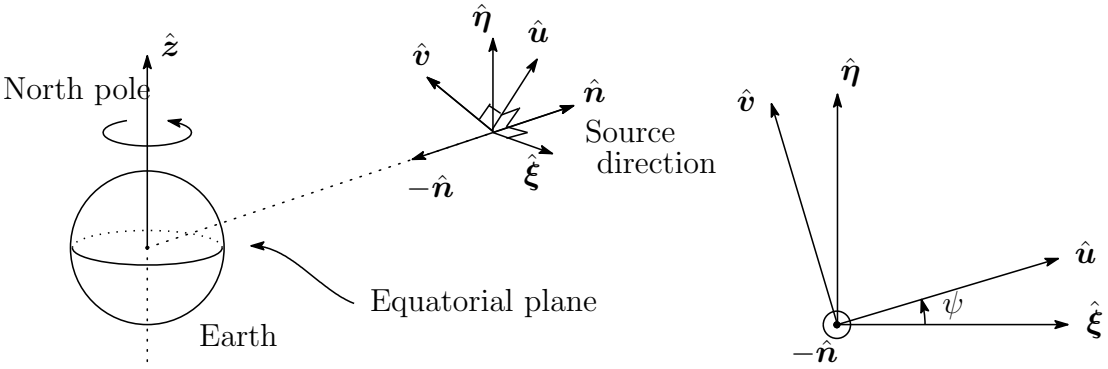

Figure 2.2: Definition of $\hat{\boldsymbol{n}}$ and ψ. The unit vector $\hat{\boldsymbol{n}}$ is defined as the unit vector pointing toward the source from the detector. It is convenient to introduce an orthogonal bases $\{-\hat{\boldsymbol{n}}, \hat{\boldsymbol{\xi}}, \hat{\boldsymbol{\eta}}\}$ and $\{-\hat{\boldsymbol{n}}, \hat{\boldsymbol{u}}, \hat{\boldsymbol{v}}\}$. The polarization phase ψ is defined as the angle from $\hat{\boldsymbol{\xi}}$ to $\hat{\boldsymbol{u}}$. Concrete expressions for these orthonomal bases are shown in the footnote[7].

GW phase

Instantaneous signal frequency received at the SSB is defined as $2\pi f(\tau) \equiv d\Phi(\tau)/d\tau$. Assuming that the SSB and the source are at rest with respect to each other, the signal frequency varies slowly due to NS's spin-down or spin-up. Thus, the phase can be expanded in a Taylor series about the reference time $\tau_{\rm ref}$ as

$$\Phi(\tau) \equiv \phi_0 + \phi(\tau), \tag{2.16a}$$

$$\phi(\tau) = 2\pi \sum_{k=0}^{s} \frac{f^{(k)}(\tau_{\rm ref})}{(k+1)!} \Delta\tau^{k+1}, \tag{2.16b}$$

where $\phi_0 \equiv \Phi(\tau_{\rm ref})$ and $\Delta\tau \equiv \tau - \tau_{\rm ref}$. The parameter τ is the time that the wavefront arrives at the SSB. The time t at which the same wavefront is observed at the detector is

[7] In the equatorial coordinate system, an orthogonal basis $\{-\hat{\boldsymbol{n}}, \hat{\boldsymbol{\xi}}, \hat{\boldsymbol{\eta}}\}$ is expressed as

$$\hat{\boldsymbol{n}} \equiv (\cos\delta\cos\alpha, \cos\delta\sin\alpha, \sin\delta), \tag{2.14a}$$

$$\hat{\boldsymbol{\xi}} \equiv \frac{\hat{\boldsymbol{n}} \times \hat{\boldsymbol{z}}}{|\hat{\boldsymbol{n}} \times \hat{\boldsymbol{z}}|} = (\sin\alpha, -\cos\alpha, 0), \tag{2.14b}$$

$$\hat{\boldsymbol{\eta}} \equiv \hat{\boldsymbol{\xi}} \times \hat{\boldsymbol{n}} = (-\sin\delta\cos\alpha, -\sin\delta\sin\alpha, \cos\delta), \tag{2.14c}$$

where the unit vector $\hat{\boldsymbol{z}} = (0, 0, 1)$ is assumed to align with the North pole of the Earth. The unit vectors $\hat{\boldsymbol{u}}$ and $\hat{\boldsymbol{v}}$ are

$$\hat{\boldsymbol{u}} = \hat{\boldsymbol{\xi}}\cos\psi + \hat{\boldsymbol{\eta}}\sin\psi, \quad \hat{\boldsymbol{v}} = -\hat{\boldsymbol{\xi}}\sin\psi + \hat{\boldsymbol{\eta}}\cos\psi, \tag{2.15}$$

where the polarizaton phase is defined as $\sin\psi \equiv \hat{\boldsymbol{u}} \cdot \hat{\boldsymbol{\eta}}$ and $\cos\psi \equiv \hat{\boldsymbol{u}} \cdot \hat{\boldsymbol{\xi}}$.

related to the SSB time τ by

$$\tau = t + \frac{\boldsymbol{r}(t) \cdot \hat{\boldsymbol{n}}}{c} - \frac{d}{c} + \Delta_{\mathrm{rel}\odot}, \tag{2.17}$$

where $\boldsymbol{r} \cdot \boldsymbol{n}/c$ is the Römer time delay[8], d/c is the propagation time from the source to the SSB, and $\Delta_{\mathrm{rel}\odot}$ is the relativistic time delay caused by the Shapiro time delay[9] and the Einstein time delay[10]. Since d/c is treated as a constant in the case of isolated NSs, this term are neglected in the following for simplicity. In practice, the phase part can be modeled as

$$\phi(\tau) = 2\pi\Delta\tau \left[f(\tau_{\mathrm{ref}}) + \frac{1}{2}\dot{f}(\tau_{\mathrm{ref}})\,\Delta\tau \right]. \tag{2.21}$$

Taking the time derivative of $\phi(\tau)$, the instantaneous signal frequency received at the SSB is expressed up to the second order of the spin-down effects as

$$f(t) = \hat{f}(t)\left(1 + \frac{\boldsymbol{v}(t) \cdot \hat{\boldsymbol{n}}}{c}\right), \tag{2.22a}$$

$$\hat{f}(t) \simeq f(\tau_{\mathrm{ref}}) + \dot{f}(\tau_{\mathrm{ref}})\,(t - \tau_{\mathrm{ref}}), \tag{2.22b}$$

where $\hat{f}(t)$ denotes the intrinsic frequency that varies with time only due to the NS's spin-up and spin-down effects. When performing a CW search, the relativistic corrections and the higher order derivatives of the spin-frequency are taken into account in this thesis[11].

[8] The detector motion is decomposed into the orbital motion around the Sun and the rotational motion around its spin axis as $\boldsymbol{r}(t) = \boldsymbol{r}_{\mathrm{orb}}(t) + \boldsymbol{r}_{\mathrm{spin}}(t)$. So, the Römer time delay is estimated by

$$\left|\frac{\boldsymbol{r}(t) \cdot \boldsymbol{n}}{c}\right| \leq \frac{|\boldsymbol{r}_{\mathrm{orb}}(t) \cdot \boldsymbol{n}|}{c} + \frac{|\boldsymbol{r}_{\mathrm{spin}}(t) \cdot \boldsymbol{n}|}{c} \leq \frac{R_{\mathrm{ES}}}{c} + \frac{R_{\mathrm{E}}}{c} \simeq 5.0 \times 10^2 \text{ sec}, \tag{2.18}$$

where R_{ES} and R_{E} denote the distance from the Earth and the Sun and the Earth radius, respectively.

[9] The Shapiro time delay originates from the curvature created by the gravitational potential of the Solar system. A GW takes a slightly longer time to reach a detector than it would in the flat space. The maximum value of the Shapiro time delay is roughly estimated to be

$$\Delta_{S\odot} \leq \frac{2GM_\odot}{c^3} \ln \frac{1 + \cos\theta_2}{1 + \cos\theta_1} \simeq 1.2 \times 10^{-4} \text{ sec}, \tag{2.19}$$

where $\theta_1 = \pi - \xi, \theta_2 = \xi$, and $\xi = \arctan(R_\odot/R_{\mathrm{ES}})$.

[10] The Einstein time delay is the effect of the gravitational redshift caused by the Solar system and is approximately evaluated by

$$\frac{d\Delta_{E\odot}}{dt} = \frac{1}{c^2}\left[\frac{GM_\odot}{r} + \frac{1}{2}v_\oplus^2\right]. \tag{2.20}$$

[11] If some effect contributes to the accumulation of the GW phase over the total observation time less than 1/4 of a cycle, neglecting this effect leads to a reduction of SNR by not more than 10%. This is known as 1/4 of a cycle criterion (see Appendix A in [56] for more details).

2.2.2 JKS factorization

Combining Eqs. (2.12), (2.13a), (2.13b), and (2.16a), CW signal measured at a detector is factorized as

$$s\left(t;\mathcal{A},\boldsymbol{\lambda}\right)=\sum_{\mu=1}^{4}\mathcal{A}^{\mu}h_{\mu}\left(t;\boldsymbol{\lambda}\right), \tag{2.23}$$

where $\mathcal{A}^{\mu}$s are often referred to as amplitude parameters [57]. They represent the strength of the CW signal and are defined as

$$\mathcal{A}^{1}\equiv A_{+}\cos\phi_{0}\cos 2\psi-A_{\times}\sin\phi_{0}\sin 2\psi, \tag{2.24a}$$
$$\mathcal{A}^{2}\equiv A_{+}\cos\phi_{0}\sin 2\psi+A_{\times}\sin\phi_{0}\cos 2\psi, \tag{2.24b}$$
$$\mathcal{A}^{3}\equiv -A_{+}\sin\phi_{0}\cos 2\psi-A_{\times}\cos\phi_{0}\sin 2\psi, \tag{2.24c}$$
$$\mathcal{A}^{4}\equiv -A_{+}\sin\phi_{0}\sin 2\psi+A_{\times}\cos\phi_{0}\cos 2\psi. \tag{2.24d}$$

The four time-dependent parts h_{μ}s in Eq. (2.23) characterize the shape of the CW signal and depend on the modulation amplitudes $a\left(t\right)$ and $b\left(t\right)$. These four basis waveforms h_{μ}s are expressed as

$$h_{1}\left(t;\boldsymbol{\lambda}\right)\equiv a\left(t;\hat{\boldsymbol{n}}\right)\cos\phi\left(t;\boldsymbol{\lambda}\right),\quad h_{2}\left(t;\boldsymbol{\lambda}\right)\equiv b\left(t;\hat{\boldsymbol{n}}\right)\cos\phi\left(t;\boldsymbol{\lambda}\right), \tag{2.25a}$$
$$h_{3}\left(t;\boldsymbol{\lambda}\right)\equiv a\left(t;\hat{\boldsymbol{n}}\right)\sin\phi\left(t;\boldsymbol{\lambda}\right),\quad h_{4}\left(t;\boldsymbol{\lambda}\right)\equiv b\left(t;\hat{\boldsymbol{n}}\right)\sin\phi\left(t;\boldsymbol{\lambda}\right). \tag{2.25b}$$

It should be noted that dependencies on the amplitude parameters and the Doppler parameters are completely separated from each other in Eq. (2.23).

2.3 $\mathcal{F}$-statistic

2.3.1 CW signal buried in detector noise

Let us consider GW observation by a network of N_{det} detectors. The collection of multi-detector output data is denoted by $\boldsymbol{x}\left(t\right)=\left(x^{1}\left(t\right),\cdots,x^{N}\left(t\right)\right)$, where $x^{X}\left(t\right)$ stands for the output of the X-th detector. The output data can be written as the linear sum of detector noise and a CW signal with parameters $\mathcal{A}$ and $\boldsymbol{\lambda}$ by

$$\boldsymbol{x}\left(t\right)=\boldsymbol{n}\left(t\right)+\boldsymbol{s}\left(t;\mathcal{A},\boldsymbol{\lambda}\right), \tag{2.26a}$$
$$\boldsymbol{s}\left(t;\mathcal{A},\boldsymbol{\lambda}\right)=\mathcal{A}^{\mu}\boldsymbol{h}_{\mu}\left(t;\boldsymbol{\lambda}\right), \tag{2.26b}$$

where the Einstein summation rule is adopted in Eq. (2.26b). Assuming stationarities of detector noises in a detector network, an autocorrelation function κ^{XY} between n^X and n^Y is related to the one-sided power spectral density $S^{XY}(f)$ by virtue of the Wiener-Khinchin theorem,

$$\kappa^{XY}(\tau) = \langle n^X(t+\tau)\, n^Y(t)\rangle, \tag{2.27a}$$

$$S^{XY}(f) = 2\int_{-\infty}^{\infty} \kappa^{XY}(\tau)\, e^{-2\pi i f\tau}. \tag{2.27b}$$

In Fourier space, these equations can be reduced to an ensemble average between the different Fourier components of noises as

$$\langle \tilde{n}^X(f)\, \tilde{n}^{Y*}(f')\rangle = \frac{1}{2}\delta(f-f')\, S^{XY}(f). \tag{2.28}$$

It is convenient to introduce noise-weighted inner product between two time-dependent functions $\boldsymbol{x}(t)$ and $\boldsymbol{y}(t)$ as

$$(\boldsymbol{x}|\boldsymbol{y}) = 4\mathrm{Re}\int_0^{\infty} \tilde{x}^X(f)\, S^{-1}_{XY}(f)\, \tilde{y}^{Y*}(f)\, df, \tag{2.29}$$

where S^{-1}_{XY} represents the inverse matrix and satisfies $S^{-1}_{XY}S^{YZ} = \delta_{XZ}$.

2.3.2 $\mathcal{F}$-statistic

Definition of the $\mathcal{F}$-statistic

When the detector noise is stationary and Gaussian, its probability distribution function (PDF) obeys $p(\boldsymbol{n}) \propto \exp[-(\boldsymbol{n}|\boldsymbol{n})/2]$ as is verified in Appendix A. From a standpoint of the Frequentist, the most optimal detection statistic to discriminate whether or not a CW signal exists in observation data $\boldsymbol{x}$ is achieved by a likelihood ratio $\Lambda(\boldsymbol{x};\boldsymbol{s})$ according to the Neyman-Pearson lemma[12], which is defined as

$$\ln\Lambda(\boldsymbol{x};\boldsymbol{s}) \equiv \ln\frac{P(\boldsymbol{x}|\boldsymbol{s})}{P(\boldsymbol{x}|\boldsymbol{0})} = (\boldsymbol{x}|\boldsymbol{s}) - \frac{1}{2}(\boldsymbol{s}|\boldsymbol{s}). \tag{2.30}$$

Substituting Eq. (2.26b) into Eq. (2.30) gives rise to

$$\ln\Lambda(\boldsymbol{x};\mathcal{A},\boldsymbol{\lambda}) = \mathcal{A}^\mu x_\mu - \frac{1}{2}\mathcal{A}^\mu\mathcal{M}_{\mu\nu}\mathcal{A}^\nu, \tag{2.31a}$$

$$x_\mu(\boldsymbol{\lambda}) \equiv (\boldsymbol{x}|\boldsymbol{h}_\mu), \quad \mathcal{M}_{\mu\nu}(\boldsymbol{\lambda}) \equiv (\boldsymbol{h}_\mu|\boldsymbol{h}_\nu). \tag{2.31b}$$

[12] Optimal strategy for sinusoidal signals buried in noisy data is discussed by the use of the Neyman-Pearson criteria in [58].

The $\mathcal{F}$-statistic[13] is defined as the maximization of $\ln\Lambda\left(\boldsymbol{x};\mathcal{A},\lambda\right)$ over the amplitude parameters $\mathcal{A}^{\mu}$,

$$2\mathcal{F}\left(\boldsymbol{x};\boldsymbol{\lambda}\right)\equiv\max_{\mathcal{A}^{\mu}}\left[2\ln\Lambda\left(\boldsymbol{x};\mathcal{A},\boldsymbol{\lambda}\right)\right]=x_{\mu}\mathcal{M}^{\mu\nu}x_{\nu}, \tag{2.32}$$

[14] where $\mathcal{M}^{\mu\nu}$ denotes the inverse matrix of $\mathcal{M}_{\mu\nu}$, namely $\mathcal{M}^{\mu\nu}\equiv\{\mathcal{M}^{-1}\}^{\mu\nu}$. In this process, the amplitude parameters are projected out and only the Doppler parameters $\boldsymbol{\lambda}$ are to be searched over.

Concrete expression for the $\mathcal{F}$-statistic

In an actual data set, detector noises in a detector network are not stationary and different from each other. To handle the non-stationarities, time series data are broken up into shorter time segments called SFT segments. The time baseline of SFTs, T_{SFT}, is chosen such that the noise level in the α-th SFT and the X-th detector, $S^{X,\alpha}\left(f\right)$, can be regarded as stationary. It is convenient to introduce the following notations.

$$\langle f\rangle_{t}\equiv\frac{1}{T_{\mathrm{SFT}}}\int_{-T_{\mathrm{SFT}}/2}^{T_{\mathrm{SFT}}/2}f\left(t\right)dt, \tag{2.34a}$$

$$\langle Q\rangle_{w}\equiv\frac{1}{N_{\mathrm{SFT}}}\sum_{X,\alpha}w_{X,\alpha}\langle Q^{X,\alpha}\rangle_{t}, \tag{2.34b}$$

$$w_{X,\alpha}\equiv\frac{S_{X,\alpha}^{-1}}{\mathcal{S}^{-1}}, \tag{2.34c}$$

where $\mathcal{S}^{-1}\equiv\sum_{X,\alpha}S_{X,\alpha}^{-1}$. By definition, $\sum_{X,\alpha}w_{X,\alpha}=N_{\mathrm{SFT}}$ is satisfied. The symbols $\langle\cdots\rangle_{t},\langle\cdots\rangle_{w}$, and $w_{X,\alpha}$ denote the time average over a single SFT, the total noise-weighted average, and the noise weights. Assuming each detector noise is independent of each other, $S_{XY}^{-1}=S_{X}^{-1}\delta_{XY}$ is satisfies. The noise weighted inner product shown in Eq. (2.29) can be

[13] The $\mathcal{F}$-statistic was first introduced by Jaranowski, Królak, and Schutz in [57] (well known as JKS98). The $\mathcal{F}$-statistic is generalized to the case of multi-detector network and multiple pulsars by Cutler and Schutz in [59]. Jaranowski and Królak proposed the $\mathcal{G}$-statistic in [60]. They considered the case where there are two unknown parameters, over-all amplitude and initial phase, whereas polarization phase and inclination are already measured by X-ray observations as in the case of the Vela pulsar. The $\mathcal{G}$-statistic is derived from the maximum-likelihood method in a similar way to the $\mathcal{F}$-statistic.

[14] Completing the square of the log-likelihood ratio is

$$2\ln\Lambda\left(\boldsymbol{x};\mathcal{A},\boldsymbol{\lambda}\right)=-\left(\mathcal{A}^{\mu}-x_{\rho}\mathcal{M}^{\rho\mu}\right)\mathcal{M}_{\mu\nu}\left(\mathcal{A}^{\nu}-\mathcal{M}^{\nu\sigma}x_{\sigma}\right)+x_{\mu}\mathcal{M}^{\mu\nu}x_{\nu}. \tag{2.33}$$

So, $\ln\Lambda$ takes the maximum value at $\hat{\mathcal{A}}^{\mu}=\mathcal{M}^{\mu\nu}x_{\nu}$ that are called the maximum likelihood estimators.

approximated as[15]

$$(\boldsymbol{x}|\boldsymbol{y}) \simeq \frac{2T_{\mathrm{obs}}}{\mathcal{S}}\langle xy\rangle_w \tag{2.36}$$

where a narrow-band approximation around $f = f_0 \equiv f(\tau_{\mathrm{ref}})$ is used because a spin frequency is regarded as a nearly constant during an observation. Using Eq. (2.36), $\mathcal{M}_{\mu\nu}$ in Eq. (2.31b) is expressed as[16]

$$\mathcal{M}_{\mu\nu} \simeq \frac{1}{2}\begin{pmatrix} A & C & 0 & 0 \\ C & B & 0 & 0 \\ 0 & 0 & A & C \\ 0 & 0 & C & B \end{pmatrix}, \quad \mathcal{M}^{\mu\nu} \simeq \frac{2}{D}\begin{pmatrix} B & -C & 0 & 0 \\ -C & A & 0 & 0 \\ 0 & 0 & B & -C \\ 0 & 0 & -C & A \end{pmatrix}, \tag{2.38}$$

where A, B, C, D are defined as

$$A \equiv (\boldsymbol{a}|\boldsymbol{a}), \quad B \equiv (\boldsymbol{b}|\boldsymbol{b}), \quad C \equiv (\boldsymbol{a}|\boldsymbol{b}), \quad D \equiv AB - C^2. \tag{2.39}$$

Combining Eqs. (2.32), (2.38), and (2.39) brings the $\mathcal{F}$-statistic to the following form:

$$\mathcal{F} = \frac{B}{D}\left(x_1^2 + x_3^2\right) + \frac{A}{D}\left(x_2^2 + x_4^2\right) - \frac{2C}{D}\left(x_1x_2 + x_3x_4\right). \tag{2.40}$$

[15] Using the narrow-band approximation and the independence of the detector noise, $(\boldsymbol{x}|\boldsymbol{y})$ is approximated as

$$\begin{aligned}(\boldsymbol{x}|\boldsymbol{y}) &\simeq \sum_X 4S_X^{-1}(f_0)\,\mathrm{Re}\int_0^\infty \tilde{x}^X(f)\,\tilde{y}^{X*}(f)\,df \simeq \sum_X 2S_X^{-1}(f_0)\int_{-T_{\mathrm{obs}}/2}^{T_{\mathrm{obs}}/2} x^X(t)\,y^X(t)\,dt \\ &\simeq \sum_{X,\alpha} 2S_{X,\alpha}^{-1}(f_0)\int_{-T_{\mathrm{SFT}}/2}^{T_{\mathrm{SFT}}/2} x^{X,\alpha}(t)\,y^{X,\alpha}(t)\,dt = \sum_{X,\alpha} 2T_{\mathrm{SFT}}S_{X,\alpha}^{-1}\langle x^{X,\alpha}y^{X,\alpha}\rangle_t \\ &= 2N_{\mathrm{SFT}}T_{\mathrm{SFT}}\mathcal{S}^{-1}\sum_{X,\alpha}\frac{1}{N_{\mathrm{SFT}}}w_{X,\alpha}\langle x^{X,\alpha}y^{X,\alpha}\rangle = \frac{2T_{\mathrm{obs}}}{\mathcal{S}}\langle xy\rangle_w,\end{aligned} \tag{2.35}$$

where $T_{\mathrm{obs}} = N_{\mathrm{SFT}}T_{\mathrm{SFT}}$ was used. In the first line, the Parseval's theorem was employed to convert the integration in the frequency domain to the time domain. In the second line, $x^{X,\alpha}(t) = x^X(t_{X,\alpha} + t)$ is used, where $t_{X,\alpha}$ denotes the centering time of the α-th SFT in the X-th detector.

[16] Temporal changes in modulation amplitudes are caused by the Earth's motion. So, $a(t)$ and $b(t)$ varies much more slowly with time than the phase $\phi(t)$ varying on the time scale of $1/f_0$. This fact leads to the following approximations.

$$(\boldsymbol{h}_1|\boldsymbol{h}_3) \simeq (\boldsymbol{h}_1|\boldsymbol{h}_4) \simeq (\boldsymbol{h}_2|\boldsymbol{h}_3) \simeq (\boldsymbol{h}_2|\boldsymbol{h}_4) \simeq 0, \tag{2.37a}$$

$$(\boldsymbol{h}_1|\boldsymbol{h}_1) \simeq (\boldsymbol{h}_3|\boldsymbol{h}_3) \simeq \frac{1}{2}(\boldsymbol{a}|\boldsymbol{a}) \equiv \frac{1}{2}A, \tag{2.37b}$$

$$(\boldsymbol{h}_2|\boldsymbol{h}_2) \simeq (\boldsymbol{h}_4|\boldsymbol{h}_4) \simeq \frac{1}{2}(\boldsymbol{b}|\boldsymbol{b}) \equiv \frac{1}{2}B, \tag{2.37c}$$

$$(\boldsymbol{h}_1|\boldsymbol{h}_2) \simeq (\boldsymbol{h}_3|\boldsymbol{h}_4) \simeq \frac{1}{2}(\boldsymbol{a}|\boldsymbol{b}) \equiv \frac{1}{2}C, \tag{2.37d}$$

where the observation time T_{obs} is assumed to be much longer than $1/f_0$.

PDF of $\mathcal{F}$-statistic

Completing the square of the $\mathcal{F}$-statistic in Eq. (2.40) leads to the form of the sum of the squares of four Gaussian random variables. In fact, there exists a linear transformation $\mathcal{L}$ such that[17]

$$x_i \equiv \mathcal{L}_{ij} z_j, \tag{2.42a}$$

$$2\mathcal{F} = z_1^2 + z_2^2 + z_3^2 + z_4^2. \tag{2.42b}$$

Since z_i can be obtained by the linear transformation of x_i obeying the Gaussian distribution, new variables z_i also obey the Gaussian distribution. Therefore, $2\mathcal{F}$ is distributed according to a non-central chi-squared distribution with four degrees of freedom (see Appendix B for more details).

2.4 Targeted search

A targeted search aims to search for a CW signal from an already discovered pulsar . The pulsar parameters such as the sky position, the spin frequency, and the spin-down rates are measured by EM observations. In other words, the Doppler parameters $\boldsymbol{\lambda}$ are known whereas the amplitude parameters $\mathcal{A}$ are unknown. As shown in Eq. (2.40), an $\mathcal{F}$-statistic value is a function only of the Doppler parameters $\boldsymbol{\lambda}$ because the amplitude parameters $\mathcal{A}$ are projected out in the process of the maximization of the log-likelihood ratio. Thus, in a targeted search, there is no need to explore a wide-parameter-space.

2.4.1 Theoretically expected upper limits

Average SNR^2

The output data $\boldsymbol{x}$ projected on the basis waveforms h_μ is expressed by

$$x_\mu(\mathcal{A}, \boldsymbol{\lambda}) = n_\mu + s_\mu(\mathcal{A}, \boldsymbol{\lambda}), \tag{2.43a}$$

$$x_\mu \equiv (\boldsymbol{x}|\boldsymbol{h}_\mu), \quad n_\mu \equiv (\boldsymbol{n}|\boldsymbol{h}_\mu), \quad s_\mu \equiv (\boldsymbol{s}|\boldsymbol{h}_\mu). \tag{2.43b}$$

Assuming that detector noise obeys Gaussian distribution, the ensemble average of n_μ

[17] The concrete expression for $\mathcal{L}$ is

$$\mathcal{L} \equiv \frac{1}{2}\begin{pmatrix} \mathcal{N} & \mathcal{O} \\ \mathcal{O} & \mathcal{N} \end{pmatrix}, \qquad \mathcal{N} \equiv \begin{pmatrix} \sqrt{A + \sqrt{\frac{A}{B}}C} & -\sqrt{A - \sqrt{\frac{A}{B}}C} \\ \sqrt{B + \sqrt{\frac{B}{A}}C} & \sqrt{B - \sqrt{\frac{B}{A}}C} \end{pmatrix}, \tag{2.41}$$

where A, B, and C are defined by Eq. (2.39).

and $n_\mu n_\nu$ are expressed as $\langle n_\mu \rangle = 0$ and $\langle n_\mu n_\nu \rangle = \mathcal{M}_{\mu\nu}$, where $\langle (\boldsymbol{n}|\boldsymbol{h}_\mu)(\boldsymbol{n}|\boldsymbol{h}_\nu)\rangle = (\boldsymbol{h}_\mu|\boldsymbol{h}_\nu)$ is used. Using these relations, the ensemble averages of x_μ and $x_\mu x_\nu$ are computed as $\langle x_\mu \rangle = s_\mu$ and $\langle x_\mu x_\nu \rangle = s_\mu s_\nu + \mathcal{M}_{\mu\nu}$. Thus, the expection value of the $\mathcal{F}$-statistic for perfectly matched signals can be expressed by

$$\langle 2\mathcal{F} \rangle = 4 + \rho^2(\boldsymbol{0}), \tag{2.44a}$$

$$\rho^2(\boldsymbol{0}) \equiv (\boldsymbol{s}|\boldsymbol{s}), \tag{2.44b}$$

where $\rho(\boldsymbol{0})$ denotes the optimal SNR[18]. The argument of $\rho(\boldsymbol{0})$ stands for the fact that there is no signal-template mismatch, namely $\Delta\boldsymbol{\lambda} = \boldsymbol{0}$. Combining Eqs. (2.24a)–(2.24d), and (2.38), the optimal SNR in Eq. (2.44b) is computed as

$$\begin{aligned}
\rho^2(\boldsymbol{0}) &= \mathcal{A}^\mu \mathcal{M}_{\mu\nu} \mathcal{A}^\nu \\
&= \frac{1}{2}\left[\left(\mathcal{A}_1^2 + \mathcal{A}_3^2\right) A + \left(\mathcal{A}_2^2 + \mathcal{A}_4^2\right) B + 2\left(\mathcal{A}_1\mathcal{A}_2 + \mathcal{A}_3\mathcal{A}_4\right) C\right] \\
&= \frac{1}{2} h_0^2 \left(\alpha_1 A + \alpha_2 B + 2\alpha_3 C\right) \\
&= h_0^2 \frac{T_{\mathrm{obs}}}{\mathcal{S}} \left[\alpha_1 \langle a^2 \rangle_T + \alpha_2 \langle b^2 \rangle_T + 2\alpha_3 \langle ab \rangle_T\right],
\end{aligned} \tag{2.46}$$

where the coefficients α_1, α_2, and α_3 are defined by

$$\alpha_1 \equiv \frac{1}{4}\left(1 + \cos^2\iota\right)^2 \cos^2 2\psi + \cos^2\iota \sin^2 2\psi, \tag{2.47a}$$

$$\alpha_2 \equiv \frac{1}{4}\left(1 + \cos^2\iota\right)^2 \sin^2 2\psi + \cos^2\iota \cos^2 2\psi, \tag{2.47b}$$

$$\alpha_3 \equiv \frac{1}{4}\left(1 - \cos^2\iota\right)^2 \sin 2\psi \cos 2\psi. \tag{2.47c}$$

As is shown in Eq. (2.46), the SNR depends on $h_0, \cos\iota, \psi, \alpha, \delta, f_0, \dot{f}, \cdots$, but is independent of the initial phase ϕ_0. In order to evaluate average SNR^2, it is convenient to introduce

$$\langle Q \rangle_{\alpha,\delta,\cos\iota,\psi} = \int_0^{2\pi} \frac{d\alpha}{2\pi} \int_{-1}^{1} \frac{d(\cos\delta)}{2} \int_{-1}^{1} \frac{d(\cos\iota)}{2} \int_0^{2\pi} \frac{d\psi}{2\pi}\, Q(\alpha, \delta, \cos\iota, \psi), \tag{2.48}$$

where $\langle Q \rangle_{\alpha,\delta,\cos\iota,\psi}$ denotes the quantity Q averaged over the angular parameters $\{\alpha, \delta, \cos\iota, \psi\}$. To put it another way, $\langle Q \rangle_{\alpha,\delta,\cos\iota,\psi}$ is the average of Q assuming isotropically distributed

[18] The ensemble average of $2\mathcal{F}$ is computed in the following way:

$$\begin{aligned}
\langle 2\mathcal{F} \rangle &= \langle x_\mu \mathcal{M}^{\mu\nu} x_\nu \rangle = \mathcal{M}^{\mu\nu} \langle x_\mu x_\nu \rangle = \mathcal{M}^{\mu\nu}\left(s_\mu s_\nu + \mathcal{M}_{\mu\nu}\right) = \delta_\mu{}^\mu + s_\mu \mathcal{M}^{\mu\nu} s_\nu \\
&= 4 + \mathcal{A}^\alpha \mathcal{M}_{\mu\alpha} \mathcal{M}^{\mu\nu} M_{\nu\beta} \mathcal{A}^\beta = 4 + \mathcal{A}^\alpha \mathcal{M}_{\alpha\beta} \mathcal{A}^\beta = 4 + (\boldsymbol{s}|\boldsymbol{s}) = 4 + \rho^2(\boldsymbol{0}),
\end{aligned} \tag{2.45}$$

where $\boldsymbol{s} = \mathcal{A}^\alpha \boldsymbol{h}_\alpha$ and $\mathcal{M}_{\mu\nu}\mathcal{M}^{\nu\lambda} = \delta_\mu{}^\lambda$ were used.

pulsars over the sky with isotropically distributed orientations. Using Eqs. (2.46) and (2.48), the root-mean-square (RMS) SNR is derived as[19]

$$\sqrt{\langle \rho^2 (\mathbf{0}) \rangle_{\alpha,\delta,\cos\iota,\psi}} = \frac{2}{5} h_0 \sqrt{\frac{T_{\rm obs}}{\mathcal{S}}}. \tag{2.49}$$

The RMS SNR is characterized by $h_0\sqrt{T_{\rm obs}/\mathcal{S}}$, which is called the statistical factor. It should be noted that $\sqrt{\langle \rho^2 (\mathbf{0}) \rangle_{\alpha,\delta,\cos\iota,\psi}}$ scales as $T_{\rm obs}^{1/2}$ in the case of coherent search, whereas a SNR in incoherent search scales as $T_{\rm obs}^{1/4} N_{\rm seg}^{-1/4}$. If the sensitivities of the detectors take the same value S_n at the frequency f_0, $\mathcal{S} = S_n/N_{\rm det}$ holds. Therefore, since the RMS SNR is proportional to $\mathcal{S}^{-1/2}$, the sensitivity of a multi-detector network is better than a single detector by a factor of $N_{\rm det}^{1/2}$.

Expected upper limits

As is discussed in the previous section, $2\mathcal{F}$ in the absence of a CW signal follows a chi-squared distribution with four degrees of freedom. The PDF of $2\mathcal{F}$ with $\rho^2 = 0$ is $p\left(2\mathcal{F}|\rho^2 = 0\right) = \mathcal{F}e^{-\mathcal{F}}/2$. In the presence of a CW signal, $2\mathcal{F}$ obeys a non-central chi-squared distribution displayed by Eqs. (3.30), (3.31a), and (3.31c). Setting $\mathcal{F}^*$ to be a threshold for detection, the false-alarm rate $p_{\rm FA}\left(2\mathcal{F}^*\right)$ and the false-dismissal rate $p_{\rm FD}\left(2\mathcal{F}^*, \rho^2\right)$ can be expressed as

$$p_{\rm FA}\left(2\mathcal{F}^*\right) = \int_{2\mathcal{F}^*}^{\infty} p\left(2\mathcal{F}|\rho^2 = 0\right) d\left(2\mathcal{F}\right) = \left(1 + \mathcal{F}^*\right) e^{-\mathcal{F}^*}, \tag{2.50a}$$

$$p_{\rm FD}\left(2\mathcal{F}^*, \rho^2\right) = \int_{0}^{2\mathcal{F}^*} p\left(2\mathcal{F}|\rho^2\right) d\left(2\mathcal{F}\right), \tag{2.50b}$$

where $p_{\rm FA}\left(2\mathcal{F}^*\right)$ can be calculated analytically, whereas $p_{\rm FD}\left(2\mathcal{F}^*, \rho^2\right)$ requires the numerical integration (see Fig. 2.3). If a false-alarm rate is taken to be 1%, a detection threshold is $2\mathcal{F}^* \simeq 13.3$ via Eq. (2.50a). Setting a false-dismissal rate to be 10%, Eq. (2.50b) leads to $\rho \simeq 4.5$. Assuming an isotropically distributed orientation of a pulsar, upper limits on h_0 in a targeted search is theoretically expected to be

$$\langle h_0 \rangle_{p_{\rm FA}=1\%}^{p_{\rm FD}=10\%} \simeq 11.4 \sqrt{\frac{\mathcal{S}}{T_{\rm obs}}}, \tag{2.51}$$

where 90°-interferometers are assumed[20].

[19] We made used of $\langle \left(\langle a^2 \rangle_T + \langle b^2 \rangle_T \right) \rangle_{\alpha,\delta} = 2/5$, $\langle \alpha_1 \rangle_{\cos\iota,\psi} = \langle \alpha_2 \rangle_{\cos\iota,\psi} = 2/5$, and $\langle \alpha_3 \rangle_{\cos\iota,\psi} = 0$.

[20] Equation (2.51) holds true for a targeted search in which only a single template is used. An estimation method for a statistical factor in wide-parameter-space searches without computationally cumbersome Monte-Carlo simulations is found in [61].

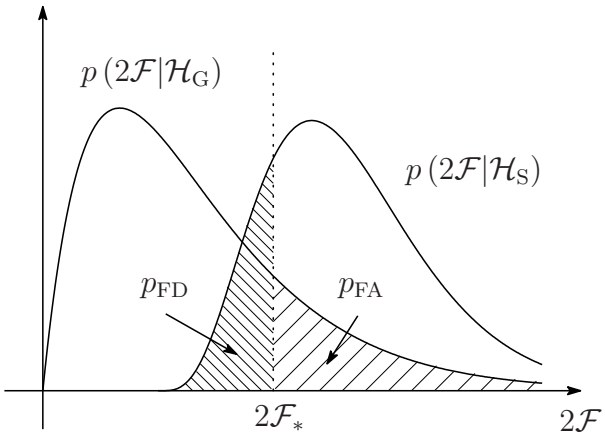

Figure 2.3: Shaded regions depict the areas formed by false-alarm rate and false-dismissal rate. The hypotheses $\mathcal{H}_{\mathrm{G}}$ and $\mathcal{H}_{\mathrm{S}}$ are a Gaussian-noise hypothesis and a signal hypothesis, respectively. The false-alarm rate is the probability that a measured value of the $\mathcal{F}$-statistic exceeds the threshold when the data is consistent with Gaussian noise. The false-dismissal rate is the probability that a measured value of the $\mathcal{F}$-statistic falls below the threshold in spite of the presence of CW signals.

2.4.2 Setting an upper limit on h_0

If the measured value of the $\mathcal{F}$-statistic is not significant, we proceed to place an upper limit on GW strain amplitude. Let $h_0\left(C\right)$ be an upper limit with confidence level C on the overall amplitude h_0. The inverse of $h_0\left(C\right)$ $\left(\equiv h_0^C\right)$ can be expressed as

$$C\left(h_0\right) = \int_{2\mathcal{F}_{\mathrm{obs}}}^{\infty} p\left(2\mathcal{F}|h_0^C\right) d\left(2\mathcal{F}\right), \tag{2.52}$$

where $p\left(2\mathcal{F}|h_0^C\right)$ denotes the PDF of the $\mathcal{F}$-statistic in the presence of the signal whose amplitude is h_0. In terms of the false-dismissal rate, Eq. (2.52) can be written as

$$P_{\mathrm{FD}} = 1 - C = \int_{0}^{2\mathcal{F}_{\mathrm{obs}}} p\left(2\mathcal{F}|h_0^C\right) d\left(2\mathcal{F}\right). \tag{2.53}$$

The upper limit h_0^C with confidence level C can be obtained by solving Eq. (2.53) inversely. However, the non-centrality parameter of the PDF $p\left(2\mathcal{F}|h_0^C\right)$ depends on the unknown waveform parameters, $\alpha, \delta, \cos\iota$ and ψ. To deal with this problem, there are two ways to determine the PDF, $p\left(2\mathcal{F}|h_0^C\right)$ [62]. One is to suppose the most pessimistic situation where the unknown parameters are fixed such that the SNRs take the lowest value. This corresponds to setting the most conservative upper limits. The other is to assume the uniform distributions of the unknown parameters. The PDF is obtained by injecting artificial signals via Monte-Carlo simulations. Here, we employed the latter to estimate the PDF, $p\left(2\mathcal{F}|h_0^C\right)$.

2.4.3 Spin-down ratio

It is useful to introduce spin-down ratio in order to make it clear how far observed upper limits on h_0 are close to physically meaningful quantities. It is defined as the ratio of the observed upper limit to the spin-down limit such as $h_0^{95\%}/h_0^{\rm sd}$. Let us consider the situation where the loss of the rotational kinetic energy of a pulsar is in a state of equilibrium with gravitational-radiation energy. Such a pulsar is often referred to as a gravitar [63]. Since all the rotational energy are converted into the production of the GW, the equation of energy conservation states that

$$\frac{dE_{\rm gw}}{dt} = -\frac{dE_{\rm rot}}{dt}, \tag{2.54}$$

where $E_{\rm gw}$ and $E_{\rm rot}$ represent the gravitational-radiation energy and the loss of the rotational energy, respectively. Concrete expressions for $E_{\rm gw}$ and $E_{\rm rot}$ are given by

$$\frac{dE_{\rm rot}}{dt} = 4\pi^2 I_{zz} f_{\rm rot} \dot{f}_{\rm rot},, \tag{2.55}$$

$$\frac{dE_{\rm gw}}{dt} = \frac{8\pi^2}{5}\frac{c^3 d^2}{G} f_{\rm rot}^2 h_0^2. \tag{2.56}$$

Combining Eqs. (2.54)–(2.56) yields

$$h_0^{\rm sd} = \left(-\frac{5}{2}\frac{GI_{zz}}{c^3 d^2}\frac{\dot{f}_{\rm rot}}{f_{\rm rot}}\right)^{1/2} = 8.06\times10^{-19}\frac{I_{38}^{1/2}}{d_{\rm kpc}}\left(-\frac{\dot{f}_{\rm rot}}{f_{\rm rot}}\right)^{1/2}, \tag{2.57}$$

where $I_{38}^{1/2} = 10^{38}$ kg m^2 and $d_{\rm kpc} = 1$ kpc. It should be noted that $\dot{f}_{\rm rot}$ takes a negative value in general because the loss of the rotational energy brings spin-down to the pulsar[21]. In practice, Eq. (2.54) does not hold in the case of isolated pulsars because measured breaking index n of isolated pulsars is usually less than 5 (e.g. $n \sim 2.5$ for the Crab pulsar [65] and $n \sim 1.4$ for the Vela pulsar [66])[22]. Setting upper limits whose spin-down ratios are less than unity is an important milestone in the field of CW search [14]. So far, the first generation GW detectors consisting of the initial LIGO, the initial Virgo,

[21] A pulsar hosted in a globular cluster is likely to have an acceleration due to the gravitational potential, which would lead to the pulsar's apparent spin-up. The observed spin period $\dot{P}_{\rm obs}$ is related to the intrinsic spin period $\dot{P}_{\rm int}$ by

$$\dot{P}_{\rm obs} = \dot{P}_{\rm int} + \frac{a_\parallel}{c}, \tag{2.58}$$

where $a_\parallel$ denotes the pulsar's acceleration along the line-of-sight [64]. In the case of a binary pulsar, mass accretion from the companion brings the spin-up to the pulsar. Also, a pulsar glitch generally produces an instantaneous spin-up [20].

[22] Breaking index n is defined as $\dot{\omega}_{\rm rot} \propto -\omega_{\rm rot}^n$. In the case of $n = 3$ and 5, the loss of the rotational energy is due to magnetic dipole radiation and gravitational quadrupole radiation, respectively [20].

and the GEO600 have performed targeted searches for a total of 195 known pulsars [62, 67, 64, 68, 69, 70, 14]. The spin-down limits for the Crab and the Vela pulsars have already been beaten by the past searches ($h_0^{95\%}/h_0^{\mathrm{sd}} = 0.11$ for the Crab pulsar and $h_0^{95\%}/h_0^{\mathrm{sd}} = 0.13$ for the Vela pulsar [14]).

2.4.4 Bayesian framework

In this section, a detection statistic is discussed in a Bayesian framework based on [71, 72][23]. Let us consider a binary hypothesis testing problem such that we choose one out of the following two hypotheses:

$$\mathcal{H}_{\mathrm{G}} : \boldsymbol{x}(t) = \boldsymbol{n}(t), \tag{2.59a}$$

$$\mathcal{H}_{\mathrm{S}} : \boldsymbol{x}(t) = \boldsymbol{n}(t) + \boldsymbol{s}(t; \mathcal{A}, \boldsymbol{\lambda}). \tag{2.59b}$$

The Gaussian-noise hypothesis $\mathcal{H}_{\mathrm{G}}$ is a statement that data $\boldsymbol{x}$ comprises of only Gaussian noise $\boldsymbol{n}$, whereas the signal hypothesis $\mathcal{H}_{\mathrm{S}}$ is that data $\boldsymbol{x}$ includes a signal $\boldsymbol{s}$ in addition to Gaussian noise $\boldsymbol{n}$. In order to decide which hypothesis is likely to be correct, the posterior odds ratio between $\mathcal{H}_{\mathrm{S}}$ and $\mathcal{H}_{\mathrm{G}}$ is employed, which is defined as

$$O_{S/G}(\boldsymbol{x}) \equiv \frac{P(\mathcal{H}_{\mathrm{S}}|\boldsymbol{x})}{P(\mathcal{H}_{\mathrm{G}}|\boldsymbol{x})} = \frac{P(\mathcal{H}_{\mathrm{S}})}{P(\mathcal{H}_{\mathrm{G}})} \frac{P(\boldsymbol{x}|\mathcal{H}_{\mathrm{S}})}{P(\boldsymbol{x}|\mathcal{H}_{\mathrm{G}})} = o_{\mathrm{S/G}} B_{\mathrm{S/G}}(\boldsymbol{x}). \tag{2.60}$$

The posterior odds ratio can be computed by means of Bayes' theorem, which results in the prior odds ratio $o_{S/G} \equiv P(\mathcal{H}_{\mathrm{S}})/P(\mathcal{H}_{\mathrm{G}})$ and the Bayes factor $B_{\mathrm{S/G}} \equiv P(\boldsymbol{x}|\mathcal{H}_{\mathrm{S}})/P(\boldsymbol{x}|\mathcal{H}_{\mathrm{G}})$. Equation (2.23) indicates that the amplitude parameters $\mathcal{A}$ and the Doppler parameters $\boldsymbol{\lambda}$ are independent of each other. In particular, in the case of a targeted search, the Doppler parameters $\boldsymbol{\lambda}$ are known to be $\boldsymbol{\lambda}_{\mathrm{sig}}$ a priori by EM observations. Thus, $P(\mathcal{A}, \boldsymbol{\lambda}|\mathcal{H}_{\mathrm{S}}) = P(\mathcal{A}|\mathcal{H}_{\mathrm{S}}) P(\boldsymbol{\lambda}|\mathcal{H}_{\mathrm{S}}) = P(\mathcal{A}|\mathcal{H}_{\mathrm{S}}) \delta(\boldsymbol{\lambda} - \boldsymbol{\lambda}_{\mathrm{sig}})$. Using this relation, the Bayes factor can be computed as follows.

$$\begin{aligned} B_{\mathrm{S/G}}(\boldsymbol{x}) &= \int \frac{P(\boldsymbol{x}|\mathcal{H}_{\mathrm{S}}; \mathcal{A}, \boldsymbol{\lambda})}{P(\boldsymbol{x}|\mathcal{H}_{\mathrm{G}})} P(\mathcal{A}, \boldsymbol{\lambda}|\mathcal{H}_{\mathrm{S}})\, d^4\mathcal{A} d\boldsymbol{\lambda} \\ &= \int \Lambda(\boldsymbol{x}; \mathcal{A}, \boldsymbol{\lambda}_{\mathrm{sig}})\, P(\mathcal{A}|\mathcal{H}_{\mathrm{S}})\, d^4\mathcal{A} \\ &= c_*^{-1} e^{\mathcal{F}(\boldsymbol{x}; \boldsymbol{\lambda}_{\mathrm{sig}})}, \end{aligned} \tag{2.61}$$

[23] Bayesian method of a targeted CW search is presented in [71]. In this paper, an end-to-end search pipeline for known pulsars is constructed and the performance test for multi-detector network is performed numerically. Prix and Krishnan discussed a targeted search in the Bayesian framework and introduced the $\mathcal{B}$-statistic [72]. They discovered the $\mathcal{F}$-statistic as a special case of a Bayes factor on the assumption of uniform priors in amplitude parameters $\mathcal{A}^\mu$. The $\mathcal{B}$-statistic is defined as the Bayes factor with more physical priors in unknown pulsar parameters. They showed that the $\mathcal{B}$-statistic is more powerful than the $\mathcal{F}$-statistic in the sense of the Neyman-Pearson optimality via Monte-Carlo simulations.

where $\Lambda(\boldsymbol{x};\mathcal{A},\boldsymbol{\lambda}_{\rm sig})$ is the likelihood ratio defined in Eq. (2.31a) and c_* is a constant depending on the priors in the amplitude parameters[24]. When integrating the likelihood ratio over the amplitude parameters in (2.61), we made use of Eq. (2.33) and the formula for a multidimensional Gaussian integral[25]. Combining Eqs. (2.65) and (2.61) yields

$$O_{\rm S/G}(\boldsymbol{x};\boldsymbol{\lambda}) = o_{\rm S/G} c_*^{-1} e^{\mathcal{F}(\boldsymbol{x};\boldsymbol{\lambda})}. \tag{2.65}$$

As discussed above, marginalization over the amplitude parameters $\mathcal{A}$ brings the Bayes factor to the $\mathcal{F}$-statistic on the assumption of the uniform priors in $\mathcal{A}$. Since $o_{S/G}$ and c_* are constants, the $\mathcal{F}$-statistic is regarded as an optimal detection statistic[26].

2.5 Wide-parameter-space searches

Thus far, about 2,500 radio pulsars have been discovered by EM observations within our galaxy even though these is only a tiny fraction of all the pulsars [15]. This is because pulsars are very weak radio sources and also because the direction of a beam from a pulsar needs to cross our line-of-sight for EM detection. In fact, the number of electromagnetically undiscovered pulsars within 5 kpc is estimated to be of the order of 10^{6-7} from the birth rate apart from the detectability by ground-based GW detectors [16]. However, a wide-parameter-space search is required to explore unknown CW sources, which entails a labor-intensive search method because the source parameters are unknown completely in advance of observation.

Search methods for GWs are usually based on a matched filtering technique in which

[24] Let the priors in the amplitude parameters obey uniform distributions:

$$P(\mathcal{A}|\mathcal{H}_S) = \begin{cases} \mathcal{C} & h_0(\mathcal{A}) < h_{\rm max}. \\ 0 & \text{otherwise}, \end{cases} \tag{2.62}$$

where $h_{\rm max}$ is introduced as a cut-off parameter to compute the normalization factor $\mathcal{C}$. Using $d^4\mathcal{A} = (1/4)\, h_0^3 \left(1-\cos^2\iota\right)^3 dh_0 d\cos\iota d\psi d\phi_0$, the priors can be normalized as

$$1 = \int P(\mathcal{A}^\mu|\mathcal{H}_S)\, d^4\mathcal{A} = \frac{(2\pi)^2}{70}\mathcal{C} h_{\rm max}^4. \tag{2.63}$$

The constant c_*^{-1} is related to $\mathcal{C}$ by $c_*^{-1} = (2\pi)^2 \mathcal{C}/\sqrt{\det\mathcal{M}}$.

[25] For an n-dimensional real vector $\boldsymbol{x}$, an n-dimenstional real vector $\boldsymbol{J}$, and an $n\times n$ real symmetric matrix M,

$$\int d^n x \exp\left[-\frac{1}{2}\boldsymbol{x}^T M \boldsymbol{x} + \boldsymbol{x}^T \boldsymbol{J}\right] = \sqrt{\frac{(2\pi)^n}{\det M}} \exp\left[\frac{1}{2}\boldsymbol{J}^T M^{-1}\boldsymbol{J}\right], \tag{2.64}$$

where $\det M$ denotes the determinant of M.

[26] Since the constant c^* depends on directions of CW sources through $\det\mathcal{M}$, this factor cannot be neglected in a blind search.

a likelihood function is maximized over unknown parameters in a brute-force way. In the case of CW searches, parameters to be searched over are the Doppler parameters $\boldsymbol{\lambda} = \{\alpha, \delta, f, \dot{f}, \cdots\}$. Thus, there are a large number of signal templates that far exceeds computational resources available to us, as opposed to targeted searches. Each template corresponds to each grid point in waveform-parameter-space. Because of the use of a discrete mesh spanned on the parameter space, search parameters are never perfectly matched with the signal parameters, which leads to the loss of the SNR. Thus, templates are required to be placed densely enough to avoid missing CW signals. Template placement is often carried out by using a signal-template mismatch that is a fractional loss of a SNR,

$$\mathcal{M} \equiv \frac{\rho^2(\mathbf{0}) - \rho^2(\Delta\boldsymbol{\lambda})}{\rho^2(\mathbf{0})}, \tag{2.66}$$

where $\Delta\boldsymbol{\lambda}$ denotes the difference between the signal and template and is defined as $\Delta\boldsymbol{\lambda} \equiv \boldsymbol{\lambda}_{\rm sig} - \boldsymbol{\lambda}$. Grid spacings are determined so that the largest mismatch between any putative signal and the closest template falls within a predetermined tolerance level. In what follows, we see an enormous computational burden in the fully coherent $\mathcal{F}$-statistic search for unknown pulsars, and then we explain alternative search methods that allow us to explore a wide-parameter-space at the cost of sensitivity.

2.5.1 Computational costs for wide-parameter-space searches

Constant amplitude model

To simplify the following discussion, it is useful to introduce a constant-amplitude model in which time-dependencies in antenna-pattern functions are neglected. This simplified model can be justified by the fact that $F_{+,\times}$ varies on the time scale of a day whereas the phase $\Phi(t)$ oscillates on a time scale of $1/f_0$. Also, coherent-integration time is typically set to be longer than a day. By reference to Eq. (2.12), the constant-amplitude waveform is taken in the following form [56, 73]:

$$s(t) = A_+ \cos\Phi(t) + A_\times \sin\Phi(t), \tag{2.67}$$

where the constants $F_{+,\times}$ are absorbed into h_0. In Eq. (2.67), there are two unknown amplitude parameters $A_{+,\times}$. The $\mathcal{F}$-statistic is defined as the maximum value of the log-likelihood ratio over the amplitude parameters,

$$2\mathcal{F} = \max_{A_+, A_\times} 2\ln\Lambda = \frac{4T}{\mathcal{S}} \left|\langle x e^{-i\phi}\rangle_T\right|^2, \tag{2.68}$$

where $\langle\cdots\rangle_T$ denotes the time average over coherent-integration time T[27]. When the CW waveform is perfectly known and is expressed as $s_{\rm sig} = A_{+,\rm sig}\cos\Phi_{\rm sig} + A_{\times,\rm sig}\sin\Phi_{\rm sig}$, $2\mathcal{F}$ satisfies the following relation,

$$\langle 2\mathcal{F}\rangle = 2 + \rho^2(\mathbf{0}), \tag{2.71a}$$

$$\rho^2(\mathbf{0}) \equiv \frac{4T}{\mathcal{S}}\left|\langle s_{\rm sig}e^{-i\phi_{\rm sig}}\rangle\right|^2 \simeq \frac{T}{\mathcal{S}}\left(A^2_{+,\rm sig} + A^2_{\times,\rm sig}\right). \tag{2.71b}$$

Note that $2\mathcal{F}$ in the constant amplitude model follows the chi-squared distribution with two degrees of freedom unlike Eq. (2.44a). This statistical difference arises from the number of unknown amplitude parameters.

Signal-template mismatch

Next, let us focus on the case where there exists a signal-template mismatch, $\Delta\boldsymbol{\lambda} = \boldsymbol{\lambda}_{\rm sig} - \boldsymbol{\lambda}$. In a similar way to the perfectly matched case, an expectation value of $2\mathcal{F}$ is calculated as

$$\langle 2\mathcal{F}\rangle = 2 + \rho^2(\Delta\boldsymbol{\lambda}), \tag{2.72a}$$

$$\rho^2(\Delta\boldsymbol{\lambda}) \equiv \frac{4T}{\mathcal{S}}\left|\langle s_{\rm sig}e^{-i\phi}\rangle_T\right|^2 = \rho^2(\mathbf{0})\left|\langle e^{-i\Delta\phi}\rangle_T\right|^2. \tag{2.72b}$$

Grid points on the parameter space are placed closely to each other, so that the mismatch

[27] The log-likelihood ratio defined in Eq. (2.30) can be reduced to the following equations,

$$\begin{aligned}\ln\Lambda &= \frac{2T}{\mathcal{S}}\left[\langle xs\rangle_T - \frac{1}{2}\langle s^2\rangle_T\right] = \frac{2T}{\mathcal{S}}\left[A_+\langle x\cos\Phi\rangle_T + A_\times\langle x\sin\Phi\rangle_T - \frac{1}{4}\left(A^2_+ + A^2_\times\right)\right]\\ &= \frac{2T}{\mathcal{S}}\left[-\frac{1}{4}\left(A_+ - 2\langle x\cos\Phi\rangle_T\right)^2 - \frac{1}{4}\left(A_\times - 2\langle x\sin\Phi\rangle_T\right)^2 + \langle x\cos\Phi\rangle^2_T + \langle x\sin\Phi\rangle^2_T\right],\end{aligned} \tag{2.69}$$

where $\langle\cos^2\Phi\rangle_T \simeq \langle\sin^2\Phi\rangle_T \simeq 1/2, \langle\cos\Phi\sin\Phi\rangle_T \simeq 0$ were employed. The $\mathcal{F}$-statistic is defined as the maximum value of the log-likelihood ratio over the amplitude parameters A_+ and $A_\times$,

$$2\mathcal{F} = \max_{A_+,A_\times} 2\ln\Lambda = \frac{4T}{\mathcal{S}}\left[\langle x\cos\Phi\rangle^2_T + \langle x\sin\Phi\rangle^2_T\right] = \frac{4T}{\mathcal{S}}\left|\langle xe^{-i\Phi}\rangle_T\right|^2. \tag{2.70}$$

Since the above equation is independent of the constant GW phase, Φ can be replaced by ϕ.

$\mathcal{M}$ can be expanded up to the second order of $\Delta\boldsymbol{\lambda}$ as[28]

$$\mathcal{M} = \frac{\rho^2(\mathbf{0}) - \rho^2(\Delta\boldsymbol{\lambda})}{\rho^2(\mathbf{0})} = g_{ab}\Delta\lambda^a\Delta\lambda^b + \left[(\Delta\boldsymbol{\lambda})^3\right], \tag{2.75a}$$

$$g_{ab} \equiv \langle\partial_a\phi_{\rm sig}\partial_b\phi_{\rm sig}\rangle_T - \langle\partial_a\phi_{\rm sig}\rangle_T\langle\partial_b\phi_{\rm sig}\rangle_T, \tag{2.75b}$$

$$\partial_a\phi_{\rm sig} \equiv \frac{\partial\phi}{\partial\lambda^a}\bigg|_{\boldsymbol{\lambda}=\boldsymbol{\lambda}_{\rm sig}}, \tag{2.75c}$$

where $\partial_a\phi_{\rm sig}$ is derivatives of ϕ with respect to the Doppler parameters $\lambda^a = \{\alpha, \delta, f, \dot{f}, \cdots\}$, followed by evaluation at $\boldsymbol{\lambda} = \boldsymbol{\lambda}_{\rm sig}$. Equation (2.75a) indicates that a geometric interpretation can be formulated for a signal-template mismatch. The mismatch can be interpreted as a distance between a signal and a template in waveform-parameter-space defined by a metric [74, 75]. In the constant-amplitude model, the metric g_{ab} is expressed only by derivatives of the phase as in Eq. (2.75b), and so is often referred to as the phase metric first introduced in [76][29].

Number of signal templates

A template bank that is a set of waveform templates is required for exploring wide parameter space. In template-based searches, a template bank is constructed so that the risk of missing a GW signal is minimized based on a metric[30]. In other words, grid

[28] The GW phase ϕ is expanded in a Taylor series in powers of $(\boldsymbol{\lambda} - \boldsymbol{\lambda}_{\rm sig})^a$ as

$$\begin{aligned}
&\phi(\boldsymbol{\lambda}) = \phi_{\rm sig} + (\boldsymbol{\lambda} - \boldsymbol{\lambda}_{\rm sig})^a\,\partial_a\phi\Big|_{\boldsymbol{\lambda}=\boldsymbol{\lambda}_{\rm sig}} + \frac{1}{2}(\boldsymbol{\lambda} - \boldsymbol{\lambda}_{\rm sig})^a(\boldsymbol{\lambda} - \boldsymbol{\lambda}_{\rm sig})^b\,\partial_a\partial_b\phi\Big|_{\boldsymbol{\lambda}=\boldsymbol{\lambda}_{\rm sig}} + \cdots \\
&\Rightarrow \Delta\phi = \Delta\lambda^a\partial_a\phi_{\rm sig} - \frac{1}{2}\Delta\lambda^a\Delta\lambda^b\partial_a\partial_b\phi_{\rm sig} + \cdots \\
&\Rightarrow e^{i\Delta\phi} = 1 + i\left(\Delta\lambda^a\partial_a\phi_{\rm sig} - \frac{1}{2}\Delta\lambda^a\Delta\lambda^b\partial_a\partial_b\phi_{\rm sig}\right) - \frac{1}{2}\Delta\lambda^a\Delta\lambda^b\partial_a\phi_{\rm sig}\partial_b\phi_{\rm sig} + \cdots,
\end{aligned} \tag{2.73}$$

where ∂_a denotes a derivative with respect to the phase parameters $\boldsymbol{\lambda}$. So, the mismatch $\mathcal{M}$ can be expressed up to the second order of $\Delta\boldsymbol{\lambda}$ as

$$\begin{aligned}
\mathcal{M} &= 1 - \left|\langle e^{i\Delta\phi}\rangle\right|^2 = 1 - \left|1 + i\left(\Delta\lambda^a\langle\partial_a\phi_{\rm sig}\rangle - \frac{1}{2}\Delta\lambda^a\Delta\lambda^b\langle\partial_a\partial_b\phi_{\rm sig}\rangle\right) - \frac{1}{2}\Delta\lambda^a\Delta\lambda^b\langle\partial_a\phi_{\rm sig}\partial_b\phi_{\rm sig}\rangle\right|^2 + \cdots \\
&= 1 - \left[\left(1 - \frac{1}{2}\Delta\lambda^a\Delta\lambda^b\langle\partial_a\phi_{\rm sig}\partial_b\phi_{\rm sig}\rangle\right)^2 + \left(\Delta\lambda^a\langle\partial_a\phi_{\rm sig}\rangle - \frac{1}{2}\Delta\lambda^a\Delta\lambda^b\langle\partial_a\partial_b\phi_{\rm sig}\rangle\right)^2\right] + \cdots \\
&= \left(\langle\partial_a\phi_{\rm sig}\partial_b\phi_{\rm sig}\rangle - \langle\partial_a\phi_{\rm sig}\rangle\langle\partial_b\phi_{\rm sig}\rangle\right)\Delta\lambda^a\Delta\lambda^b + \mathcal{O}\left[(\Delta\boldsymbol{\lambda})^3\right].
\end{aligned} \tag{2.74}$$

[29] General parameter space metric of multidetector $\mathcal{F}$-statistic is derived in [77]. Using this multidetector metric, the parameter resolutions are proven to have nothing to do with the number of detectors. Multidetector $\mathcal{F}$-statistic metric is also discussed in the context of short-duration non-precessing inspiral GW signals in [78, 79].

[30] Efficient template placements in flat parameter spaces with constant-coefficient metrics are discussed in [80]. The construction method for efficient template banks can be cast into the sphere covering problem. For low-dimension parameter space $n \lesssim 24$, (nearly) optimal template banks are provided by

points in waveform parameter space $\mathcal{P}$ are placed so that the mismatch between the signal point $\boldsymbol{\lambda}_{\rm sig}$ and the nearest grid point $\boldsymbol{\lambda}$ falls within a predetermined acceptable maximal mismatch $\mathcal{M}_{\rm max}$. Every point in parameter space $\mathcal{P}$ satisfies $g_{ab}\Delta\lambda^a\Delta\lambda^b \leq \mathcal{M}_{\rm max}$. A template bank placed on the parameter space is usually taken in the form of lattice. So, the proper volume and the number of templates are evaluated as

$$V = \int_{\mathcal{P}} dV = \int_{\mathcal{P}} \sqrt{\det g}\, d\boldsymbol{\lambda}, \tag{2.76a}$$

$$\mathcal{N} \simeq \frac{V}{V_0\left(\mathcal{M}_{\rm max}\right)}, \tag{2.76b}$$

where $\det g$, V_0, and $\mathcal{N}$ denote the determinant of the metric g_{ab}, the volume covered by a single template that depends on the maximal mismatch $\mathcal{M}_{\rm max}$, and the number of the templates, respectively. In the case of fully coherent $\mathcal{F}$-statistic based search, a parameter space metric is given by Eq. (2.75b). Using Eqs. (2.16b) and (2.75c), derivatives of the phase ϕ with respect to the Doppler parameters are

$$\partial_{f^{(k)}}\phi\left(t\right) = 2\pi\frac{\left[\Delta\tau\right]^{k+1}}{(k+1)!} \sim t^{k+1}, \quad \partial_{n^i}\phi\left(t\right) = 2\pi\frac{r^i}{c}\sum_{k=0}^{s}\frac{f^{(k)}}{k!}\left[\Delta\tau\right]^k \sim \frac{f r^i_{\rm orb}}{c}, \tag{2.77}$$

where the coherent-integration time is assumed to be $T \ll 1$ year and $\boldsymbol{r}_{\rm orb}$ is the position vector describing the orbital motion around the Sun. Each component of the phase metric defined by Eq. (2.75b) is of the order of

$$g_{f^{(k)}f^{(k')}} \sim T^{k+1}T^{k'+1}, \quad g_{n^in^j} \sim \left(\frac{f v_{\rm orb} T}{c}\right)^2 e^i e^j, \quad g_{n^i f^{(k)}} \sim \frac{f T v_{\rm orb}}{c} T^{k+1} e^i, \tag{2.78}$$

where e^i is the unit vector along the orbital velocity $v_{\rm orb}$. The determinant of the metric is evaluated as

$$\sqrt{\det g} \sim f^2\mathcal{O}\left(T^2\right)\prod_{k=0}^{s} T^{k+1}. \tag{2.79}$$

From the above discussion, if spin-down parameters are taken into account up to the first order $s = 1$, the number of the templates scales with $\mathcal{N} \sim T^5$. Thus, the number of templates increases with the coherent-integration time polynomially. Computational costs for wide-parameter-space searches based on the fully coherent $\mathcal{F}$-statistic easily overwhelm existing computational resources available to us.

the A_n^* lattice [81]. However, such a template-based search method is known to be inefficient in higher dimensions. To overcome this problem, random template banks are proposed in which templates are placed uniformly randomly over the parameter space [82].

2.5.2 Semi-coherent search

As discussed in the previous section, we cannot perform the most optimal search method based on the fully coherent $\mathcal{F}$-statistic in the case of unknown CW searches because of lack of computational resources. Thus, a suboptimal strategy based on a semi-coherent search must be adopted. Because computational cost for search and the corresponding sensitivity have a trade-off relationship, large waveform-parameter-space can be explored efficiently by sacrificing sensitivity[31].

The simplest semi-coherent search method is achieved by incoherent sum of Fourier powers over all the SFT segments. The whole observation data is divided up into shorter segments, and subsequently each segment is Fourier transformed by SFTs. Detection statistics is basically constructed by use of incoherent combination of the SFT powers. The time baseline of SFTs, T_{SFT}, is determined so that the power of a putative signal does not leak into the adjacent frequency bins by the signal's Doppler shift during T_{SFT}. Also, the time baseline should be short enough for detector noise to be regarded as stationary within a single SFT segment. The length of SFT is typically taken to be 30 min.

There are three types of SFT-based semi-coherent methods that were commonly used in the initial LIGO [84, 85]: StackSlide method [86, 87], Hough method [88, 83, 89], and PowerFlux method [90, 91]. For example, the StackSlide approach uses the total power P_k as a detection statistic, which is defined as

$$P_k \equiv \frac{1}{N_{\mathrm{SFT}}} \sum_{\alpha=1}^{N_{\mathrm{SFT}}} \rho^2_{k,\alpha}, \tag{2.81a}$$

$$\rho^2_{k,\alpha} = \frac{2\left|\tilde{x}_{k,\alpha}\right|^2}{T_{\mathrm{SFT}} S_{k,\alpha}}, \tag{2.81b}$$

where $\rho^2_{k,\alpha}$ denotes the normalized SFT power contained in the k-th frequency bin of the α-th SFT segment. The normalization factor in Eq. (2.81b) is chosen so that the expectation value of $\rho^2_{k,\alpha}$ is unity when the data is comprised of only the Gaussian noise (see Eq. (A.2)). As illustrated in Fig. 2.4, the frequency bin that contains a putative CW signal varies with time due to the Doppler shift and the spin-down of the source. In order to accumulate the SNR efficiently, the SFT powers are summed up incoherently along the path of In order to accumulate the SNR efficiently, the SFT powers are summed

[31] For example, the sensitivity of the $\mathcal{F}$-statistic-based Hough method is expressed as

$$h_0 = \frac{8.92}{N_{\mathrm{seg}}^{1/4}} \sqrt{\frac{S_n}{T_{\mathrm{seg}}}} = 8.92 N_{\mathrm{seg}}^{1/4} \sqrt{\frac{S_n}{T_{\mathrm{obs}}}}, \tag{2.80}$$

where the false-alarm rate and false-dismissal rate are assumed to be 1% and 10%, respectively [83]. Comparing Eq. (2.51), for the same value of T_{obs}, the sensitivity decreases as $N_{\mathrm{seg}}^{-1/4}$.

up incoherently along the path of frequency bins of the putative signal described by Eq. (2.22a).

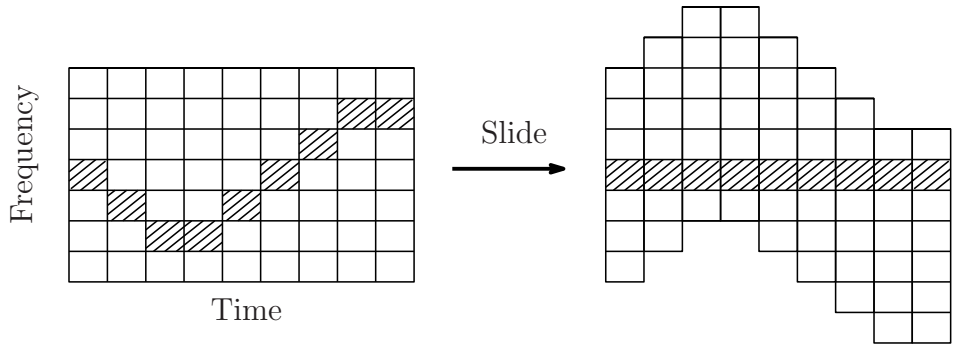

Figure 2.4: A schematic view of semi-coherent search methods. Each row corresponds to a frequency bin and each column corresponds to a SFT segment. The pixels that contain a putative CW signal are filled with diagonal lines. The signal frequency shifts are caused by the Doppler effects and the intrinsic time evolution of the CW frequency.

Recent advances in computing power make it possible to perform a $\mathcal{F}$-statistic-based semi-coherent search method. An year-long observation data is split up into shorter segments of the order of a day that is much longer than the case of SFT-based semi-coherent methods. The $\mathcal{F}$-statistic is computed from each segment on a coarse grid of templates. Then, resulting $\mathcal{F}$-statistics are summed up over all the segments incoherently on a common fine grid of templatese. In a similar way to the StackSlide method, a detection statistic consists of incoherent sum of the $\mathcal{F}$-statistics along the path of the putative CW signal,

$$\overline{2\mathcal{F}} \equiv \frac{1}{N_{\mathrm{seg}}} \sum_{j=1}^{N_{\mathrm{seg}}} 2\mathcal{F}_j, \tag{2.82}$$

where $\mathcal{F}_j$ denotes the $\mathcal{F}$-statistic computed from the j-th coherent segment.

Chapter 3

Low-frequency all-sky CW search with TOBA

Large-scale laser interferometric GW detectors such as aLIGO [92], Advanced Virgo [93], and KAGRA [12] are now constructed or are being constructed around the world. A network of these advanced ground-based GW detectors will reach unprecedented sensitivity which may be enough to establish GW astronomy. However, low-frequency GW band below about 10 Hz cannot be explored by the currently existing laser interferometers because the sensitivities of detectors to GWs are hampered by seismic noise on the Earth. One of the solutions to avoid noise due to the ground motion is to construct GW detectors formed by satellites in space such as the evolved LISA (eLISA) [94] and the DECi-hertz Interferometer Gravitational wave Observatory (DECIGO) [95]. Another solution is to devise detector configurations on the Earth such as the torsion-bar antenna (TOBA) [96], atomic interferometers [97], the juggled interferometer [98], and the full-tensor detector [99].

A TOBA is a terrestrial low-frequency GW detector that is composed of two orthogonal bar-shaped test masses [96]. When a GW passes through the detector, the two bars rotate differentially around their centers. GW signals can be read by measuring the bar rotations on the horizontal plane. The main feature of the TOBA is a good sensitivity at low frequencies around 1 Hz even on the ground thanks to its low resonant frequency in the rotational degrees of freedom. So far, the prototype TOBA was used to set upper limits on the amplitude of the stochastic GW background [100, 101, 102]. In the subsequent work, a new detector configuration for a TOBA was introduced by incorporating two additional detector outputs by measuring the rotations of the bars on the vertical planes [103, 104]. Such a multi-output TOBA can be regarded as a network of three coincident but misaligned interferometric detectors.

In this chapter, we give an overview of our work on how much the new detector configuration improves parameter estimation accuracies for GW detections. Subsequently, we perform an all-sky CW search in a low-frequency region using data from a Phase-II TOBA that is a prototype detector of the multi-output TOBA.

The outline of this chapter is as follows. In section 3.1, a concept of a TOBA is

summarized and a new detector configuration for a TOBA is introduced. We study accuracy of parameter estimation using the Fisher analysis. In section 3.2, we report the results of an all-sky CW search in a low-frequency region using the Phase-II TOBA data. This chapter is basically based on [17] and [18].

3.1 Multi-output TOBA and its performance

3.1.1 TOBA

A TOBA is a ground-based detector for low-frequency GWs, and was originally proposed in [96]. A TOBA consists of two bar shaped orthogonal test masses to which mirrors are attached at both ends as can be seen in Fig. 3.1. The two bars rotate differentially on the xy plane due to the passage of incident GWs. The GW signals can be read in the following way. An input laser beam is split into two orthogonal beams at a beam splitter. The two beams are reflected by the mirrors attached to the ends of the bars and are recombined at the beam splitter. The GW signals can be obtained by measuring the optical path differences at a PD placed in a different direction from the laser. The angular motions of the bars are written as follows:

$$I\ddot{\theta}\left(t\right)+\gamma_{\theta}\dot{\theta}\left(t\right)+\kappa_{\theta}\theta\left(t\right)=\frac{1}{4}\ddot{h}_{jk}q_{\theta}^{jk}, \tag{3.1}$$

where we denote the moment of inertia, the dissipation coefficient, the spring constant, and the dynamical quadrupole moment of the two bars by I, γ_θ, κ_θ, and q_θ^{jk}, respectively. The spring constant is written as $\kappa_\theta = mga^2/\ell$, where ℓ and a denote the length of the suspension wire and the distance between two holes for the suspension wires, respectively. When the time-dependence of the antenna pattern functions is negligible, Eq. (3.1) in the Fourier domain can be expressed as

$$\tilde{\theta}\left(\omega\right)=\sum_{A=+,\times}H_{\theta}^{A}\left(\omega\right)\tilde{h}_{\mathrm{TT}}^{A}, \tag{3.2a}$$

$$H_{\theta}^{A}\left(\omega\right)\equiv\frac{q_{\theta}^{A}}{2I}\frac{\omega^{2}}{\omega^{2}-\omega_{\mathrm{res},\theta}^{2}\left(1+i\varphi\right)-i\omega\gamma/I}, \tag{3.2b}$$

where φ is the loss angle arising from internal friction and $\omega_{\mathrm{res},\theta} = 2\pi f_{\mathrm{res},\theta} \equiv \sqrt{\kappa_\theta/I}$ is the resonant frequency in the θ degree of freedom . Since the resonant frequency can be set below 1 Hz, a TOBA is sensitive to low-frequency GWs.

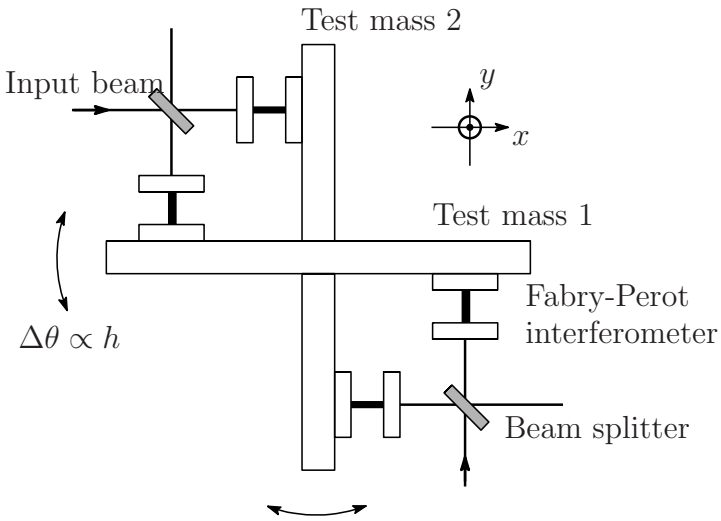

Figure 3.1: Layout of a TOBA detector that is composed of two orthogonal bar-shaped test masses. Tidal force due to GWs induces differential rotations of the bars on the xy plane. The angular fluctuations $\Delta\theta$ of the bars correspond to the GW amplitude h. GW signals are read by a laser interferometer in a similar way to the conventional interferometric GW detectors.

3.1.2 Multi-output system

As discussed in the previous section, the originally proposed TOBA monitors angular motions of the bar-shaped test masses on the xy plane. In [17, 103], a new detector configuration for a TOBA is introduced by adding two other outputs that are obtained from rotations of the bars on the vertical planes. Hence, the GW signals can be read from the rotations of the bars on the xy, yz, and zx planes as shown in Fig. 3.2. Similarly to Eq. (3.1), the EOM of the bar in the ϕ degree of freedom is expressed by

$$I\ddot{\phi}(t) + \gamma_\phi \dot{\phi}(t) + \kappa_\phi \phi(t) = \frac{1}{4}\ddot{h}_{jk} q_\phi^{jk}. \tag{3.3}$$

The spring constant in the ϕ degree of freedom is written as $\kappa_\phi = mgd$, where d is the distance between the center of mass of the bar and its suspension point. The resonant frequency is $f_{\mathrm{res},\phi} = \sqrt{\kappa_\phi / I}/2\pi$ above which the bar-shaped test masses are sensitive to GW (see [17, 103] for more details). Because of $\theta_2 = -\theta_1$, we have three independent output signals, $s_{\mathrm{I}} = \theta_1 - \theta_2, s_{\mathrm{II}} = \phi_1$, and $s_{\mathrm{III}} = \phi_2$. Antenna responses to GW for each detector output are given in Appendix C.2.2 . Figure 3.3 depicts antenna pattern power defined by $P(\alpha, \delta) = \sum_i \left(F_i^{+2} + F_i^{\times 2}\right)$. The summation is taken over the three outputs I, II and III. This figure indicates that the multi-output TOBA has no blind direction, and so its sensitivity is much more uniform than the conventional single-output TOBA.

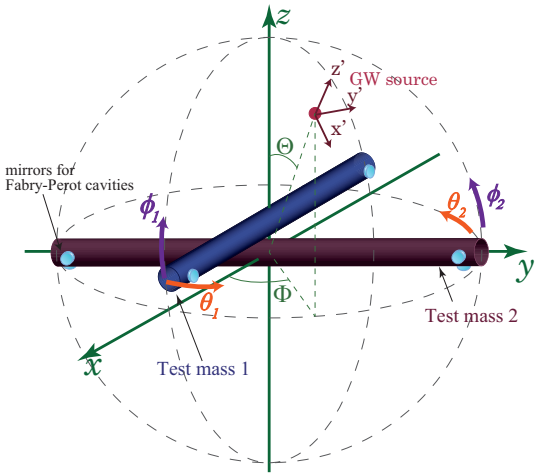

Figure 3.2: Layout of the multi-output TOBA. The two bar-shaped test masses can move independently in the directions of the x, y, and z axes. The three independent output signals can be obtained by monitoring the bar motions on the xy, xz, and yz planes (from [17]).

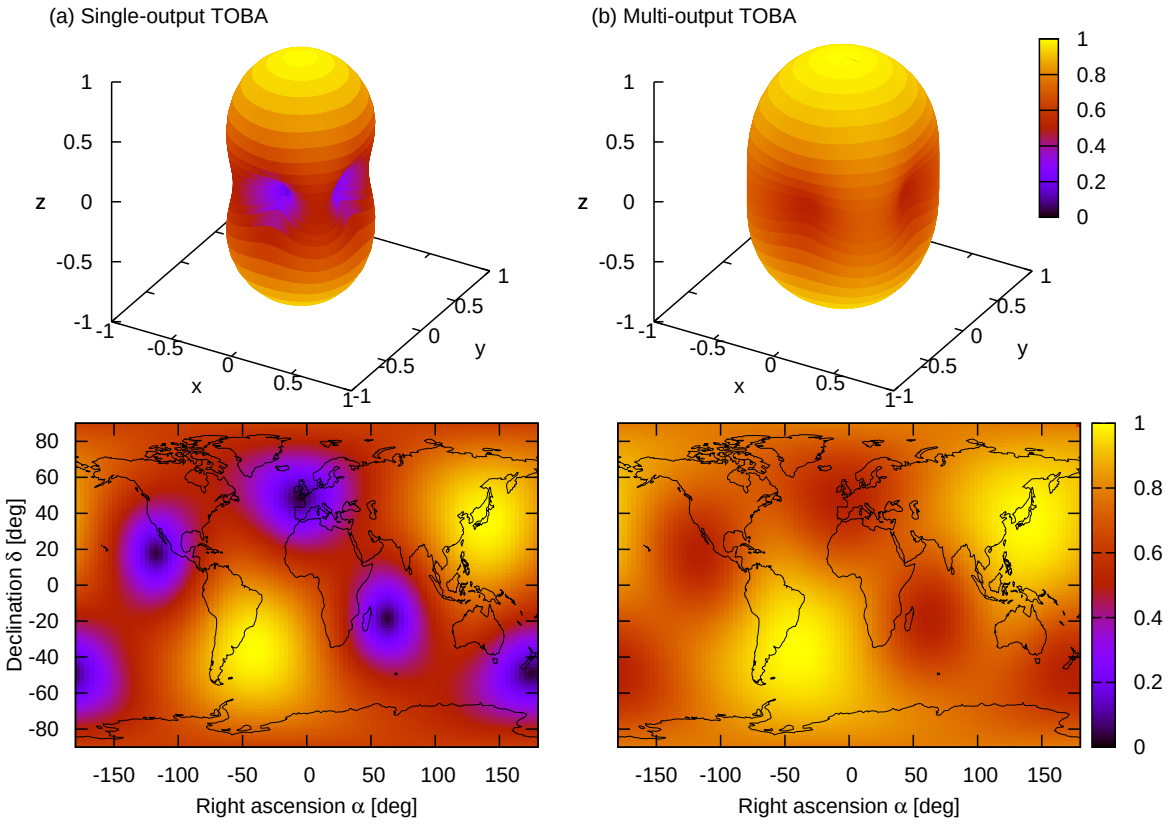

Figure 3.3: Square root of the antenna power pattern $\sqrt{P(\alpha, \delta)}$ for the single-output TOBA (left panel) and the multi-output TOBA (right panel). The detectors are assumed to be located at the TAMA300's site in Japan (35° 40′ 36″ N, 139° 32′ 10″ E).

3.1.3 Accuracy of parameter estimation

In the following, we study how accurately we estimate a source location using a multi-output TOBA and also examine the estimation accuracy of the other waveform parameters. For this purpose we consider two nominal sources, monochromatic sources and intermediate-mass black hole (IMBH) binary coalescences. First, we examine the case of the monochromatic source for a fixed SNR in order to reveal how the multi-output configuration improves the parameter resolution apart from the improved SNR. This examination gives an insight into the result of the IMBH mergers case. Then, we move on to discussions about IMBH mergers at a fixed distance, which are more realistic targets of a TOBA. In what follows, we make the simplifying assumptions that noise of each detector is uncorrelated with each other and that each sensitivity can be expressed as the same form. In this case, the noise spectrum matrix $\boldsymbol{S}_n(f)$ has only diagonal elements all of which can be written by the same form $S_n(f)$.

The case of monochromatic sources

Monochromatic GW with a frequency f_0 can be expressed by Eqs. (2.10) and (2.11b). Combining Eqs. (2.10) and (2.12), we find the detector response to a monochromatic source as

$$h_{Xi}(t) = A_{Xi}(t)\cos\left[\Phi_{Xi}(t)\right], \tag{3.4a}$$

$$A_{Xi}(t) = h_0 Q_{Xi}(t), \tag{3.4b}$$

$$Q_{Xi}(t) = \left[\left(\frac{1+\cos^2\iota}{2}\right)^2 {F_{Xi}^{+}}^2(t) + \cos^2\iota {F_{Xi}^{\times}}^2(t)\right]^{1/2}, \tag{3.4c}$$

$$\Phi_{Xi}(t) = 2\pi f_0 t + \varphi_0 + \varphi_{\mathrm{pol},Xi}(t) + \varphi_{\mathrm{Dop},X}(t), \tag{3.4d}$$

$$\varphi_{\mathrm{pol},Xi}(t) = \arctan\left[-\frac{2\cos\iota}{1+\cos^2\iota}\frac{F_{Xi}^{\times}(t)}{F_{Xi}^{+}(t)}\right], \tag{3.4e}$$

$$\varphi_{\mathrm{Dop},X}(t) = 2\pi f_0 \frac{\hat{\boldsymbol{n}}\cdot\boldsymbol{r}_X(t)}{c}, \tag{3.4f}$$

where the suffixes "Xi" stand for the i-th output in the X-th detector. The phase shift $\varphi_{\mathrm{Dop},X}(t)$ is called the Doppler phase because it comes from the Doppler correction[1]. The phase shift $\varphi_{\mathrm{pol},Xi}(t)$ is often referred to as the polarization phase that depends

[1] The inner product $\hat{\boldsymbol{n}}\cdot\boldsymbol{r}(t)$ is written as

$$\begin{aligned}\hat{\boldsymbol{n}}\cdot\boldsymbol{r}(t) = {} & R_{\mathrm{ES}}\left[\cos\alpha\cos\delta\cos\left(\phi_{0,\mathrm{orb}}+\Omega_{\mathrm{orb}}t\right) + \left(\cos\epsilon\sin\alpha\cos\delta+\sin\epsilon\sin\delta\right)\sin\left(\phi_{0,\mathrm{orb}}+\Omega_{\mathrm{orb}}t\right)\right] \\ & + R_{\mathrm{E}}\left(\sin\delta_D\sin\delta+\cos\delta_D\cos\delta\cos\left[\alpha-\alpha_D(t)\right]\right),\end{aligned} \tag{3.5}$$

where $\alpha_D(t)$ and δ_D represent the detector position at time t [57]. The symbols Ω_{orb} and ϵ denote the angular speed of the Earth's revolution around the Sun and the Earth's axial tilt, respectively.

on the angular pattern functions $F_{+,\times}$ [105]. The GW signal is characterized by the seven waveform parameters $\{h_0, f_0, \varphi_0, \alpha, \delta, \psi, \cos\iota\}$. Substituting Eqs. (3.4a)−(3.4f) into Eqs. (D.4) and (D.5), we evaluate the accuracy of the parameter estimation accuracy using the Fisher analysis (see Appendix D for more details).

The left panel of Fig. 3.4 shows the angular resolution in the case of a single detector located at the TAMA300's site in Japan. This figure indicates that there is no difference between two curves for $T_{\rm obs} > 1$ day. For $T_{\rm obs} > 1$ day, the error $\Delta\Omega$ drops with the time and approaches to the diffraction-limited accuracy [106],

$$\Delta\Omega_{\rm diff} = \frac{c^2}{f_0^2 \rho^2 \pi R_{\rm ES}^2 |\sin i|} = 2.5 \times 10^{-8}\ {\rm sr} \left(\frac{1\ {\rm Hz}}{f_0}\right)^2 \left(\frac{1/\sqrt{2}}{|\sin i|}\right) \left(\frac{10}{\rho}\right)^2, \tag{3.6}$$

where ρ is the total SNR and i is the angle between the normal to the ecliptic plane and the direction of incident GW [107]. This is because $\Delta\Omega$ is mainly determined by the Doppler effect caused by the Earth's orbital motion. The deviation between the two curves appears in the short-duration signals (less than 1 day). The error $\Delta\Omega$ in the single-output TOBA decreases with time for $T_{\rm obs} \gtrsim 10^4$ seconds due to the Doppler effect caused by the Earth's rotation. For $T_{\rm obs} \lesssim 10^4$ seconds, the sky location of the source cannot be determined at all. In contrast, $\Delta\Omega$ in the multi-output TOBA is of the order of 0.1 steradians and remains approximately constant even in the short-duration signals with SNR = 10 (less than 1 day). This feature can be traced to the polarization phase $\varphi_{{\rm pol},Xi}$. In the case of the multi-output configuration, the degeneracy of the two polarization modes is broken as opposed to the single-output one because the three independent output signals can be obtained. Hence, the angular resolution of the multi-output TOBA for short-duration signals is much better than that of the single-output TOBA thanks to the information on the polarization.

The right panel of Fig. 3.4 shows the angular resolution in the case of a three-detector network. Each detector is assumed to be located at the site of TAMA300 (Japan), LIGO-Hanford (US) and Virgo (Italy). In Fig. 3.4, the two curves coincide with each other for long-duration signals (more than 1 day) due to the Doppler effects. This behavior is the same as the single-detector case. On the other hand, $\Delta\Omega$ for both the single and multi output configurations are constants below 10^4 seconds because the polarization phase $\varphi_{{\rm pol},Xi}$ determines the angular resolutions. It should be noted that $\Delta\Omega$ of low-frequency detectors for short-duration signals (less than about 1 day) is controlled by much different factors than the conventional ground-based detectors. The angular resolution of a network of ground-based detectors sensitive to above 10 Hz is mainly determined by the error of the delays of the arrival time [108]. It is roughly estimated by the geometrical formula

derived by Wen and Chen [107],

$$\Delta\Omega = 1.8 \times 10^{-3}\ \mathrm{sr} \left(\frac{100\ \mathrm{Hz}}{f_0}\right)^2 \left(\frac{3 \times 10^{13}\ \mathrm{m}^2}{S}\right) \left(\frac{1/\sqrt{2}}{\cos i}\right) \left(\frac{10}{\rho_{\mathrm{tot}}}\right)^2 \left(\frac{\rho_{\mathrm{tot}}^3/\rho_1\rho_2\rho_3}{3\sqrt{3}}\right), \tag{3.7}$$

where S is the area formed by the three-detector network, ρ_{tot} is the total SNR, ρ_i is the SNR achievable with the i-th detector alone, and i is the angle between the normal to the plane defined by the detector network and the direction of GW propagation[2]. This formula does not work when applied to low-frequency GW detectors because the directional derivatives of the pattern functions are neglected in the derivation of Eq. (3.7). When low-frequency GW source is localized by ground-based detectors, the polarization phases $\varphi_{\mathrm{pol},Xi}$ play a key role in the angular resolution.

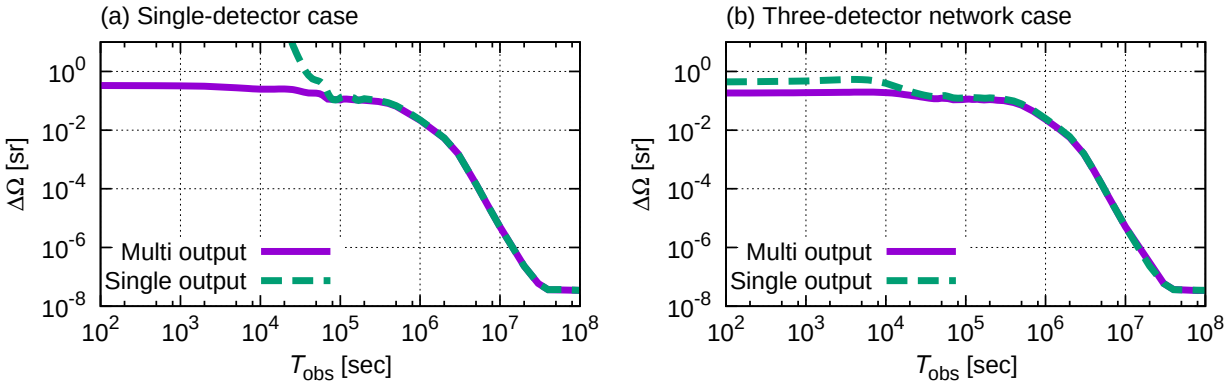

Figure 3.4: Angular resolution $\Delta\Omega$ as a function of observation time T_{obs} for monochromatic sources with $f_0 = 1$ Hz. Angular parameters are set to be $\alpha = \delta = \iota = \psi = 1.0$ radians. The amplitudes of GW signals are normalized by SNR $= 10$. The solid line and the dashed line correspond to a multi-output TOBA and a single-output TOBA, respectively.

The case of IMBH-IMBH binary coalescences

Next, we consider a coalescing binary system composed of two point masses with m_1 and m_2 as a GW source. Unlike the monochromatic sources, the orbital radius shrinks with time and the orbital frequency increases accordingly because of the GW radiation loss. In this case, parameter estimation accuracy depends on the functional form of noise spectral density $S_n(f)$. As a signal model of a binary coalesce, we adopt the restricted post-Newtonian waveform with the 1.5 PN phase in which the amplitude is retained up to the Newtonian order:

$$\tilde{h}_{Xi}(f) = \mathcal{A} Q_{Xi}(t_*)\, f^{-7/6} e^{-i\left[\varphi_{\mathrm{pol},Xi}(t_*) + \varphi_{\mathrm{Dop},X}(t_*)\right]} e^{i\Psi(f)}, \tag{3.8a}$$

[2] The value 3×10^{13} m^2 corresponds to the area formed by the TAMA-LIGO-Virgo network.

$$\mathcal{A} \equiv \sqrt{\frac{5}{24}} \frac{1}{\pi^{2/3}} \frac{c}{d} \left(\frac{GM_c}{c^3}\right)^{5/6}, \tag{3.8b}$$

$$\Psi(f) = 2\pi f t_c - \frac{\pi}{4} - \phi_c - \tilde{\Phi}(f), \tag{3.8c}$$

$$\tilde{\Phi}(f) = -\frac{3}{4}\left(\frac{GM_c}{c^3} 8\pi f\right)^{-5/3} \left[1 + \frac{20}{9}\left(\frac{743}{336} + \frac{11}{4}\eta\right) x - 16\pi x^{3/2}\right], \tag{3.8d}$$

$$t_*(f) = t_c - 5\left(\frac{GM_c}{c^3}\right)^{-5/3} (8\pi f)^{-8/3} \left[1 + \frac{4}{3}\left(\frac{743}{336} + \frac{11}{4}\eta\right) x - \frac{32}{5}\pi x^{3/2}\right], \tag{3.8e}$$

where t_c and ϕ_c are the time and the phase at the coalescence, respectively (see e.g. [55]). The mass $M_c \equiv (m_1 m_2)^{3/5} (m_1 + m_2)^{-1/5}$ and the mass ratio $\eta \equiv m_1 m_2 / (m_1 + m_2)^2$ are called a chirp mass and a symmetric mass ratio, respectively, and a post-Newtonian variable $x \equiv [\pi G (m_1 + m_2) f / c^3]^{2/3}$ was introduced. We cut-off the GW signal at $f_{\rm ISCO} \equiv c^3 / \left[6\sqrt{6}\pi G (m_1 + m_2)\right]$ beyond which the quasi-circular orbit is not stable any longer and the two point masses plunge toward each other. So, we set $\tilde{h}(f) = 0$ for $f > f_{\rm ISCO}$ in Eq. (3.8a).

We analyze parameter estimation accuracy for GWs from $10^4 M_\odot$ equal-mass IMBH binaries located at a distance of 200 Mpc. The GW signal described by Eqs. (3.8a)–(3.8e) consists of the eight waveform parameters $\{\mathcal{A}, t_c, \phi_c, \alpha, \delta, \psi, \cos\iota, M_c\}$. Substitution of Eq. (3.8a) into Eq. (D.5) yields the values of Fisher matrix elements. From Eq. (D.4), we get the accuracy of the waveform parameters. Here, we neglect the effect of the expansion of the Universe and the higher order terms in the Post-Newtonian expansion. However, the angular resolution $\Delta\Omega$ we calculate in this section is expected to be accurate because the angular resolution is accumulated at the inspiral phase long before the final plunge.

Performing 1,000 Monte-Carlo simulations, we obtain Fig. 3.5 that represents the probability distributions in a single-detector case for (a) SNR, (b) angular resolution, (c) measurement error of overall amplitude, and (d) measurement error of chirp mass[3]. The panel (a) of Fig. 3.5 shows that SNRs of the multi-output configuration are better by a factor of about 1.2 than the single-output case. This factor can be simply explained by $\sqrt{1^2 + (1/2)^2 + (1/2)^2} \simeq 1.2$ from Eqs. (C.10a)−(C.10c). The panel (b) indicates that the angular resolution in the multi-output configuration are improved by an order of magnitude. This feature can be traced to the polarization phase $\varphi_{{\rm pol},Xi}$. Since GWs from coalescing IMBH binaries are regarded as short-duration signals, the sky positions are well determined by the multi-output TOBA compared with the single-output TOBA in a similar discussion to the previous section. Accuracies of the other waveform parameters, especially $\mathcal{A}$, are also improved as shown in the panels (c) and (d) of Fig. 3.5 because the over-all amplitude $\mathcal{A}$ is strongly correlated with the GW polarizations through the antenna pattern functions $F_{+,\times}$.

[3] In the case of low SNRs, the estimation accuracies would be overestimated [74].

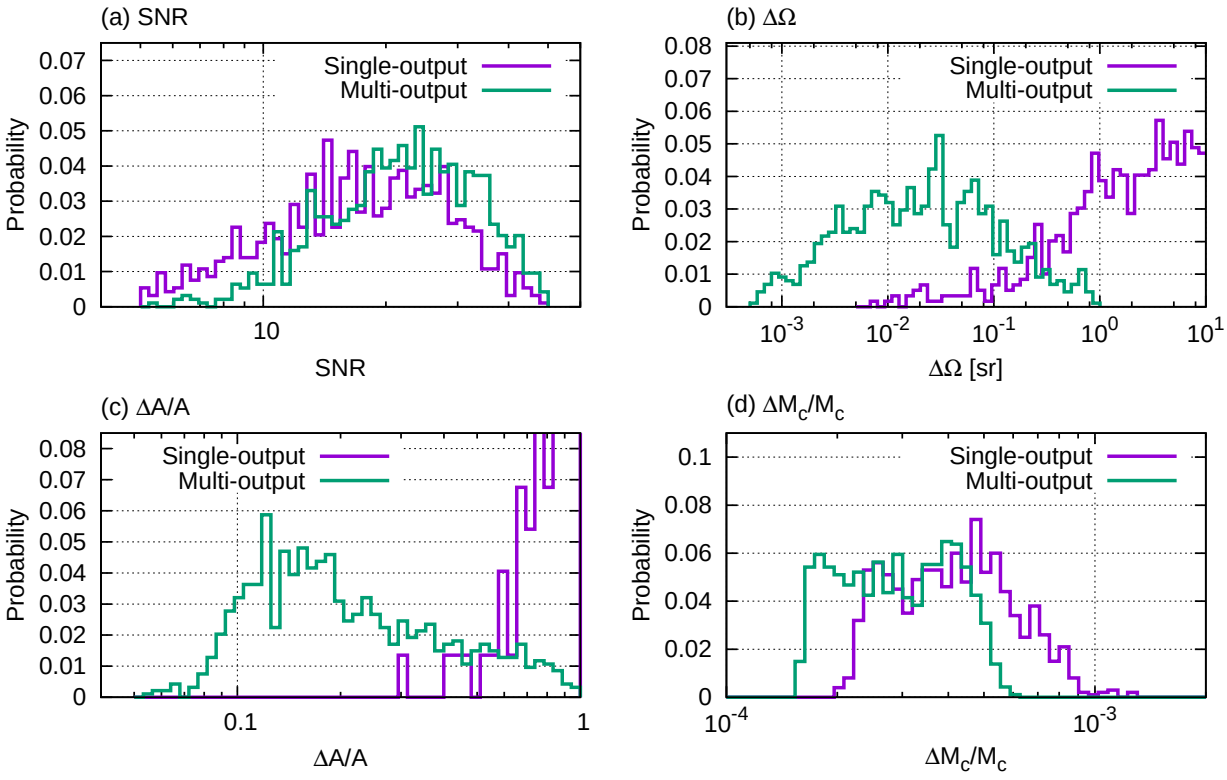

Figure 3.5: Histograms for (a) SNR, (b) angular resolution, (c) measurement error of overall amplitude, and (d) measurement error of chirp mass in the case of a single-detector for one-year observations. GWs are assumed to be emitted from $10^4 M_\odot$ equal-mass IMBH binaries located at a distance of 200 Mpc. We assume that sky locations and inclination angles are distributed uniformly. Polarization phases are arbitrarily set to be 0.5 radians. The two lines correspond to the single-output and multi-output TOBA, respectively.

3.1.4 Summary

In this section, we studied the performance of the proposed multi-output TOBA and presented the parameter estimation accuracy for the two nominal sources, monochromatic sources and binary coalescences. For long-duration signals, the multi-output TOBA can be treated as the same way as the conventional single-output TOBA apart from the improved SNR, as expected. The advantage of the multi-output system is merely the accumulation of the SNR. On the other hand, in the case of short-duration signals, the multi-output TOBA improves the parameter estimation accuracy drastically compared with the single-output TOBA because it can break the degeneracy of two polarization modes of GW signals even in the case of a single detector.

3.2 Low-frequency CW search with a TOBA

To date, data from the initial LIGO and Virgo science runs have been used to place upper limits on GW amplitudes from unknown isolated pulsars with GW frequencies above 20 Hz [84, 49, 85, 109, 110, 111, 112, 113, 114, 115, 116]. On the other hand, continuous GWs below 20 Hz have yet to be investigated because seismic noise on the Earth hinders the sensitivity of detectors to GWs in such a low-frequency regime. The ATNF catalogue shown in Fig. 2.1 lists about 1,500 pulsars in the frequency range from 1 Hz to 10 Hz, whereas it contains only about 400 above 10 Hz [15]. Hence, it is interesting to explore the low-frequency regime, although the expected GW amplitude scales as frequency squared. In this section, we first search for unknown continuous GWs coherently in the low-frequency regime using data from the Phase-II TOBA and report its results[4].

3.2.1 Phase-II TOBA

Previously, the Phase-I TOBA has been constructed, which is composed of a single 20 cm test mass and has succeeded in putting constraints on the abundance of stochastic GWs [100, 101, 102]. Motivated by the work discussed in the previous section [17], the Phase-II TOBA that is a prototype of the multi-output TOBA was developed [103, 104]. The main features of the Phase-II TOBA are common-mode noise rejection, the multi-output system, and the active and passive vibration systems. As can be seen in Fig. 3.7, the Phase-II TOBA has two 24 cm bar-shaped test masses each of which is suspended by two parallel tungsten wires near its center. In order to reduce the common-mode noise effectively, the two test masses are installed in such a way that their centers of mass are

[4] Recently, upper limits on stochastic GW background was set in the frequency band of $1-5$ Hz using the Phase-II TOBA data [117]. The most stringent upper limit is $\Omega_{\rm gw}h_{100}^2 \leq 6.0\times10^{18}$ at 2.58 Hz from a frequentist viewpoint, where h_{100} denotes the Hubble constant in units of 100 km/s/Mpc.

positioned at the same point on the horizontal plane. The motions of the bars in both the horizontal and vertical planes are monitored by using fiber Michelson laser interferometers, so that three independent output signals can be obtained unlike the previous prototype TOBA. A hexapod-type active vibration isolation system is incorporated into the Phase-II TOBA to reduce seismic noise at around 1 Hz; see [103, 104] for more details.

The Phase-II TOBA is placed in Tokyo (35°42′49.0″N, 139°45′47.0″E) and operated for 22.5 hours from 6:18 UTC, December 11, 2014 to 4:48 UTC, December 12, 2014. The measured strain sensitivity of the Phase-II TOBA is shown in Fig. 3.6 in which the red, blue, and, green lines correspond to the output signals from the xy, xz, and yz degrees of freedom, respectively. The z axis is in the local vertical direction, whereas the x and y axes align with the two bars when they are at rest (see also Fig. 3.2). The GW equivalent-strain sensitivity is about 10^{-10} $\mathrm{Hz}^{-1/2}$ at around 1 Hz for the signal on the horizontal plane. The sensitivity is limited by the seismic noise below 2 Hz and by unexpected noise in the optical fiber above 2 Hz. The peaks appearing at around 0.7 Hz, 5.7 Hz, 8.5 Hz, and 14 Hz correspond to the resonance of the optical bench, and the resonance of the vibration isolation table in the directions of y, x, and z axes, respectively. It should be noted that we do not incorporate the data obtained from monitoring the vertical planes into our following analysis because their sensitivities are unfortunately much worse than the sensitivity from the horizontal plane, as is evident from Fig. 3.6.

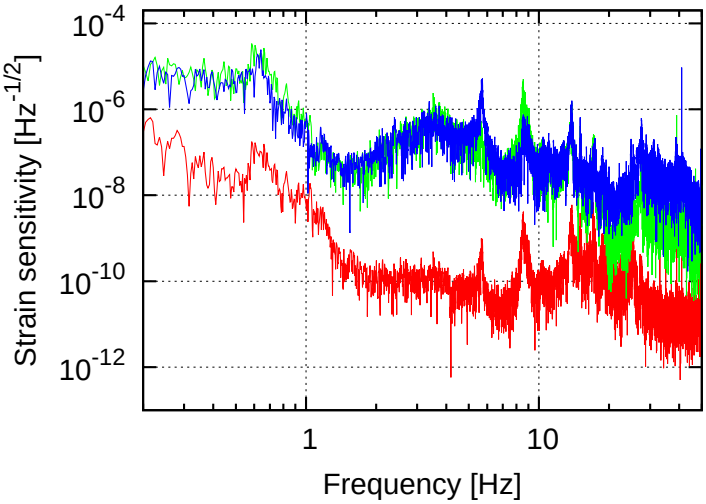

Figure 3.6: The strain sensitivity curve of the Phase-II TOBA. The horizontal axis shows the frequency and the vertical axis shows the square root of the one-sided noise spectral density $\sqrt{S_n(f)}$. The red, blue, and green lines correspond to the output signals from the xy, xz, and yz degrees of freedom, respectively.

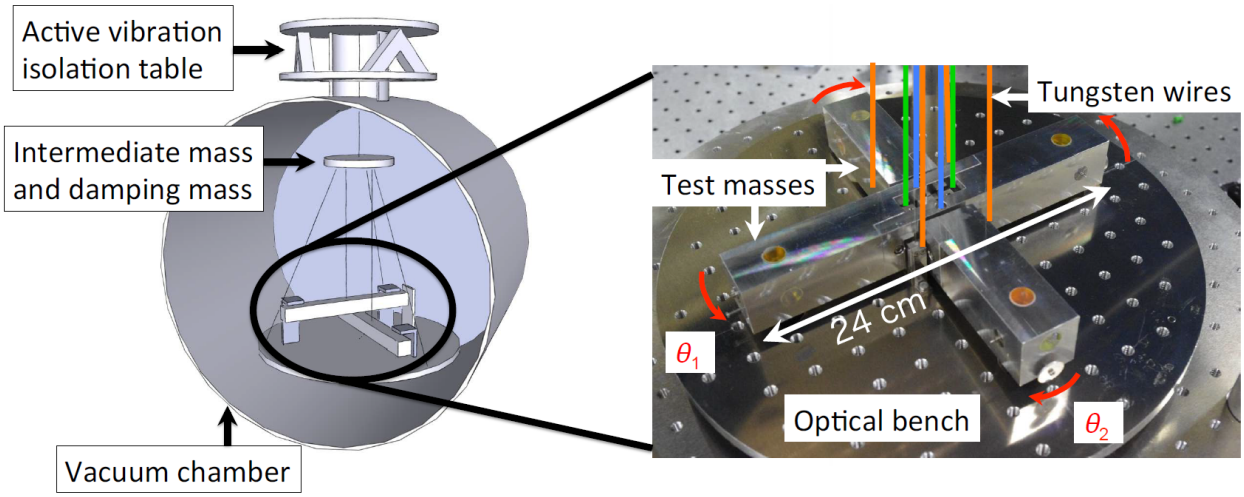

Figure 3.7: Photograph of the Phase-II TOBA [Credit: Yuya Kuwahara]. Each bar-shaped test mass has a mass of 0.61 kg and a length of 24.0 cm. The two bars are suspended by four tungsten wires with a length of 40.0 cm. The distance between the suspension points is 1.7 cm. Optical sensors are installed on an optical bench. GW signals are read out by measuring the relative motion between the test masses and the optical bench.

3.2.2 Statistical properties of the data

SFT

Since CW signals are long-duration signals, the length of analyzed data is typically more than of the order of a day. In the frequency domain analysis, such a long duration signal poses some problems such as non-stationarities of noise background and frequency shifts caused by the Doppler effects due to the Earth rotation and its orbital motion. In order to handle these problems, short-time-baseline Fourier transform (SFT) is carried out in CW analysis. SFT is a kind of Fourier transform usually used to deal with quasi-periodic signals whose frequencies gradually vary with time[5]. In this process, time series data are broken up into shorter time segments, which are often called SFT frames, by using window function, and then each frame is Fourier transformed.

There are three constraints on the time baseline of SFTs, T_{SFT}. The first is non-stationarities of detector noise. To estimate the noise background accurately, the time baseline of the SFTs should be short enough for the noise to be regarded as locally stationary during the time baseline. The second is frequency shifts of putative signals induced by NS's spin-down and relative motion of the detector with respect to the NS. The third is computational resources. The computational cost of performing a search linearly increases with the number of SFT segments. Since the first and second requirements oppose to the third, we have to chose a compromise between these needs. In practice,

[5] In the field of signal processing, this process is often referred to as short-time Fourier transform (STFT).

T_{SFT} is chosen such that the signal frequency does not shift by more than half a frequency bin during T_{SFT},

$$T_{\mathrm{SFT}} < \sqrt{\frac{1}{2|\dot{f}|}}. \tag{3.9}$$

The signal frequency $f(t)$ is modulated by the Doppler effect due to the relative motion of the detector with respect to the NS as in Eq. (2.22a). So, the time derivative of the observed frequency is estimated as

$$\dot{f}(t) \simeq f_0 \frac{\hat{\boldsymbol{n}}}{c} \cdot \frac{d\boldsymbol{v}}{dt} \leq \frac{f_0}{c} \left| \frac{d\boldsymbol{v}}{dt} \right| \simeq \frac{f_0}{c} \frac{v_{\mathrm{E}}^2}{R_{\mathrm{E}}}, \tag{3.10}$$

where f_0 is the intrinsic spin frequency of the NS, v_{E} is the spin velocity of the Earth, and R_{E} the Earth radius. Equations (3.9) and (3.10) lead to the restriction on the time baseline T_{SFT} of the SFTs,

$$T_{\mathrm{SFT}} < \sqrt{\frac{1}{2} \frac{cR_{\mathrm{E}}}{f_0 v_{\mathrm{E}}^2}} \simeq 9.4 \times 10^3 \text{ sec} \left(\frac{50 \text{ Hz}}{f_0} \right)^{1/2}. \tag{3.11}$$

Therefore, we set the time baseline T_{SFT} to be 9,000 seconds in this seciton[6]. It should be noted that the SFT baseline length can be taken longer at lower frequencies as long as the data stationarity is assured.

Statistical properties of the data

We investigated the statistical properties of our data in the band 6–7 Hz using the SFTs at around which the TOBA has the best sensitivity. It is convenient to define the following quantity to evaluate to what extent the noise obeys a Gaussian distribution [62]:

$$P_{\alpha,k} \equiv \frac{|\tilde{x}_{\alpha,k}|^2}{\frac{1}{N_{\mathrm{band}}} \sum_{k'=0}^{N_{\mathrm{band}}} |\tilde{x}_{\alpha,k'}|^2}, \tag{3.12}$$

where the indices α and k stand for the k-th frequency bin in the α-th SFT segment. $P_{\alpha,k}$ can be regarded as the normalized noise power in the frequency bin k. Because $|\tilde{x}_{\alpha,k}|^2$ follows a χ^2 distribution with two degrees of freedom in the absence of GW signal in data, the numerator and denominator in Eq. (3.12) follow χ^2 distributions with 2 and $2N_{\mathrm{band}}$ degrees of freedom, respectively. Thus, $P_{\alpha,k}$ obeys a F-distribution, $P_{\alpha,k} \sim F(2, 2N_{\mathrm{band}})$[7].

[6] The time baseline T_{SFT} is typically set to be 1,800 seconds in the conventional targeted CW search by LIGO/VIRGO.

[7] In general, a statistic following F-distribution with parameters d_1 and d_2 is defined as a ratio of

The PDF and CDF are expressed as

$$f\left(x; d_1, d_2\right) = \frac{1}{B\left(d_1/2, d_2/2\right)} \left(\frac{d_1}{d_2}\right)^{\frac{d_1}{2}} x^{\frac{d_1}{2}-1} \left(1 + \frac{d_1}{d_2} x\right)^{-\frac{d_1+d_2}{2}}, \tag{3.14a}$$

$$F\left(x; d_1, d_2\right) = I\left(\frac{d_1 x}{d_2 + d_1 x}; \frac{d_1}{2}, \frac{d_2}{2}\right), \tag{3.14b}$$

where $B\left(a, b\right)$ and $I\left(x; a, b\right)$ denote the beta function and the regularized incomplete beta function[8]. For $N_{\mathrm{band}} \gg 1$, $P_{\alpha,k}$ is approximately distributed according to Gaussian distribution with unit mean and variance.

The histogram of $P_{\alpha,k}$ is shown in the left panel of Fig. 3.8. If the data is distributed according to a Gaussian distribution, $P_{\alpha,k}$ is approximately proportional to an exponential, or in other words, $P_{\alpha,k}$ is aligned with a straight line in a semi-log plot. The measured values of the mean and the standard deviation are 1.00 and 1.08, respectively. Thus, we can regard that our data follows almost a Gaussian distribution. We also have studied the stationarity of the data by computing the difference between adjacent phases of the SFT data [62],

$$\Delta\Phi_{\alpha,k} = \Phi_{\alpha,k} - \Phi_{\alpha,k-1}. \tag{3.16}$$

If the data is stationary, $\Delta\Phi_{\alpha,k}$ obeys a unifom distribution in the range of $[-\pi, \pi]$. The histogram of measured $\Delta\Phi_{\alpha,k}$ is shown in the right panel of Fig. 3.8 in which no strong non-stationarity is found.

3.2.3 Data analysis

GW signal

We will start with briefly summarizing data analysis method we will use in this section based on Chapter 3. A pulsar is a rapidly rotating NS whose spin frequency is nearly constant, say f_0. GWs from such a source are generated by a non-axisymmetry of the

variances of χ^2 distribution with d_1 and d_2 degrees of freedom,

$$F_{d_1,d_2} = \frac{\chi^2_{d_1}/d_1}{\chi^2_{d_2}/d_2}. \tag{3.13}$$

[8] These functions are defined as

$$B\left(a, b\right) = \frac{\Gamma\left(a\right)\Gamma\left(b\right)}{\Gamma\left(a+b\right)}, \quad I\left(x; a, b\right) = \frac{B\left(x; a, b\right)}{B\left(a, b\right)}, \tag{3.15a}$$

$$B\left(x; a, b\right) = \int_0^x t^{a-1}\left(1-t\right)^{b-1} dt, \tag{3.15b}$$

where a and b are assumed to be integers.

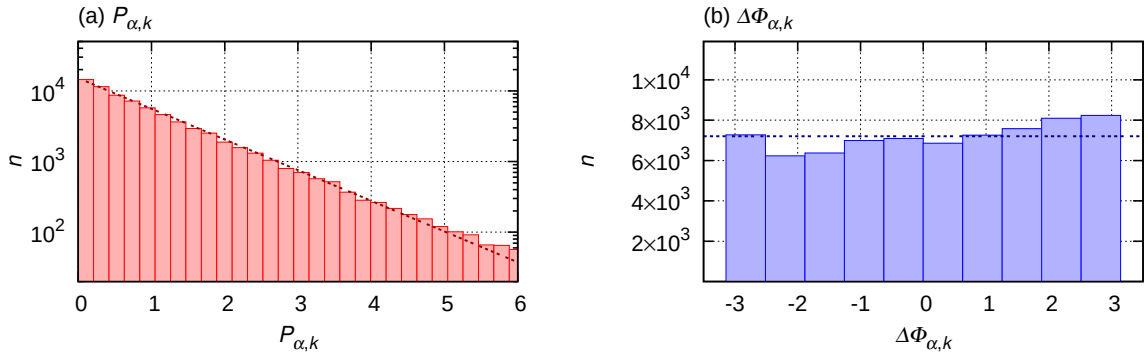

Figure 3.8: Histogram of (a) the power $P_{\alpha,k}$ and (b) the phase $\Delta\Phi_{\alpha,k}$ of the TOBA SFT data at the k-th frequency bin. If the data is distributed according to a Gaussian distribution, $P_{\alpha,k}$ lies on the straight line described by a dotted line. If the data is stationary, $\Delta\Phi_{\alpha,k}$ is distributed uniformly in the range of $[-\pi, \pi]$ as described by a dotted line.

pulsar around its spin axis. The GW amplitude is expressed by

$$h_0 = \frac{16\pi^2 G}{c^4 d}\varepsilon I f_0^2, \tag{3.17}$$

where G, c, and I are Newton's gravitational constant, the speed of light, and the NS's moment of inertia, respectively. The non-axisymmetry is characterized by the parameter ε called ellipticity. The GW singal we expect to detect from a rapidly rotating NS is described as

$$h(t) = h_+(t) F_+(t) + h_\times(t) F_\times(t), \tag{3.18a}$$

$$h_+(t) = h_0 \frac{1+\cos^2\iota}{2}\cos\Phi(t), \tag{3.18b}$$

$$h_\times(t) = h_0 \cos\iota \sin\Phi(t), \tag{3.18c}$$

where h_0 is the overall amplitude, $\Phi(t)$ is the GW phase measured at the solar system barycenter (SSB), and ι is the inclination, which is the angle between the line of sight and the spin axis. The antenna pattern functions $F_{+,\times}$ represent the response of the antenna to the plus and cross polarization modes of the incoming GWs. The antenna patterns of the TOBA are given by Eqs. (C.12a) and (C.12b) in Appendix C[9]. The spin of the Earth around its axis gives rise to the amplitude modulation that is described by the time dependence of $F_{+,\times}$.

The Earth's spin around its axis and the its rotation around the Sun bring Doppler

[9] The antenna patterns of the TOBA rotated by 45° on the detector plane are identical to that of a 90° interferometer.

modulation to the GW phase up to the first derivative of frequency as follows:

$$\Phi(t) = \phi_0 + 2\pi\Delta t\hat{f}(\Delta t), \tag{3.19a}$$

$$\hat{f}(\Delta t) = f_0 + \frac{1}{2}\dot{f}\Delta t, \tag{3.19b}$$

$$\Delta t = \tau + \frac{\boldsymbol{r}\cdot\hat{\boldsymbol{n}}}{c} + \Delta_{\rm rel} - t_0, \tag{3.19c}$$

where ϕ_0, τ, $\boldsymbol{r}$, and $\hat{\boldsymbol{n}}$ denote the initial phase at the reference time t_0, the arrival time of the GW measured at the detector, the detector position on the Earth with respect to the SSB, and the unit vector pointing toward the NS from the SSB. The unit vector $\boldsymbol{n}$ is related to the equatorial coordinates of the source, right ascension α and declination δ. The timing correction $\Delta_{\rm rel}$ represents relativistic effects such as the Einstein delay and the Shapiro delay.

$\mathcal{F}$-statistic

We use a detection statistic called the $\mathcal{F}$-statistic to discriminate whether or not an expected GW signal exists in the data [57]. The $\mathcal{F}$-statistic is derived from the method of maximum likelihood function and is known as the most powerful test from a frequentist standpoint according to the Neyman−Pearson lemma [72]. On the stationary Gaussian noise assumption, the log-likelihood function is expressed as

$$\ln\Lambda = (x|h) - \frac{1}{2}(h|h), \tag{3.20}$$

where $(\cdot|\cdot)$ denotes the noise-weighted inner product defined as

$$(x|y) = 4\mathrm{Re}\int_0^\infty \frac{\tilde{x}(f)\,\tilde{y}^*(f)}{S_n(f)}df. \tag{3.21}$$

The maximization of $\ln\Lambda$ over the amplitude parameters $\mathcal{A}$ defined by Eqs. (2.24a)–(2.24d) leads to the $\mathcal{F}$-statistic,

$$2\mathcal{F} = \max_{\mathcal{A}}[2\ln\Lambda]. \tag{3.22}$$

The number of search parameters is reduced from eight to four in this process. In the presence of a GW signal, $2\mathcal{F}$ obeys a non-central χ^2 distribution with four degrees of freedom and a non-centrality parameter ρ^2, where ρ is the average SNR in the case of a signal perfectly matched with the template. In the absence of any GW signal, $2\mathcal{F}$ obeys the χ^2 distribution function with four degrees of freedom. The SNR of the signal is related to the expected value of the $\mathcal{F}$-statistic by $\langle 2\mathcal{F}\rangle = 4 + \rho^2$.

The threshold for $\mathcal{F}$-statistic can be related to a false alarm probability $p_{\rm FA}$ as discussed

in Sec. 2.4.1. When data is consistent with Gaussian noise, the probability that a single value of $2\mathcal{F}$ falls below $2\mathcal{F}_{\rm thr}$ is written by Eqs. (2.50a) and (3.28). Assuming values of $2\mathcal{F}$ for $N_{\rm temp}$ templates are independent of each other, the false alarm probability, which is the probability that one or more $2\mathcal{F}$ take values above $2\mathcal{F}_{\rm thr}$, is written as

$$p_{\rm FA} = 1 - \left[\int_0^{2\mathcal{F}_{\rm thr}} p\left(2\mathcal{F}|\rho^2 = 0\right) d\left(2\mathcal{F}\right)\right]^{N_{\rm temp}}, \tag{3.23}$$

where $N_{\rm temp}$ denotes the number of templates. In our case, $N_{\rm temp}$ is estimated to be 3.2×10^{10} as will be discussed. Setting $p_{\rm FA} = 0.01$, we obtain the threshold of $\mathcal{F}$-statistic as $2\mathcal{F}_{\rm thr} = 64.6$ by solving Eq. (3.23) inversely.

If the measured value of the $\mathcal{F}$-statistic is below the predetermined threshold, we move on to the step of placing a constraint on the GW amplitude h_0. An upper limit of the amplitude can be defined as a function of the confidence level C, $h_0\left(C\right)$. The inverse of $h_0\left(C\right)$ is written as

$$C\left(h_0\right) = \int_{2\mathcal{F}_{\rm obs}}^{\infty} p\left(2\mathcal{F}|h_0\right) d\left(2\mathcal{F}\right), \tag{3.24}$$

where $\mathcal{F}_{\rm obs}$ denotes the observed value of the $\mathcal{F}$-statistic and $p\left(2\mathcal{F}|h_0\right)$ denotes the probability distribution function of $2\mathcal{F}$ in the presence of a signal with its amplitude h_0. The value of the upper limit is evaluated by solving Eq. (3.24) via Monte-Carlo simulations over the unknown parameters $\{h_0, \cos\iota, \psi\}$.

The value of h_0 which satisfies Eq. (3.24) can be numerically evaluated by the Newton-Raphson method. Let $J\left(h_0\right)$ be a false-dismissal rate averaged over angular parameters $\alpha, \delta, \cos\iota$, and ψ[10]. The angular parameters are assumed to be distributed uniformly in the range of $\alpha \in [0, 2\pi]\,, \delta \in [0, \pi]\,, \cos\iota \in [-1, 1]$, and $\psi \in [0, 2\pi]$, respectively. Note that the initial phase ϕ_0 is not averaged over because the value of the $\mathcal{F}$-statistic is independent of ϕ_0 as shown in Eq. (2.46). For given a value of $P_{\rm FD}$,

$$J\left(h_0^C\right) = P_{\rm FD}. \tag{3.25}$$

Taylor expansion of $J\left(h_0^C\right)$ around h_0 leads to the correction term of the Newton-Raphson method,

$$\begin{aligned} &J\left(h_0^C\right) = J\left(h_0\right) + \left(h_0 - h_0^C\right) J'\left(h_0\right) + \mathcal{O}\left[\left(\Delta h_0\right)^3\right], \\ &\Rightarrow\ \Delta h_0 \equiv h_0 - h_0^C \simeq \frac{J\left(h^C\right) - J\left(h_0\right)}{J'\left(h_0\right)} = \frac{P_{\rm FD} - J\left(h_0\right)}{J'\left(h_0\right)}. \end{aligned} \tag{3.26}$$

[10] In a targeted search, sky positions (α, δ) of NSs are already known by EM observations. So, these two parameters are not averaged over. To put it another way, α and δ in Eqs. (3.29a) and (3.29b) are fixed whereas $\cos\iota$ and ψ are treated as random variables.

The next iteration value of h_0 can be obtained by adding the above step to the previous iteration value as

$$h_0^{(n+1)} = h_0^{(n)} + \Delta h_0^{(n)}, \quad \Delta h_0^{(n)} \equiv \frac{P_{\rm FD} - J\left(h_0^{(n)}\right)}{J'\left(h_0^{(n)}\right)}. \tag{3.27a}$$

The function $J\left(h_0\right)$ can be evaluated by Monte-Carlo simulations over angular parameters as referred to above. Also, $\mathcal{F}$ is averaged over in the range of $\mathcal{F} \in [0, \mathcal{F}_{\rm obs}]$. When detector noise is stationary and Gaussian, the PDF $p\left(2\mathcal{F}|h_0\right)$ obeys non-central χ^2 distribution function with four degrees of freedom and a non-centrality parameter ρ^2,

$$p\left(2\mathcal{F}|h_0\right) = f_X\left(2\mathcal{F}; 4, \rho^2\right). \tag{3.28}$$

Combining Eqs. (2.53) and (3.28), the functions $J\left(h_0\right)$ and $J'\left(h_0\right)$ appearing in Eq. (3.27a) can be approximately evaluated as

$$J\left(h_0\right) = \frac{2\mathcal{F}_{\rm obs}}{N_{\rm MC}} \sum_{i=1}^{N_{\rm MC}} f_X\left(2\mathcal{F}_i; 4, \rho^2\left(\alpha_i, \delta_i, \cos\iota_i, \psi_i\right)\right), \tag{3.29a}$$

$$J'\left(h_0\right) = \frac{2\rho^2}{h_0} \frac{2\mathcal{F}_{\rm obs}}{N_{\rm MC}} \sum_{i=1}^{N_{\rm MC}} \frac{f_X\left(2\mathcal{F}_i; 4, \lambda\right)}{d\lambda}\Big|_{\lambda=\rho^2(\alpha_i,\delta_i,\cos\iota_i,\psi_i)}, \tag{3.29b}$$

where $N_{\rm MC}$ denotes the number of trials in the Monte-Carlo simulations[11]. In our analysis, $N_{\rm MC}$ is set to be 10^6. Concrete expressions for $f_X\left(x; 4, \lambda\right)$[12] and its derivative with respect to the non-centrality parameter are

$$f_X\left(x; 4, \lambda\right) = \frac{1}{2} e^{-\frac{1}{2}(\lambda+x)} \sqrt{\frac{x}{\lambda}} I_1\left(z\right), \tag{3.31a}$$

$$\frac{df_X\left(x; 4, \lambda\right)}{d\lambda} = \frac{1}{4} e^{-\frac{1}{2}(\lambda+x)} \left[\frac{1}{2}\frac{x}{\lambda}\left(I_0\left(z\right) + I_2\left(z\right)\right) - \sqrt{\frac{x}{\lambda}}\left(1 + \frac{1}{\lambda}\right) I_1\left(z\right)\right], \tag{3.31b}$$

$$I_n\left(z\right) \equiv \frac{1}{\pi} \int_0^\pi e^{z\cos\theta} \cos\left(n\theta\right) d\theta, \tag{3.31c}$$

where $z \equiv \sqrt{x\lambda}$ and $I_n\left(z\right)$ denotes the modified Bessel function of the first kind.

[11] $d\lambda/dh_0 = 2\rho^2/h_0$ is satisfied by proportional relation between the non-centrality parameter and the GW amplitude, $\lambda = \rho^2 \propto h_0^2$.

[12] In general, a non-central χ^2 distribution with k degrees of freedom and a non-centrality parameter λ is expressed by

$$f_X\left(x; k, \lambda\right) = \frac{1}{2} e^{-\frac{1}{2}(\lambda+x)} \left(\frac{x}{\lambda}\right)^{\frac{k}{4}-\frac{1}{2}} I_{\frac{k}{2}-1}\left(z\right). \tag{3.30}$$

Analysis and results

Equations (3.17)–(3.19c) indicate that a continuous GW is characterized by eight parameters when we take into account up to the first derivative of frequency. The four amplitude parameters are projected out by using the $\mathcal{F}$-statistic. Then, the parameters to be searched over become only the phase parameters $\{\alpha, \delta, f_0, \dot{f}\}$. The spacing of frequency bins for the templates is chosen by the inverse of twice the observation time. The grid spacings on the sky positions are chosen such that the maximum mismatch is less than 0.02. We take both $\Delta\alpha$ and $\Delta\delta$ to be 0.01 radians conservatively. To reduce the computational burden, we did not search over spin-down parameters. So our analysis is valid only for NSs with a spin-down $\dot{f}$ less than $1/(2T_{\rm obs}^2) \simeq 7.62 \times 10^{-11}$ Hz s^{-1} where $T_{\rm obs} = 22.5$ hours is the data length. Thus, the number of spin-templates and sky-templates are estimated to be $N_{\rm spin} \simeq 2T_{\rm obs} \simeq 1.62 \times 10^5$ and $N_{\rm sky} \simeq 2\pi^2/\left(0.01\right)^2 \simeq 1.92 \times 10^5$, respectively. The total number of templates are $N_{\rm temp} = N_{\rm spin} N_{\rm sky} \simeq 3.2 \times 10^{10}$.

We make SFTs of the 22.5 hours contiguous data by employing MakeSFTs code in the LIGO scientific collaboration Algorithm Library (LAL) [118]. Each segment is windowed by a Tukey window function[13] prior to computing the SFTs. The length of each SFT segment is chosen as 9,000 seconds for the reasons described in Sec. 3.2.2. The frequency range to be searched is a 1 Hz band in 6–7 Hz where our detector has the best sensitivity. The statistical properties of the data in this band are described in Sec. 3.2.2.

We compute $2\mathcal{F}$ by making use of ComputeFstatistic_v2 code in the LAL [119]. The left panel in Fig. 3.9 shows the distribution of $2\mathcal{F}$ over a 0.01 Hz band between 6.10 Hz and 6.11 Hz. The experimentally measured distribution of the $\mathcal{F}$-statistic is represented by the filled boxes. The theoretically expected distribution in the case of the Gaussian noise without any GW signal is represented by a χ^2 distribution with four degrees of freedom, which are shown by the dotted line. As can be seen in the left panel of Fig. 3.9, the two agree very well. This indicates that the data we observed is filled with almost Gaussian noise. The right panel is identical to the left panel but changes the scale of the vertical axis to a the semi-log scale. Because of the small non-Gaussian noise, the filled area deviates slightly from the dotted line for larger values of the $\mathcal{F}$-statistic.

We divide the 1 Hz band between 6 Hz and 7 Hz into 100 sub-bands each of length 0.01Hz. The loudest values of $2\mathcal{F}$ in each sub-band resulting from the all-sky search are

[13] The Tukey window function is defined as

$$w\left(x\right) = \begin{cases} \frac{1}{2}\left[1 + \cos\left(\frac{2\pi}{r}\left(x - \frac{r}{2}\right)\right)\right], & 0 \leq x < \frac{r}{2} \\ 1, & \frac{r}{2} \leq x < 1 - \frac{r}{2} \\ \frac{1}{2}\left[1 + \cos\left(\frac{2\pi}{r}\left(x - 1 + \frac{r}{2}\right)\right)\right], & 1 - \frac{r}{2} \leq x \leq 1 \end{cases} \tag{3.32}$$

where r is a parameter related to a length of the window.

computed and are shown in the left panel of Fig. 3.10. There is no significant candidate whose value of the $\mathcal{F}$-statistic is above the predetermined threshold $2\mathcal{F}_{\rm thr} = 64.6$ corresponding to $p_{\rm FA} = 0.01$. Then, we move on to the step of finding the upper limits on h_0 by employing Eq. (3.24). The right panel in Fig. 3.10 represents the upper limit of h_0 with a 95% confidence level in each sub-band. The obtained upper limits are of the order of 5×10^{-12}. This values are precisely consistent with theoretically expected upper limits calculated by Eq. (3.31) in [61]. In our case, $p_{\rm FA} = 0.01, p_{\rm FD} = 0.05, N_{\rm seg} = 1$, and $N_{\rm temp} \simeq 3.2 \times 10^{10}$. A statistical factor is estimated to be ~ 36.7, which implies $h_0 \sim 5.1 \times 10^{-12}$. The constraints on h_0 become tighter as the frequency increases. This feature basically reflects the noise curve shown in Fig. 3.6. The most stringent upper limit on h_0 is 3.6×10^{-12} at 6.84 Hz.

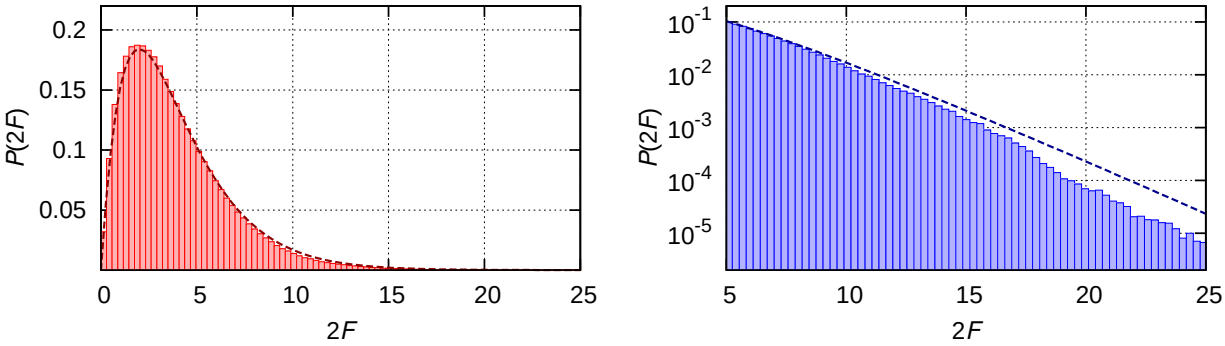

Figure 3.9: Probability distributions of the $\mathcal{F}$-statistic over $6.10 - 6.11$ Hz. The right panel is identical to left panel apart from the scale of the vertical axis and the range of the horizontal axis. The filled areas in both panels represent histograms obtained from the observations. In each panel, a dotted line represents a central χ^2 distribution with four degrees of freedom. When the data is dominated by a Gaussian noise, the histogram obeys the dotted line.

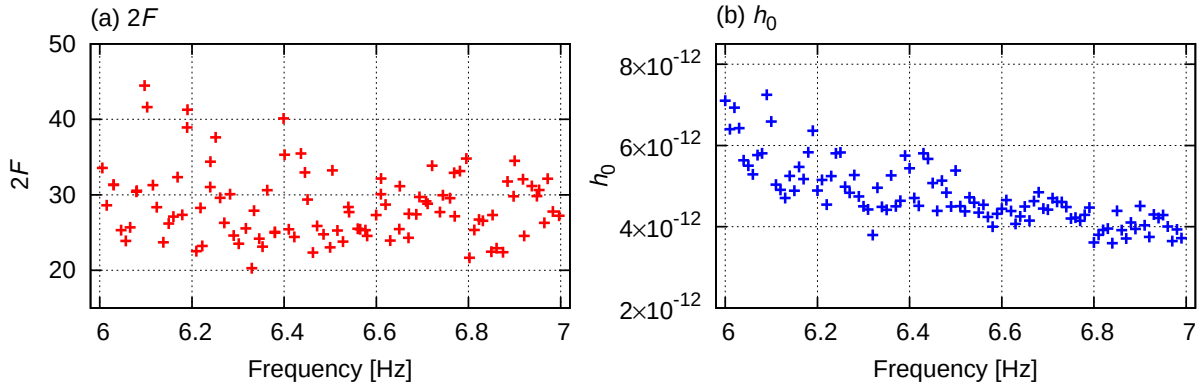

Figure 3.10: (a) Loudest values of $2\mathcal{F}$ in sub-bands of 0.01 Hz width. (b) Upper limits on h_0 with 95% confidence level in sub-bands as a function of frequency.

Discussion

We can interpret our upper limits on the strain amplitudes in terms of upper limits on the ellipticity ε using Eq. (3.17). For instance, when we consider a NS with a moment of inertia $I = 10^{38}$ kg m^2 at a distance of $d = 1$ kpc, the most stringent upper limit we obtained corresponds to the constraint on the ellipticity of $\varepsilon = 1.7 \times 10^{10}$. The maximum possible value of ellipticity is typically of the order of less than 10^{-6} [26], so this limit has yet to reach an interesting parameter region.

One of the proposed configurations of the TOBA [17] may achieve the best sensitivity of $\sim 10^{-20}$ Hz$^{-1/2}$ at around 0.1 Hz. With the proposed TOBA, we can detect GWs from inspiralling compact binaries such as NS/NS binaries within the Local Group or intermediate-mass black hole binaries within 10 Gpc, in addition to low-frequency continuous GWs from rapidly rotating compact stars. In fact, the $\mathcal{F}$-statistic search method we employed in this paper can be used for inspiralling compact binaries long before their coalescences [120, 121, 122, 123].

3.2.4 Summary

In this section, we carried out an all-sky search for continuous GWs from isolated spinning NSs in the frequency range from 6 Hz to 7 Hz using the $\mathcal{F}$-statistic method. The data was obtained from a 22.5-hour observation with the Phase-II TOBA at Tokyo in Japan and has good sensitivity at of the order of 1 Hz. We converted our data into 9,000-second SFT segments and searched coherently for an isolated NSs for all sky positions by the method of the $\mathcal{F}$-statistic. As a result, no significant candidates were found at 6–7 Hz and the most stringent upper limits on h_0 with 95 % confidence level in this band is 3.6×10^{-12} at 6.84 Hz.

Chapter 4

Targeted CW search with iKAGRA

KAmioka GRAvitational-wave telescope (KAGRA)[1][12, 124] is the first Japanese km-scale interferometric GW detector, which is often categorized into second-generation GW detectors as well as advanced LIGO and advanced Virgo. There exist two main unique features in KAGRA. One is underground operation. KAGRA is located about 200 meters underground below Ikenoyama mountain at Kamioka Mine in Gifu Prefecture, Japan (35°24′43″N, 137°18′21″E [125]). The underground observation is expected to reduce seismic noise, and thus provide quiet and stable environment for GW observations. The detector started to be constructed in 2010, which is now being upgrading toward observation with a full configuration within a few years. The other feature is cryogenic operation. Detector sensitivity around a few hundred Hz is hampered by thermal noise that excites vibrations in the mirrors and the suspension wires. In order to mitigate the thermal noise, the four mirror test masses that constitute the two Fabry-Perot cavities are cooled down to 20 K. Sapphire mirrors suspened by sapphire wires are used in KAGRA because of its high thermal conductivitity at low temperatures. It is expected that these new technology[2] will provide a useful knowledge for third-generation GW detectors such as the Einstein Telescope.

A roadmap for KAGRA is composed of two phases: the initial KAGRA (iKAGRA) and the baseline KAGRA (bKAGRA). In the iKAGRA phase, the configuration is a simple Michelson interferometer in a room-tempearature as will be discussed in the next section. From a standpoint of data analysis, the main purposes of iKAGRA are to validate the search pipeline we developed, to find program-related problems at the early stage, and to gain experiences to analyze actual data toward bKAGRA. In this chapter, we report the results of an end-to-end test for a targeted search for known isolated pulsars. Also, we summarize future prospects for CW search in the bKAGRA phase.

[1] The formal name is Large-scale Cryogenic Gravitational-wave Telescope (LCGT).

[2] The technology for underground and cryogenic operation has been tested by Cryogenic Laser Interferometer Observatory (CLIO) detector that is a prototype detector for KAGRA [126].

4.1 Detector

4.1.1 Detector configuration

The initial KAGRA, so-called iKAGRA, consists of a Michelson interferometric GW detector with its arm length of 3 km as shown in Fig. 4.1. The interferometer was constructed in underground at Kamioka Mine in Gifu Prefecture. The underground observation is expected to mitigate seismic noise and make it possible for the detector to operate in both quiet and stable environment. Figure 4.1 shows a simple schematic view of the iKAGRA configuration [127, 128]. The laser with 2 W power at a wavelength of 1064 nm is used as an input laser beam. The input laser beam passes through an input mode cleaner (IMC) composed of three mirrors (MCi, MCe, and MCo) in order to filter out higher-order spatial modes of the laser beam and stabilize laser light frequency. Power recycling (PR) mirrors are installed to broaden the input beam waist and adjust its direction. The input beam is split into two orthogonal beams by the central beam splitter (BS). After bouncing at the end mirrors (ETMX and ETMY), the two beams are recombined at the BS and return to the laser system. An input Faraday isolater (IFI) is placed between the IMC and the BS for optical isolation of the laser system from the interferometer. The IFI prevents the reflected light from returning into the laser cavity and change its direction. The recombined beam are detected at a photo-detector (PD) that is placed in the direction away from the laser system[3]. Temporal change of difference in the arm lengths due to the passage of a GW is read out at the PD by means of optical interference effects.

4.1.2 Observation

The iKAGRA operated for about three weeks between March and April in 2016. The observation run of the iKAGRA is divided into two phases, the first run in March and the second run in April. The first run took place during a week between March 25, 17:00 JST and March 31, 17:00 JST (from 1142928017 to 1143446417 in GPS time). After the commissioning in the first week of April, the second run was conducted between April 11, 9:00 JST and April 25, 17:00 JST (from 1144368017 to 1145606417 in GPS time).

Data obtained from interferometric GW detectors are generally stored in the form of a frame format that is available via the Frame Library Software [129] developed by LIGO and VIRGO collaborations. A frame is a standard format commonly used in GW community and records the following information: the GPS start time of the frame, the time length of the frame, a strain channel corresponding to the main data output $h(t)$, auxiliary channels that is obtained by monitoring the instruments and the ambient

[3] GW signals are usually read out from the PD placed at the anti-symmetric port. In the iKAGRA, the PD is placed at the symmetric port due to the small space in the anti-symmetric port.

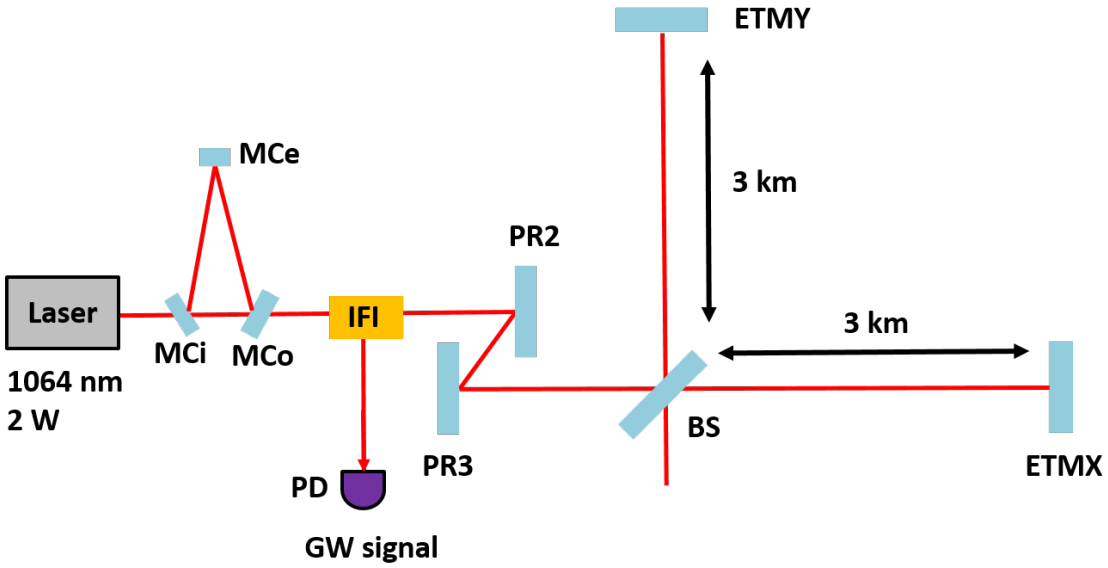

Figure 4.1: The schematic view of the iKAGRA configuration [127, 128]. The power of incident laser light is 2 W and its wavelength is 1064 nm. Passing the mode cleaner leads to fundamental spatial mode of the laser beam by filtering higher order spatial modes. The three mirrors, IMC, MCi, MCe, and MCo stand for input, end, and output mirrors, respectively. PR2 and PR3 mirrors are placed to adjust the beam waist.

environment around the interferometer, and so on. The iKAGRA data are stored in 32-sec frame files each of which is a 16,384 Hz time series. When analyzing for GW detections, we used post-processed data (proc data) that contains mainly a strain channel and data quality flags. The flags give us useful information on the detector state for GW data analysis. In the iKAGRA data, data quality is categorized into the following three types based on the auxiliary channels [130]:

Category A checks whether the interferometer is locked or not by using four auxiliary channels.

Category B is a lock flag obtained from the state machine automation platform *Guardian* [131].

Category C checks values of feedback signals.

Strain data are sampled at a rate of 16,384 Hz, whereas data quality flags consist of a 1 Hz time series.

Figure 4.4 (a) shows the number of frame files from the iKAGRA as a function of date. The red colored histogram represents the total number of the frame files in a day. Among them, available data for GW analysis whose flags indicate data as good states are represented by the blue colored histogram. The ratio of the good state data to the total data is shown in Fig. 4.4 (b). As can be seen in these figures, the observation run in

April is more stable than that in March. In fact, the Michelson interferometer in March lost lock about every 30 minutes because tidal forces induced by the Moon and the Sun exerted on the end mirrors. This caused the saturation of feedback signals in the actuation range. The total locked time and the longest locked time in the first run are 129.5 hours and 3.6 hours, respectively. Thanks to the updates during the commissioning, the total locked time and the longest locked time in the second run are 257.7 hours and 21.3 hours, respectively. The fraction of the available frame data on April 16 is only 30% and are very few compared with other days. This is because the main shock of the 2016 Kumamoto earthquakes occurred at 1:25 JST on April 16 in Kumamoto Prefecture.

The measured GW strain-equivalent noise level, or sensitivity is depicted in Fig. 4.3. The red and blue region describe the sensitivity estimated from data collected in March and April, respectively. The solid lines represent the median sensitivity during the observation. The shaded zones represent the sensitivities between the 5th and 95th percentile. Since the April run is stable, the red-shaded zone is almost invisible in this figure. Typically, the strain sensitivities in March and April at $f = 200$ Hz are $\sqrt{S_n(f)} \sim 2 \times 10^{-15}$ Hz$^{-1/2}$ and 2×10^{-16} Hz$^{-1/2}$, respectively. The sensitivity is limited by seismic noise below 4 Hz, ADC noise above 3 kHz, and acoustic noise at around 100 Hz. The summary table of the iKAGRA observation is found in Table 4.1.

	Observation period (GPS)	N_{frames}	N_{SFTs}	Best sensitivity (Hz$^{-1/2}$)
First run	1142928017 – 1143446417	3,535	62	6.92×10^{-16}
Second run	1144368017 – 1145606417	28,438	504	1.03×10^{-16}

Table 4.1: Summary table of the iKAGRA observation. N_{frames} and N_{SFTs} are the total number of frame files and SFT files available for CW analysis, respectively. The fifth column represents the best median value of the sensitivity for the first run and the second run.

4.2 SFT

4.2.1 SFT

In the frequency domain analysis, time series $x(t)$ data are broken up into smaller segments, followed by windowing of each segment with the Tukey window function $w(t)$ defined by Eq. (3.32). Then, each segment are converted into the frequency domain by the discrete Fourier transform:

$$\tilde{x}_{\alpha,k} = \Delta t \sum_{j=1}^{M} w_j x_{\alpha,j} e^{-2\pi i j k/M}, \tag{4.1}$$

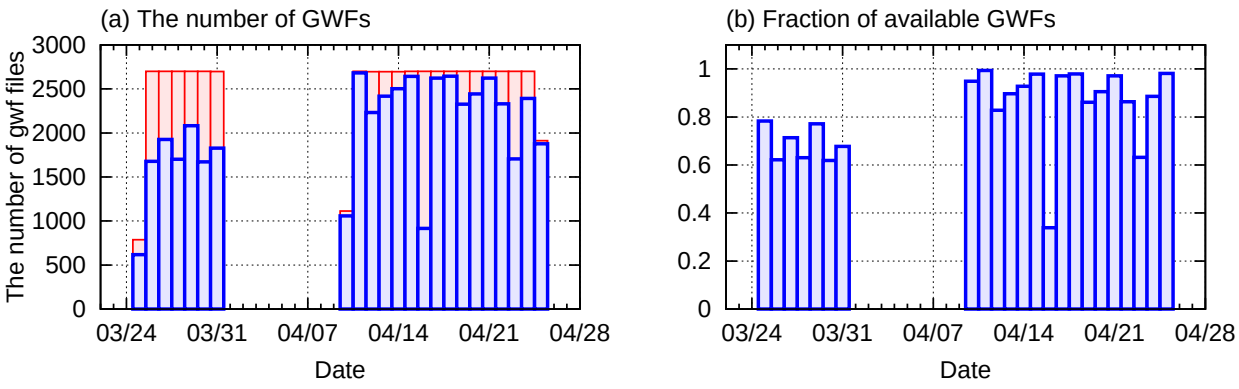

Figure 4.2: Left panel: Histogram of the number of frame files from the entire observation run as a function of date. The red filled area represents the total number of the frame files we obtained. The blue filled represents the total number of the frame files that are good state. Right panel: Fraction of available frame files as a function of date. Since the commissioning started after the March run, there are no frame files during the first week in April.

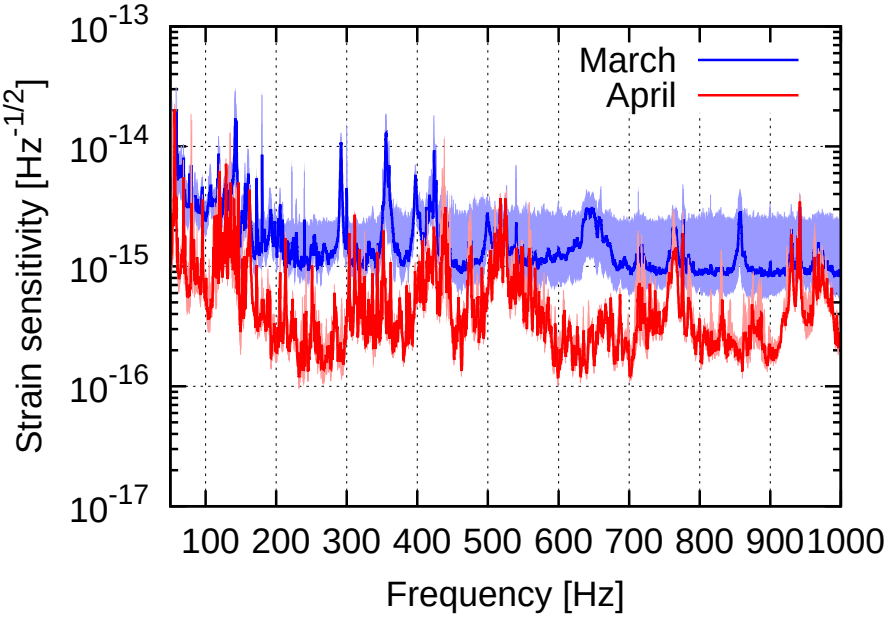

Figure 4.3: The measured GW strain-equivalent noise level of the iKAGRA. The blue and red lines correspond to the observation run during March (March 25 - March 31, 2016) and April (April 11 - April 25), respectively. The solid line represent the median sensitivity. The shaded zone represents the sensitivity between the 5th and 95th percentile. Since the April run is stable, the red-shaded zone is almost invisible in the above figure.

where $\tilde{x}_{\alpha,k}$ represents the Fourier component in the α-th SFT segment and k-th frequency bin. This process, referred to as SFT, is required to deal with non-stationarities of the detector and frequency-shifts caused by the Doppler effects due to the Earth motion. As discussed in section 3.2.2, the time baseline $T_{\rm SFT}$ is chosen such that the signal frequency does not shift by more than half a frequency bin during $T_{\rm SFT}$:

$$T_{\rm SFT} < \sqrt{\frac{1}{2}\frac{cR_{\rm E}}{f_0 v_{\rm E}^2}} \simeq 1.7 \times 10^3 \text{ sec} \left(\frac{1.5 \text{ kHz}}{f_0}\right)^{1/2}. \tag{4.2}$$

We set the time baseline of the SFT to be 1,800 seconds in our analysis.

A single SFT segment comprises 1,800-sec contiguous frame data each of which has 32 second length. Figure 4.4 (a) shows the number of the available SFT segments for GW analysis as a function of date. While 10 SFTs are produced on average in a day in March, about 30 SFTs are available in a day in April thanks to the updates during the commissioning. As a result of the SFT process, 29,801 frame files collected in the second run produced non-overlapping 528 SFTs. This corresponds to the total time baseline of about 11 days. When we performed the SFT, we employed MakeSFTs code in the LAL. In our analysis, we used the SFT data obtained only from the second run because there were insufficient number of SFTs in the first run, and furthermore, the sensitivity in the first run is much worse than that in the second run as shown in Fig. 4.3.

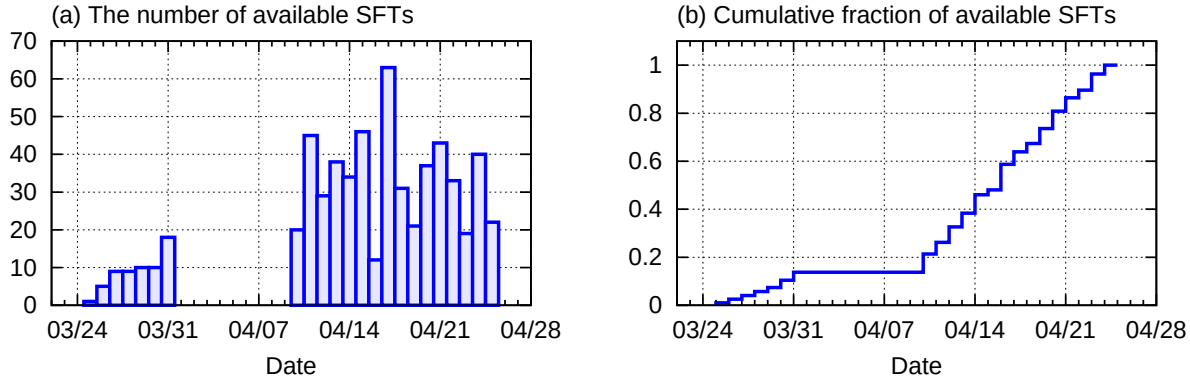

Figure 4.4: Left panel: Histogram of the number of available SFT segments as a function of date. Since the iKAGRA operated very unstably in March due to the tidal effects caused by the Moon and the Sun, we can use only about 10 SFTs in a day. On the other hand, in April, the number of available SFTs is about 30 in a day. Right panel: Cumulative fraction of available SFT segments as a function of date.

4.2.2 Data selection

Whereas detector noise can be regarded as approximately following Gaussian distribution, it often shows strong non-Gaussianities due to environment disturbances, which would degrade the detection power of the $\mathcal{F}$-statistic. SFT segments that contains strong outliers should be excluded in the analysis. In order to investigate statistical properties of data, it is useful to introduce a normalized SFT power. The normalized SFT power in the α-th SFT segment and the k-th frequency bin is defined as

$$P_{\alpha,k} \equiv \frac{|\tilde{x}_{\alpha,k}|^2}{\frac{1}{N_{\mathrm{band}}}\sum_{k'=0}^{N_{\mathrm{band}}-1}|\tilde{x}_{\alpha,k'}|^2}, \tag{4.3}$$

where N_{band} is the number of the frequency bins within the narrow band. In Eq. (4.3), the numerator represents the power in a single frequency bin, and the denominator represents the average value of the bin power over the narrow frequency band. It is advisable for the bandwidth N_{band} to be taken broader than the frequency shift of putative CW signals induced by the Doppler effect. If that is the case, $P_{\alpha,k}$ can be regarded as being dominated by the detector noise. When the detector noise obeys a Gaussian distribution, $P_{\alpha,k}$ follows the F-distribution $F\left(2, 2N_{\mathrm{band}}\right)$.

To find SFT segments that contain strong non-Gaussianity, we set a threshold for $P_{\alpha,k}$. If a value of $P_{\alpha,k}$ is beyond the threshold, we omit the SFT segment containing this $P_{\alpha,k}$. Let N_{SFT} random variables $X_1, \cdots, X_{N_{\mathrm{SFT}}}$ be distributed according to the F-distribution as $X \sim F\left(2, 2N_{\mathrm{band}}\right)$. For a given false-alarm rate, we define a probability such that the maximum value among $X_1, \cdots, X_{N_{\mathrm{SFT}}}$ exceeds a threshold P_{th} in the following way:

$$p_{\mathrm{FA}} = \mathrm{Prob}\left[\max\left(X_1, \cdots, X_{N_{\mathrm{SFT}}}\right) > P_{\mathrm{th}}\right]. \tag{4.4}$$

The right hand side in Eq. (4.4) can be reduced to

$$\mathrm{Prob}\left[\max\left(X_1, \cdots, X_{N_{\mathrm{SFT}}}\right) > P_{\mathrm{th}}\right] = 1 - \left[F\left(P_{\mathrm{th}}; 2, 2N_{\mathrm{band}}\right)\right]^{N_{\mathrm{SFT}}}, \tag{4.5}$$

where $F\left(P_{\mathrm{th}}; 2, 2N_{\mathrm{band}}\right)$ denotes the CDF (cumulative distribution function) of F-distribution. Since the false-alarm rate is usually set to be much smaller than 1, $p_{\mathrm{FA}} \ll 1$, Eq. (4.5) can be solved as

$$P_{\mathrm{th}} \simeq N_{\mathrm{band}}\left[\left(\frac{N_{\mathrm{SFT}}}{p_{\mathrm{FA}}}\right)^{1/N_{\mathrm{band}}} - 1\right]. \tag{4.6}$$

In our analysis, $N_{\mathrm{band}}, N_{\mathrm{SFT}}$, and p_{FA} are set to be $180, 540$, and 0.1%, respectively. The

resulting threshold of $P_{\rm th}$ is 13.6 beyond which $P_{\alpha,k}$ is regarded as following a non-Gaussian distribution.

Figure 4.5 (a) shows histogram of normalized SFT power over 0.1 Hz frequency band starting at 225.899 Hz as a representative example. This frequency corresponds to a CW signal from pulsar J0645+5158. The blue filled area represents the measured value of $P_{\alpha,k}$. If the detector noise in this band is distributed according to the Gaussian distribution, the histogram is expected to lie on the dotted line. The deviation between the histogram and the dotted line for large $P_{\alpha,k}$ indicates small non-Gaussianities in the detector noise. The mean and variance of $P_{\alpha,k}$ in this band are 1.07 and 1.24, respectively. The non-stationarity of the noise is described by the averaged sensitivity over a day shown in Fig. 4.5 (b). If the noise is completely stationary, the histogram follows the dotted line. The measured value of the averaged sensitivity varies on a few factors around $\sqrt{S_n\left(f\right)} = 2.9 \times 10^{-16}$ in this frequency band.

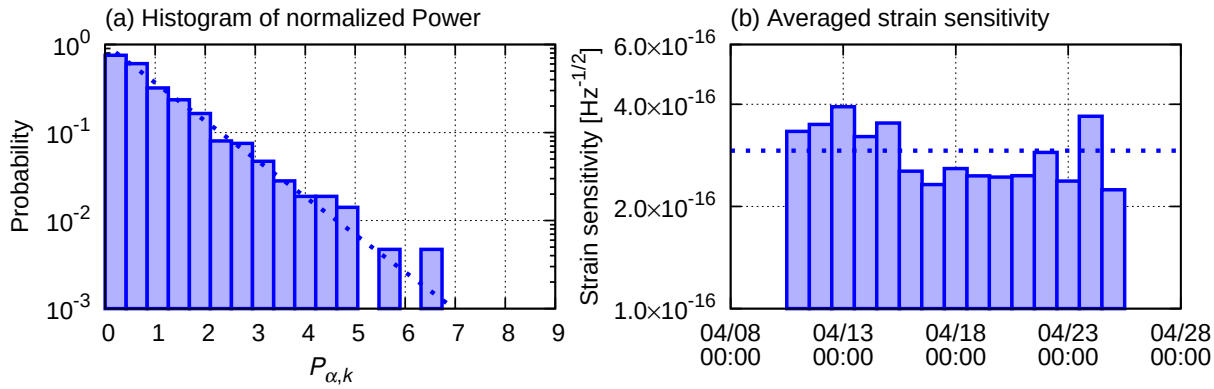

Figure 4.5: Left panel: Histogram of normalized SFT power over 180 frequency bins around $f = 225.899$ Hz corresponding to a CW signal from pulsar J0645+5158. In the case that detector noise is pure Gaussian noise, the normalized power is expected to obey F-distribution. In other words, the histogram lies on the straight line. The deviation between the histogram and the dotted line indicates the existence of non-Gaussian noise. Right panel: Strain sensitivity averaged over a day at around $f = 225.899$ Hz during the April run. The dotted line is the averaged value of the strain sensitivity.

4.3 Data analysis

4.3.1 Seach method

In our analysis, we use calibrated strain data $x\left(t\right)$ that pass all the aforementioned data quality check criteria. The strain data is expressed as a putative CW signal $s\left(t\right)$ with

additive detector noise $n\,(t)$:

$$x\,(t) = n\,(t) + s\,(t;\mathcal{A},\boldsymbol{\lambda})\,, \tag{4.7}$$

$$s\,(t;\mathcal{A},\boldsymbol{\lambda}) = F_+\,(t;\hat{\boldsymbol{n}},\psi)\,A_+\cos\Phi\,(t;\boldsymbol{\lambda}) + F_\times\,(t;\hat{\boldsymbol{n}},\psi)\,A_\times\sin\Phi\,(t;\boldsymbol{\lambda})\,, \tag{4.8}$$

where $F_{+,\times}$ and $A_{+,\times}$ denote detector antenna patterns and CW amplitudes corresponding to $+, \times$ modes, respectively. The Doppler parameter $\boldsymbol{\lambda}$ is comprised of the sky position $\hat{\boldsymbol{n}}$, the spin frequency f, and the spin-down parameters $\dot{f}, \ddot{f}, \cdots$. When we search for CWs from known pulsars, these Doppler parameters are already measured by EM observations in advance. In contrast, the amplitude parameters $\mathcal{A}$ are the collection of four unknown parameters: the amplitude of the CW, h_0, the inclination angle, ι, the polarization phase, ψ, and the initial phase, ϕ_0. The signal strength is characterized by

$$h_0 = \frac{4\pi^2 G}{c^4 d}\varepsilon I_{zz} f_0^2, \tag{4.9}$$

where d, I_{zz}, and ε are the distance to the source, the moment of inertia, and the ellipticity, respectively. In the case of a targeted search, we can estimate the theoretically expected upper limit on h_0 as

$$\langle h_0\rangle^{p_{\rm FD}=10\%}_{p_{\rm FA}=1\%} \simeq 11.4\sqrt{\frac{S_n\,(f_{\rm sig})}{T_{\rm obs}}} = 1.17\times10^{-18}\left(\frac{\sqrt{S_n\,(f_{\rm sig})}}{10^{-16}\ {\rm Hz}^{-1/2}}\right)\left(\frac{11\ {\rm days}}{T_{\rm obs}}\right)^{1/2}, \tag{4.10}$$

where a false-alarm rate and a false-dismissal rate are set to be 1% and 10%, respectively.

Our analysis pipeline for CWs from known isolated pulsars is based on the $\mathcal{F}$-statistic method. In this method, there is no search parameter because the four unknown parameters $\mathcal{A} = \{h_0, \psi, \cos\iota, \phi_0\}$ are projected out in the process of maximization of the log-likelihood ratio over $\mathcal{A}$:

$$2\mathcal{F}\,(x,\boldsymbol{\lambda}_{\rm sig}) \equiv \max_{\mathcal{A}^\mu}\left[2\ln\Lambda\,(x;\mathcal{A}^\mu,\boldsymbol{\lambda}_{\rm sig})\right]. \tag{4.11}$$

The SNRs are related to the $\mathcal{F}$-statistic by $\mathrm{E}\left[2\mathcal{F}\right] = 4 + (\mathrm{S/N})^2$. Also, the threshold for the $\mathcal{F}$-statistic can be related to a false alarm probability $p_{\rm FA}$ by Eq. (2.50a). When the false alarm probability is set to be 1%, the threshold of $\mathcal{F}$-statistic is estimated to be $2\mathcal{F}_{\rm thr} = 13.3$ in the case of Gaussian noise. We make use of ComputeFstatistic_v2 code in the LAL to evaluate a $\mathcal{F}$-statistic value of each known pulsars.

Schematic view of the entire search pipeline for known pulsars are given in Fig. 4.6. First, we create 1,800-sec SFT segments from the set of contiguous frame files. Second, we compute $\mathcal{F}$-statistic coherently from the all the SFT segments. Then, the measured values of $2\mathcal{F}$ are compared with the threshold of the detection statistic. If the measured

value is above the threshold, we regard it as the signal candidate. If not, we proceed to set an upper limit on the strength of the signal.

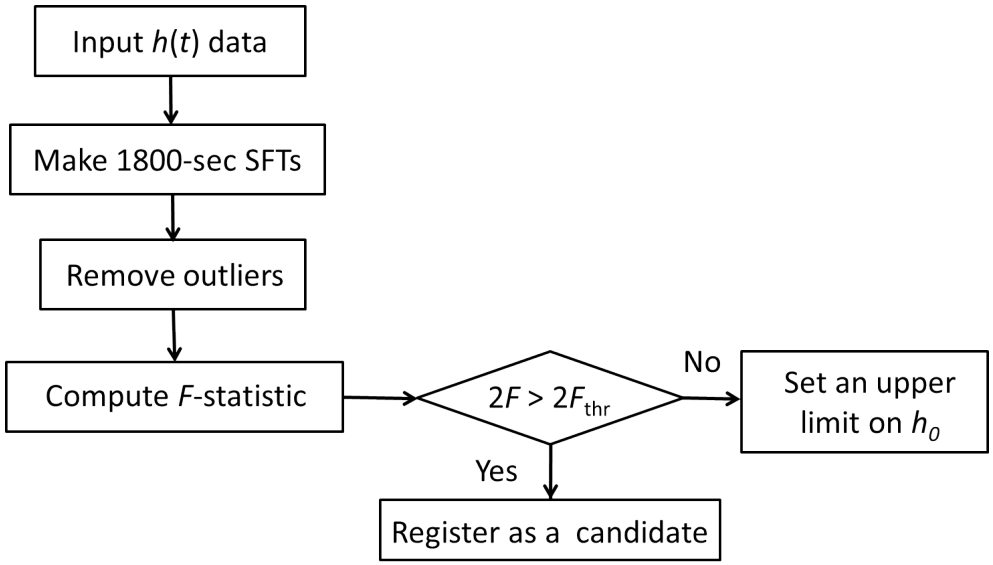

Figure 4.6: Entire search pipeline for known pulsars.

4.3.2 Results

If the data is consistent with stationary Gaussian noise, $2\mathcal{F}$ is distributed according to χ^2 distribution with four degrees of freedom. In order to investigate the actual PDF for the $2\mathcal{F}$, we compute the $\mathcal{F}$-statistics from the SFT segments within a narrow frequency band because the computed $2\mathcal{F}$ from noise at the nearby frequency can be regarded as different realizations of the same random process. Figure 4.7 represents probability distribution of the $\mathcal{F}$-statistics over 0.1 Hz band at around $f = 225.899$ Hz. This GW frequency corresponds to PSR J0645+5158 and its $2\mathcal{F}$ is 2.10. The blue-filled area represents the measured values and the dotted line represents the PDF in the case of stationary Gaussian noise. As can be seen in this figure, the two lines agree well with each other with the exception of large values of $2\mathcal{F}$. Since the small non-Gaussianities exist in the data, the deviation between the measured histogram and the dotted line appears for large $2\mathcal{F}$ as in the right panel of Fig. 4.7. The threshold of the $\mathcal{F}$-statistic can be set by the false-alarm rate. We set the false-alarm rate to be 1%. In this case, the threshold $2\mathcal{F}_{\rm thr}$ corresponds to the 99th percentile of the probability distribution in Fig. 4.7. For PSR J0645+5158, $2\mathcal{F}_{\rm thr} = 13.50$.

Figure 4.8 (a) shows the measured value of $2\mathcal{F}$ for 63 known isolated pulsars whose spin frequencies range between 50 and 1,000 Hz. Green dots represent the thresholds of $2\mathcal{F}$ that are derived from the actual probability distribution based on the iKAGRA data. The

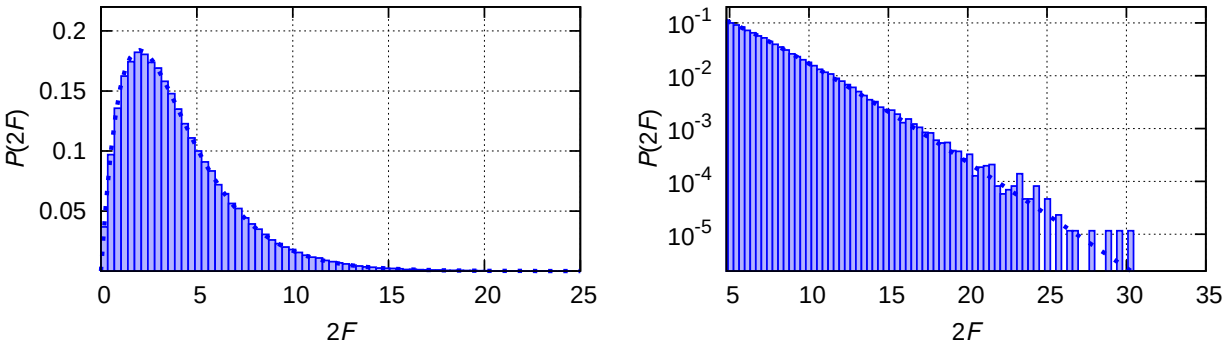

Figure 4.7: Probability distributions of the $\mathcal{F}$-statistic over 0.1 Hz band at around $f = 225.899$. The right panel is identical to the left panel apart from the scale of the vertical axis and the range of the horizontal axis. The blue shaded areas in both panels represent histograms obtained from the observations. In each panel, a dotted line represents a central χ^2 distribution with four degrees of freedom. When the data is dominated by Gaussian noise, the histogram obeys the dotted line.

thresholds are at around 13. This is because if noise obeys a Gaussian distribution, $2\mathcal{F}_{\rm thr} = 13.3$ for $p_{\rm FA} = 1\%$. Because all the computed values of $2\mathcal{F}$ fall below the predetermined threshold, we conclude that there is no significant candidate in our data. The left panel in Fig. 4.8 represents the upper limits on h_0 with a 95% confidence level. The upper limits are of the order of 10^{-18}. The most stringent upper limit is $h_0 \sim 7.5 \times 10^{-19}$ at 460.17 Hz from PSR J0024-7204L.

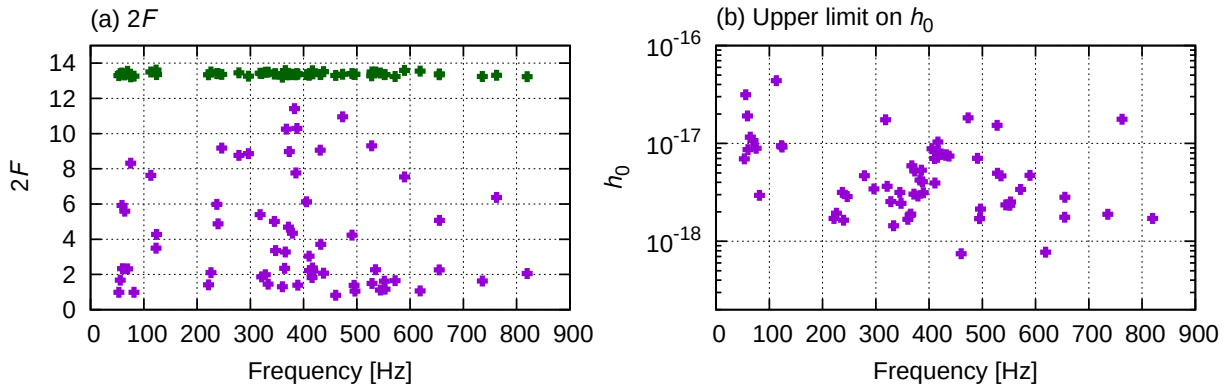

Figure 4.8: The left panel represents the observed value of the $\mathcal{F}$-statistic for each pulsar. Each green dot corresponds to the data-derived threshold of the $\mathcal{F}$-statistic for each pulsar. All the measured values of $2\mathcal{F}$ fall below the thresholds. The right panel represents the upper limits on the signal strength with a 95% confidence level. The most stringent upper limit is $h_0 \sim 7.5 \times 10^{-19}$ at 460.17 Hz from PSR J0024-7204L.

From Eq. (2.11b), the upper limits on h_0 can be also interpreted as the upper limits on

the ellipticity assuming $I = 10^{38}$ kg m^2, where I denotes the NS's moment of inertia:

$$\varepsilon = \frac{c^4 d}{16\pi^2 G I f_{\rm gw}^2} h_0. \tag{4.12}$$

The results are shown in Fig. 4.9 (a). All the upper limits are above unity. The most stringent upper limit is 3.0 at 819.9 Hz correpoding to J1658-5324. The spin-down ratio which is defined as $h_0^{95\%}/h_0^{\rm sd}$ is given in Fig. 4.9 (b). The lowest value of the spin-down ratio is 6.0×10^6 corresponding to J0534+2200 (Crab pulsar).

All the results we obtained are summarized in Table 4.2. Each column corresponds to pulsar name, GW frequency which is twice the spin frequency, the spin-down rate, the distance to the pulsar, the spin-down limit, the observed $2\mathcal{F}$ value, the data-derived threshold $2\mathcal{F}_{\rm thr}$, and upper limit on h_0 with a 95% confidence level, respectively. The values of $f_{\rm rot}, \dot{f}_{\rm rot}$, and d are taken from the ATNF catalogue [15]. The upper limits have a systematic error of about 20% due to detector calibration [132]. For pulsars with $\dot{f}_{\rm rot} > 0$, the spin-down rates are calcurated under the assumption of a characteristic pulsar age of 10^9 year by Eq. (2.1).

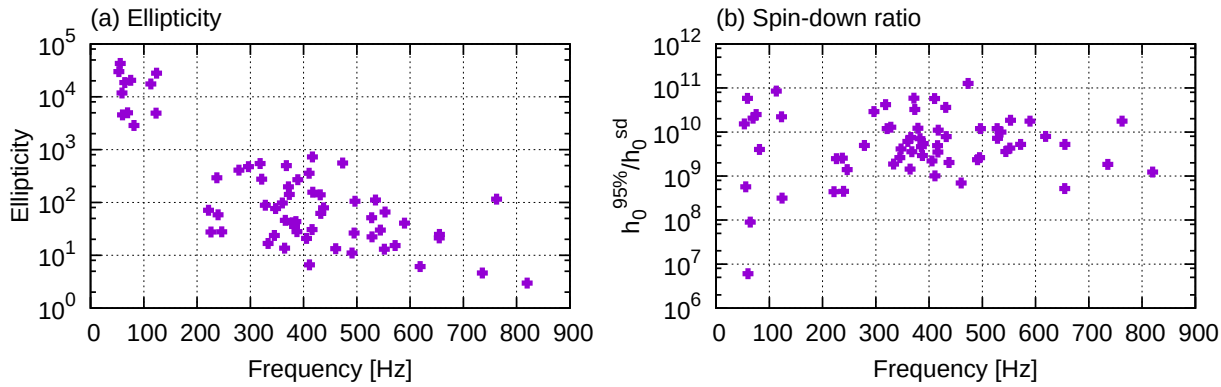

Figure 4.9: Left panel represents the upper limits on ellipticities of NSs assuming $I = 10^{38}$ kg m^2. The right panel represents the spin-down ratios. The lowest value of the spin-down ratio is 6.0×10^6 corresponding to J0534+2200 (Crab pulsar).

Table 4.2: Upper limits on GW amplitude for known isolated pulsars.

Pulsar	$f_{\rm gw}$ **(Hz)**	$\dot{f}_{\rm rot}$ **(Hz s^{-1})**	d **(kpc)**	$h_0^{\rm sd}$	$2\mathcal{F}$	$2\mathcal{F}_{\rm thr}$	$h_0^{95\%}$
J0024-7204C	347.41	1.5×10^{-15}	4.0	1.1×10^{-27}	3.35	13.40	2.4×10^{-18}
J0024-7204D	373.30	1.1×10^{-16}	4.0	1.1×10^{-27}	8.98	13.34	5.2×10^{-18}

Table 4.2: Upper limits on GW amplitude for known isolated pulsars.

Pulsar	$f_{\mathbf{gw}}$ **(Hz)**	$\dot{f}_{\mathbf{rot}}$ **(Hz s^{-1})**	d **(kpc)**	$h_0^{\mathbf{sd}}$	$2\mathcal{F}$	$2\mathcal{F}_{\mathbf{thr}}$	$h_0^{95\%}$
J0024-7204F	762.31	-9.3×10^{-15}	4.0	9.9×10^{-28}	6.37	13.31	1.7×10^{-17}
J0024-7204G	495.00	2.5×10^{-15}	4.0	1.1×10^{-27}	1.38	13.35	1.7×10^{-18}
J0024-7204L	460.17	6.4×10^{-15}	4.0	1.1×10^{-27}	0.81	13.30	7.4×10^{-19}
J0024-7204M	543.97	2.8×10^{-15}	4.0	1.1×10^{-27}	1.11	13.43	2.3×10^{-18}
J0024-7204N	654.88	2.3×10^{-15}	4.0	1.1×10^{-27}	5.06	13.38	2.8×10^{-18}
J0030+0451	411.06	-4.2×10^{-16}	0.3	3.8×10^{-27}	2.21	13.37	3.9×10^{-18}
J0534+2200	59.89	-3.7×10^{-10}	2.0	1.4×10^{-24}	2.32	13.37	8.6×10^{-18}
J0537-6910	124.05	-1.9×10^{-10}	49.7	2.9×10^{-26}	4.26	13.35	9.1×10^{-18}
J0645+5158	225.89	-6.2×10^{-17}	0.7	7.8×10^{-28}	2.10	13.50	1.9×10^{-18}
J0711-6830	364.23	-4.9×10^{-16}	1.0	1.2×10^{-27}	2.35	13.40	1.8×10^{-18}
J0931-1902	431.21	-1.9×10^{-16}	3.6	2.0×10^{-28}	9.06	13.34	7.5×10^{-18}
J1024-0719	387.43	-6.9×10^{-16}	1.1	1.3×10^{-27}	10.29	13.40	4.0×10^{-18}
J1038+0032	69.32	-8.0×10^{-17}	2.3	5.1×10^{-28}	2.32	13.53	1.0×10^{-17}
J1103-5403	589.49	-3.2×10^{-16}	3.1	2.6×10^{-28}	7.54	13.58	4.7×10^{-18}
J1400-6325	64.14	-4.0×10^{-11}	7.0	1.2×10^{-25}	5.59	13.33	1.1×10^{-17}
J1453+1902	345.28	-3.4×10^{-16}	0.9	1.2×10^{-27}	5.01	13.38	3.1×10^{-18}
J1518+0204A	360.12	-1.3×10^{-15}	8.0	2.7×10^{-28}	1.30	13.19	1.6×10^{-18}
J1552-4937	318.25	-4.8×10^{-16}	3.3	4.1×10^{-28}	5.39	13.43	1.7×10^{-17}
J1629-6902	333.3	-2.7×10^{-16}	1.3	7.6×10^{-28}	1.44	13.48	1.4×10^{-18}
J1658-5324	819.90	-1.8×10^{-15}	1.2	1.3×10^{-27}	2.05	13.23	1.7×10^{-18}
J1721-2457	571.97	-4.5×10^{-16}	1.5	6.5×10^{-28}	1.64	13.24	3.3×10^{-18}
J1725-3853	417.37	-2.2×10^{-15}	3.4	7.6×10^{-28}	2.19	13.39	8.3×10^{-18}
J1730-2304	246.22	-3.0×10^{-16}	0.6	2.0×10^{-27}	9.17	13.35	2.8×10^{-18}
J1744-1134	490.85	-5.3×10^{-16}	0.4	2.9×10^{-27}	4.23	13.41	7.0×10^{-18}
J1748-2021C	321.18	1.5×10^{-15}	8.2	5.5×10^{-28}	1.86	13.41	3.6×10^{-18}
J1748-2021E	122.97	-1.1×10^{-15}	8.2	4.2×10^{-28}	3.49	13.61	9.5×10^{-18}
J1748-2446C	237.07	8.5×10^{-15}	5.5	8.2×10^{-28}	5.98	13.41	3.1×10^{-18}
J1750-3703C	75.27	1.4×10^{-15}	13.8	3.2×10^{-28}	8.32	13.22	8.9×10^{-18}
J1750-3703D	389.11	-1.8×10^{-14}	13.8	5.7×10^{-28}	1.38	13.37	3.1×10^{-18}
J1757-27	113.07	-6.7×10^{-16}	5.4	5.1×10^{-28}	7.62	13.50	4.3×10^{-17}
J1801-0857A	278.72	9.9×10^{-15}	7.2	6.3×10^{-28}	8.76	13.45	4.6×10^{-18}
J1801-0857C	534.94	4.6×10^{-15}	7.2	6.3×10^{-28}	2.27	13.50	4.6×10^{-18}

Table 4.2: Upper limits on GW amplitude for known isolated pulsars.

Pulsar	$f_{\mathbf{gw}}$ **(Hz)**	$\dot{f}_{\mathbf{rot}}$ **(Hz s^{-1})**	d **(kpc)**	$h_0^{\mathbf{sd}}$	$2\mathcal{F}$	$2\mathcal{F}_{\mathbf{thr}}$	$h_0^{95\%}$
J1801-0857D	473.20	-3.9×10^{-16}	7.2	1.4×10^{-28}	10.95	13.37	1.8×10^{-17}
J1801-1417	551.70	-4.0×10^{-16}	1.8	5.4×10^{-28}	1.61	13.35	2.3×10^{-18}
J1821+0155	59.20	-2.5×10^{-17}	2.2	3.2×10^{-28}	5.92	13.44	1.9×10^{-17}
J1823-3021A	367.64	-1.1×10^{-13}	12.1	1.6×10^{-27}	10.25	13.34	5.9×10^{-18}
J1824-2452A	654.81	-1.7×10^{-13}	5.5	3.3×10^{-27}	2.26	13.34	1.7×10^{-18}
J1832-0836	735.53	-1.1×10^{-15}	1.4	1.0×10^{-27}	1.62	13.24	1.8×10^{-18}
J1836-2354B	618.75	4.6×10^{-17}	3.2	1.4×10^{-27}	1.06	13.54	7.7×10^{-19}
J1843-1448	365.54	-2.0×10^{-16}	3.4	2.5×10^{-28}	3.27	13.57	1.8×10^{-18}
J1904+0451	328.28	-1.5×10^{-16}	3.9	1.9×10^{-28}	1.97	13.48	2.5×10^{-18}
J1905+0400	528.48	-3.4×10^{-16}	1.3	6.9×10^{-28}	1.49	13.50	4.9×10^{-18}
J1910-5959B	239.29	1.1×10^{-14}	2.1	2.1×10^{-27}	4.87	13.39	1.6×10^{-18}
J1910-5959C	378.98	-7.7×10^{-17}	2.1	2.3×10^{-28}	4.33	13.36	2.8×10^{-18}
J1910-5959D	221.35	-1.1×10^{-14}	2.1	3.8×10^{-27}	1.40	13.34	1.7×10^{-18}
J1910-5959E	437.46	2.0×10^{-14}	2.1	2.1×10^{-27}	2.07	13.51	7.4×10^{-18}
J1911+0101B	371.44	6.9×10^{-17}	9.5	4.7×10^{-28}	4.68	13.42	3.0×10^{-18}
J1911+1347	432.34	-8.0×10^{-16}	1.6	9.6×10^{-28}	3.71	13.35	7.6×10^{-18}
J1913+1011	55.69	-2.6×10^{-12}	4.4	5.5×10^{-26}	1.67	13.41	3.1×10^{-17}
J1923+2515	527.96	-6.5×10^{-16}	0.9	1.2×10^{-27}	9.30	13.27	1.5×10^{-17}
J1944+0907	385.71	-6.3×10^{-16}	1.2	1.1×10^{-27}	7.76	13.33	5.3×10^{-18}
J1944+2236	552.79	-5.7×10^{-16}	8.4	1.3×10^{-28}	1.16	13.34	2.5×10^{-18}
J1955+2527	410.44	-3.8×10^{-16}	9.0	1.2×10^{-28}	3.03	13.31	7.0×10^{-18}
J2007+2722	81.64	-1.6×10^{-15}	6.8	7.3×10^{-28}	0.98	13.26	2.9×10^{-18}
J2010-1323	382.90	-1.7×10^{-16}	1.2	6.0×10^{-28}	11.41	13.35	4.2×10^{-18}
J2124-3358	405.58	-8.4×10^{-16}	0.4	4.0×10^{-27}	6.12	13.34	8.8×10^{-18}
J2129+1210D	416.42	4.6×10^{-13}	12.9	3.5×10^{-28}	2.36	13.56	1.0×10^{-17}
J2129+1210F	496.64	-2.0×10^{-15}	12.9	1.7×10^{-28}	1.05	13.37	2.1×10^{-18}
J2129+1210G	53.10	-1.4×10^{-15}	12.9	4.5×10^{-28}	0.98	13.29	6.9×10^{-18}
J2129+1210H	296.58	-5.3×10^{-16}	12.9	1.1×10^{-28}	8.86	13.26	3.4×10^{-18}
J2322+2057	415.93	-4.1×10^{-16}	0.7	1.4×10^{-27}	1.82	13.41	7.2×10^{-18}

Notes: The upper limits $h_0^{95\%}$ entail detector calibration errors about 20% [132]. For pulsars with $\dot{f}_{\rm rot} > 0$, the spin-down rates are estimated under the assumption of a characteristic pulsar age of

10^9 year by Eq. (2.1). The pulsar's spin frequencies, spin-down rates, and the distances are taken from the ATNF catalogue [15].

4.4 Future prospects

Figure 4.10 shows bKAGRA sensitivity and amplitudes of CW signals from 220 known isolated pulsars in the case of one-year observation. The solid line is calculated by Eq. (4.10) assuming VRSE configuration for bKAGRA [133]. Spin-down limits for known isolated pulsars given in Eq. (2.57) are represented by dots in this figure. The dots that exceed the solid line correspond to detectable signal candidates because thier spin-down rates cannot be explained only by the loss of GW radiations. As can be seen in Fig. 4.10, strength of GW signals from young pulsars in lower-frequency region is likely to be constrained more strictly than millisecond pulsars in spite of the fact that $h \propto f_0^2$ (see Eq. (4.9)). This can be traced to the fact that young pulsars are likely to have larger spin-down rates. The panels (a) and (b) of Fig. 4.11 represent pulsar distributions for spin-down ratios and upper limits on ellipticities that we will obtain in bKAGRA observations. About 50 pulsars with $2f_{\rm rot} > 10$ Hz would emit GWs strong enough to beat the spin-down limits. The panel (b) of Fig. 4.11 indicates that upper limits on ellipticities we would obtain fall much below the theoretical maximum possible value suggested by Eq. (2.4). It should be noted that Fig. 4.11 depends on pulsar models. We assume a fiducial moment of inertia of 10^{38} kg m^2. However, actual moments of inertia are theoretically expected to range between 1–3 $\times 10^{38}$ kg m^2 when equations-of-state are taken into account [64]. So, these spin-down limits may increase up to a factor of about 1.7. Distances to pulsars are basically inferred from radio dispersion measures and are subject to uncertainties uncertainties of about $\pm 10\%$. Table 4.3 summarizes seven high interest pulsars whose spin-down ratios are below 0.1. In particular, spin-down ratios of Crab (J0534+2200) and Vela (J0835-4510) pulsars will be beaten significantly by bKAGRA observations although frequencies around 60 Hz may be contaminated by narrow-band noise due to electrical power supply system.

4.5 Conclusion

The observation run of the iKAGRA operated for about three weeks in March and April in 2016. We constructed the analysis pipeline for known isolated pulsars based on the $\mathcal{F}$-statistic method and investigated performance of our pipeline using the iKAGRA data. We focused on the data from the second run in April and made use of the 28,438 32-sec frame files. We produced 504 1,800-sec SFT segments from the contiguous frame files.

Pulsar	$f_{\mathbf{gw}}$ **(Hz)**	$\dot{f}_{\mathbf{rot}}$ **(Hz s^{-1})**	d **(kpc)**	$h_0^{\mathbf{sd}}$	$h_0^{\mathrm{sd}}/\langle h_0 \rangle$
J0835-4510	22.38	-1.5×10^{-11}	0.2	3.4×10^{-24}	0.019
J0205+6449	30.43	-4.4×10^{-11}	3.2	4.3×10^{-25}	0.076
J1833-1034	32.31	-5.2×10^{-11}	4.1	3.5×10^{-25}	0.082
J2229+6114	38.74	-2.9×10^{-11}	3.0	3.3×10^{-25}	0.060
J1813-1749	44.74	-6.3×10^{-11}	4.7	2.8×10^{-25}	0.052
J0534+2200	59.89	-3.7×10^{-10}	2.0	1.4×10^{-24}	0.006
J1400-6325	64.14	-4.0×10^{-11}	7.0	1.2×10^{-25}	0.070

Table 4.3: Seven high interest pulsars whose spin-down ratios fall below 0.1. The moments of inertia are assumed to be 10^{38} kg m^2.

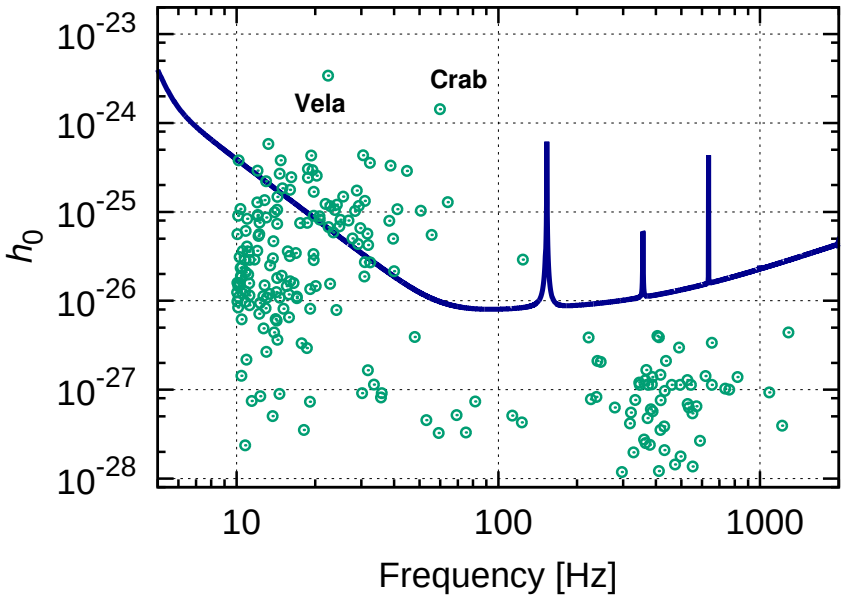

Figure 4.10: bKAGRA sensitivity and amplitudes of CW signals from known isolated pulsars for one-year observation. The solid line is calculated by Eq. (4.10) assuming VRSE configuration for bKAGRA [133]. The dots represent spin-down ratios for pulsars. The moments of inertia are assumed to be 10^{38} kg m^2. For pulsars with $\dot{f}_{\mathrm{rot}} > 0$, the spin-down rates are estimated under the assumption of a characteristic pulsar age of 10^9 year by Eq. (2.1).

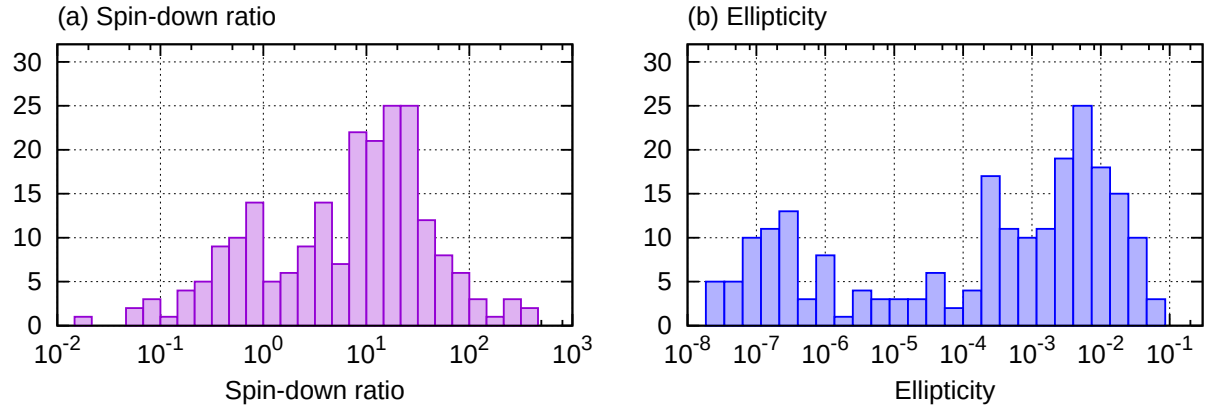

Figure 4.11: Pulsar distributions for spin-down ratios and upper limits on ellipticities we would obtain in bKAGRA observations. Spin-down ratios can be estimated by Eq. (2.57). Ellipticities are related to spin-down ratios by Eq. (4.9).

We computed the $\mathcal{F}$-statistic coherently from the entire observation data and found that there are no significant candidates in our data. Thus, we put constraints on the over-all amplitude of GWs and obtained Fig 4.8. The upper limits are of the order of 10^{-18} which are consistent with the upper limits estimated from the iKAGRA noise level. The most stringent upper limit is $h_0 \sim 7.5 \times 10^{-19}$ at 460.17 Hz corresponding to PSR J0024-7204L. We confirmed that our search pipeline correctly operates as expected. This search pipeline will be able to be applied to data from bKAGRA in the near future.

Chapter 5

χ^2 veto for $\mathcal{F}$-statistic-based semi-coherent search

CWs are considered to be one of the most interesting detectable targets for large-scale laser interferometric GW detectors such as the advanced LIGO [10], advanced Virgo [11], KAGRA [12], and LIGO-India [13]. CWs are generated from rapidly rotating neutron stars due to the non-axisymmetry around their spin axes. Broadly speaking, there exist two main approaches to search for CW signals. One is the so-called targeted search in which the source parameters such as sky position α, δ, spin frequency f, and spin-down rate $\dot{f}$ are already measured by EM observations. In this case, it is possible to analyze year-long observation data coherently by the most optimal method known as $\mathcal{F}$-statistic (Sec. 2.3) [57]. The other approach is often referred to as wide-parameter-space search whose main targets are electromagnetically undiscovered CW sources[1]. Since the aforementioned source parameters are unknown completely, it is necessary to explore a wide-parameter-space characterizing CW signals, in which case the coherent matched-filtering method are computationally prohibitive (Sec. 2.5.1) [136].

In order to reduce computational burden in wide-parameter-space search, semi-coherent approach has been developed by many authors [86, 137, 87, 138, 139, 140]. In a hierarchical semi-coherent search, year-long observation data is split up into segments small enough to allow us to analyze each segment coherently. Coherent detection statistic called $\mathcal{F}$-statistic is computed for each coherent segment on a coarse grid of templates. Then, $\mathcal{F}$-statistic are summed over all the coherent segments incoherently on a common fine grid. Significant candidates are followed up by fully coherent search using all the observation data. However, since such wide parameter-space search entails a huge number of templates, many narrow-band disturbances, or lines agree well with the signal templates and result in the high SNRs accidentally.

[1] Wide-parameter-space search is generally divided into two categories: directed search and all-sky search. All-sky search aims to detect CWs from undiscovered sources whose parameters are unknown at all, in which case search parameter space consists of $\alpha, \delta, f, \dot{f}, \ddot{f}, \cdots$. Directed search aims to detect CWs from unknown pulsars in the direction where CW sources potentially exist, in which case search parameter space consists of $f, \dot{f}, \ddot{f}, \cdots$. This search method lies between a targeted search and an all-sky search. The first directed search has been conducted using LIGO S5 data sets from H1 and L1 detectors, searching for unknown isolated pulsars in the direction of the Galactic center [134, 135].

Line cleaning [85, 111, 113] is often used to veto known instrumental lines. The frequency bands contaminated by such instrumental noise artifacts are identified through detector characterization. On the other hand, many methods for dealing with unknown lines are proposed. S-veto [85, 109] utilizes such a noise property that signal candidates stemming from instruments and environment are not subject to frequency modulations due to the Earth's rotation and revolution. This method removes the sky regions around the north and south poles from search parameter space, where noise lines behave as if they were CW signals. The veto method called line-robust statistics has been recently proposed by Keitel et al. [141, 142, 143]. Using the Bayesian framework, the authors constructed the line-robust statistics by introducing an alternative simple line-noise hypothesis in addition to the signal hypothesis $\mathcal{H}_{\rm S}$ and the Gaussian-noise hypothesis $\mathcal{H}_{\rm G}$ (Sec. 2.4.4). Since in their works a line is modeled as a CW-like signal which appears only in a single detector , one of the drawbacks is incapability of rejecting coincident line-noise events in a multi-detector network.

In this chapter, we introduce a χ^2 veto in $\mathcal{F}$-statistic-based semi-coherent search for unknown CW signals and study its performance. A χ^2 veto is widely used in compact binary coalescence (CBC) search in order to exclude non-Gaussian noise transients which would produce high SNR accidentally [144, 1]. The key idea of a χ^2 veto is that a SNR of transient noise accumulates with time in a different way from that of a true CBC signal. If the SNR of the signal candidate builds up in a way that is inconsistent with the expected CBC signal, the value of χ^2 becomes large and indicates that the signal candidate should be vetoed. A χ^2 veto was also applied to a targeted CW search in [145] where line events are rejected according to the spectral shape of the observed $\mathcal{F}$-statistics around a CW frequency. A χ^2 veto is discussed in the context of Hough transform search [146].

This chapter is organized as follows. In section 5.1, we summarize $\mathcal{F}$-statistic-based semicoherent search. We give an overview of currently proposed veto methods for wide-parameter-space search in section 5.2. In section 5.3, we formulate a χ^2 veto for $\mathcal{F}$-statistic-based semicoherent search in the case of equal-SNR time-intervals and validate it by using simulation data. Then, we test its detection power using actual LIGO data in section 5.4. A summary follows in section 5.5.

5.1 $\mathcal{F}$-statistic-based semi-coherent search

We will start with summarizing $\mathcal{F}$-statistic-based semi-coherent search. The detection statistic called $\mathcal{F}$-statistic is widely used to detect a CW signal from an electromagnetically known isolated pulsar. This is a coherent matched filtering based on the maximum likelihood method, which is known as the most optimal detection statistic from a fre-

quentist viewpoint [72]. For a stationary Gaussian noise, the likelihood ratio is expressed as

$$\ln \Lambda = (x|h) - \frac{1}{2}(h|h), \tag{5.1}$$

where x and h are the detector output and the CW waveform, respectively. $(\cdot|\cdot)$ appeared in Eq. (5.1) denotes the noise-weighted inner product defined by

$$(x|y) = 4\mathrm{Re}\int_0^\infty \frac{\tilde{x}(f)\,\tilde{y}^*(f)}{S_n(f)}df, \tag{5.2}$$

where $S_n(f)$ is a one-sided noise power spectral density. The $\mathcal{F}$-statistic is derived by maximization of the likelihood ratio over amplitude parameters $\mathcal{A}^\mu$ which consist of the overall amplitude h_0, the inclination ι, the polarization phase ψ, and the initial phase ϕ_0 [57],

$$2\mathcal{F} = \max_{\mathcal{A}^\mu} 2\ln\Lambda. \tag{5.3}$$

The four amplitude parameters are projected out by this process. In the case of an all-sky search, the parameters to be searched are the remaining phase parameters which are composed of the sky positions, the frequency, and the spin-down parameters. Even when we retain the spin-down effects up to the first order, the number of required templates grows up with coherent-integration time polynomially [77]. Thus, it is computationally impossible to perform a fully coherent search for year-long data.

A semi-coherent search method mitigates the computational cost by taking a sub-optimal strategy at the cost of sensitivity. A data set is broken up into N_{seg} shorter segments typically of the order of a day or longer. The $\mathcal{F}$-statistics are computed from each segment and then combined incoherently. The resulting detection statistic is an average of the $\mathcal{F}$-statistics over N_{seg} segments,

$$\overline{2\mathcal{F}} = \frac{1}{N_{\mathrm{seg}}}\sum_{j=1}^{N_{\mathrm{seg}}} 2\mathcal{F}_j, \tag{5.4}$$

where the index j stands for the j-th coherent segment. The significant candidates are followed up by fully coherent search by using the entire observation data.

5.2 Veto method

In this section, we give a brief review of commonly used veto methods in $\mathcal{F}$-statistic-based semi-coherent search.

5.2.1 Known lines

Line-cleaning

Line cleaning [85, 111, 113] is used to remove narrow-frequency bands that are known to suffer from instrumental artifacts, or known lines, because noise lines behave as CW signals and becomes signal candidates with high SNRs accidentally. Prominent contaminated frequency bands are often identified by data characterization. According to [113], there are various line sources including so-called the main lines at the 60 Hz electrical power supply frequency and its harmonics, calibration lines injected intendedly for the purpose of calibration, lines at violin-mode frequencies due to wire suspension systems, and 1 Hz Harmonic, known as 1 Hz combs, caused by control and data acquisition system. In the cleaning process, contaminated narrow-frequency bands are replaced by white Gaussian noise whose power spectrum is the same as noise level in the adjacent frequencies.

5.2.2 Unknown lines

S-veto

In the previous LIGO search [85, 109], S-veto has been employed to remove unpredicted noise lines. The S-veto is based on the fact that instrumental and environmental lines are not influenced by frequency modulations due to the Earth's rotation and revolution. In the process of the S-veto, sky regions around the Earth's pole are excluded from search-parameter-space before a search, because such lines are prone to mimic CW signals incoming from these regions. S-veto was originally used in the context of SFT-based semi-coherent searches (Sec. 2.5.2) [85]. Pletsch [147] generalized the S-veto to the $\mathcal{F}$-statistic-based semi-coherent CW search by using global-correlation equations. Time derivative of Eq. (2.22a) yields

$$\frac{df}{dt} = \left(1 + \frac{\boldsymbol{v}\left(t\right) \cdot \hat{\boldsymbol{n}}}{c}\right) \dot{\hat{f}} + \hat{f}\left(t\right) \frac{\boldsymbol{a}\left(t\right) \cdot \hat{\boldsymbol{n}}}{c}, \tag{5.5}$$

where $\boldsymbol{a}\left(t\right)$ denotes the acceleration of the detector. The first and second terms in the right hand side of Eq. (5.5) stems from the NS's spin down and the Earth's motion, respectively. Since signal candidates arising from instrumental and environmental lines are not subject to the frequency shifts induced by the Earth's motion, vetoed region is an annulus in the sky described by

$$\left| \dot{\hat{f}} + \hat{f}\left(t_{\text{fiducial}}\right) \frac{\left(\boldsymbol{\Omega} \times \boldsymbol{v}_{\text{E}}\right) \cdot \hat{\boldsymbol{n}}}{c} \right| < \varepsilon, \tag{5.6}$$

where $\boldsymbol{\Omega}, \boldsymbol{v}_{\text{E}}$, and ε represents the Earth's angular velocity vector, the Earth's orbital velocity vector, and the parameter originating from the finite resolutions of the parameter

space. The tolerance parameter ε can be written as

$$\varepsilon = \frac{\Delta f}{T_{\mathrm{obs}}} N_{\mathrm{cell}}, \tag{5.7}$$

where $\Delta f, T_{\mathrm{obs}}$, and N_{cell} denote the frequency resolution, the observation time, and the minimum total number of frequency bins occupied by CW signals, respectively. The sky region to be excluded is determined by Eq. (5.6). In [85], the fractions of the sky excluded from the search are about 15% for H1 and 26% for L1. In [109], about 30% of the sky are excluded.

Permanence veto

Permanence veto is used in semi-coherent searches based on $\mathcal{F}$-statistic [134, 135]. This method utilizes the fact that strong lines often appear only in a signle coherent segment. In the process of the permanence veto, the coherent segment containing the strongest lines is removed. Then, a value of $\mathcal{F}$-statistic is re-computed over the remaining $N_{\mathrm{seg}} - 1$ coherent segments:

$$\overline{2\mathcal{F}}_{+\mathrm{pv}} \equiv \frac{1}{N_{\mathrm{seg}} - 1} \sum_{j \neq k}^{N_{\mathrm{seg}}} 2\mathcal{F}_j, \tag{5.8a}$$

$$2\mathcal{F}_k \equiv \max_{k'} 2\mathcal{F}_{k'}, \tag{5.8b}$$

where the k-th segment is assumed to contain the strongest $\mathcal{F}$-statistic value. The new detection statistic $\overline{2\mathcal{F}}_{+\mathrm{pv}}$ is compared with the threshold. If the measured value of $\overline{2\mathcal{F}}_{+\mathrm{pv}}$ falls below the predetermined threshold, the signal candidate is regarded as arising from noise lines. The main draw-back of the permanence veto is not being able to treat noise lines appearing in two or more coherent segments.

Line-robust statistics

As discussed in Sec. 2.4.4, the $\mathcal{F}$-statistic can be formulated by the posterior odds ratio between the Gaussian-noise hypothesis $\mathcal{H}_{\mathrm{G}}$ and the signal hypothesis $\mathcal{H}_{\mathrm{S}}$ in the Bayesian framework. The $\mathcal{F}$-statistic can be used to decide which hypothesis agrees better with observation data. Hence, there is a possibility that noise lines produce a large value of $\mathcal{F}$-statistic even if it does not resemble a CW signal model. In order to deal with this problem, Keitel et al. [141, 142, 143] introduced the additional hypothesis that formulates line as

$$\mathcal{H}_{\mathrm{L}} \equiv \bigvee_{X=1}^{N_{\mathrm{det}}} \left(\mathcal{H}_{\mathrm{L}}^{X} \bigwedge_{Y \neq X} \mathcal{H}_{\mathrm{G}}^{Y} \right), \tag{5.9a}$$

$$\mathcal{H}_{\mathrm{L}}^{X} : x^{X}(t) = n^{X}(t) + s^{X}\left(t; \mathcal{A}^{X}\right), \tag{5.9b}$$

where $\mathcal{H}_{\mathrm{L}}^{X}$ is a hypothesis stating a CW-like line in a detector X. The simple line hypotheis $\mathcal{H}_{\mathrm{L}}$ assumes that only a single detector X contains a CW-like line and any other detectors $Y\,(\neq X)$ are comprised of pure Gaussian noise. Since the Gaussian noise hypothesis $\mathcal{H}_{\mathrm{G}}$ and the simple line hypothesis $\mathcal{H}_{\mathrm{L}}$ are mutually exclusive, the noise hypothesis can be extended as $\mathcal{H}_{\mathrm{GL}} \equiv \mathcal{H}_{\mathrm{G}} \vee \mathcal{H}_{\mathrm{L}}$. A new detection statistic, which is called a line-robust statistic, is constructed from a posterior odds ratio between the extended noise hypothesis $\mathcal{H}_{\mathrm{GL}}$ and the signal hypothesis $\mathcal{H}_{\mathrm{S}}$,

$$O_{\mathrm{S/GL}}(\boldsymbol{x}) \equiv \frac{P(\mathcal{H}_{\mathrm{S}}|\boldsymbol{x})}{P(\mathcal{H}_{\mathrm{GL}}|\boldsymbol{x})} = \left[O_{\mathrm{S/G}}^{-1}(\boldsymbol{x}) + O_{\mathrm{S/L}}^{-1}(\boldsymbol{x})\right]^{-1}, \tag{5.10}$$

where $P(\mathcal{H}_{\mathrm{GL}}|\boldsymbol{x}) = P(\mathcal{H}_{\mathrm{G}}|\boldsymbol{x}) + P(\mathcal{H}_{\mathrm{L}}|\boldsymbol{x})$. Computing $O_{\mathrm{S/G}}(\boldsymbol{x})$[2] and $O_{\mathrm{S/L}}(\boldsymbol{x})$[3] gives rise to the concrete expression for the line-robust statistic,

$$O_{\mathrm{S/GL}}(\boldsymbol{x}) = o_{\mathrm{S/GL}} \frac{e^{\mathcal{F}_{\mathrm{tot}}(\boldsymbol{x})}}{(1-p_{\mathrm{L}})\, e^{N_{\mathrm{seg}}\mathcal{F}_{*}^{(0)}} + \sum_{X} p_{\mathrm{L}}^{X} e^{\mathcal{F}^{X}\left(x^{X}\right)}}, \tag{5.14a}$$

$$p_L \equiv P(\mathcal{H}_{\mathrm{L}}|\mathcal{H}_{\mathrm{GL}}) = \frac{P(\mathcal{H}_{\mathrm{L}})}{P(\mathcal{H}_{\mathrm{GL}})} = \frac{o_{\mathrm{L/G}}}{1+o_{\mathrm{L/G}}}, \tag{5.14b}$$

$$p_L^{X} \equiv P\left(\mathcal{H}_{\mathrm{L}}^{X}|\mathcal{H}_{\mathrm{GL}}\right) = \frac{P\left(\mathcal{H}_{\mathrm{L}}^{X}\right)}{P(\mathcal{H}_{\mathrm{GL}})} = \frac{o_{\mathrm{L/G}}^{X}}{1+o_{\mathrm{L/G}}^{X}}, \tag{5.14c}$$

where c^* is reparameterized as $\mathcal{F}_{*}^{(0)} \equiv \ln c^*$. The line-robust statistic $B_{\mathrm{S/GL}}$ depends on N_{det} free prior parameters to be specified, $\mathcal{F}_{*}^{(0)}$ and p_{L}^{X}. The line priors p_{L}^{X} are estimated by reference to normalized average SFT powers for each detector. The prior $\mathcal{F}_{*}^{(0)}$ that arises from the amplitude-prior cutoff shown in Eq. (2.61) determines a transition scale

[2] Using a similar calculation to Eq. (2.61), the posterior odds between $\mathcal{H}_{\mathrm{G}}$ and $\mathcal{H}_{\mathrm{S}}$ in the case of semicoherent methods can be calculated as

$$O_{\mathrm{S/G}}(\boldsymbol{x}) = o_{\mathrm{S/G}} c_{*}^{-N_{\mathrm{seg}}} e^{\mathcal{F}_{\mathrm{tot}}(\boldsymbol{x})} \tag{5.11}$$

where $\mathcal{F}_{\mathrm{tot}}$ denotes the sum of the $\mathcal{F}$-statistics.

[3] The posterior probability for $\mathcal{H}_{\mathrm{L}}^{X}$ shown in Eq. (5.9b) is expressed as

$$P\left(\mathcal{H}_{\mathrm{L}}^{X}|x^{X}\right) = o_{\mathrm{L/G}}^{X} c_{*}^{-N_{\mathrm{seg}}} e^{\mathcal{F}^{X}\left(x^{X}\right)} P\left(\mathcal{H}_{\mathrm{G}}^{X}|x^{X}\right) \tag{5.12}$$

So, the posterior probability for the simple line hypothesis defined by Eq. (5.9a) is calculated as

$$P(\mathcal{H}_{\mathrm{L}}|\boldsymbol{x}) = \sum_{X} P\left(\mathcal{H}_{\mathrm{L}}^{X}|x^{X}\right) \prod_{Y\neq X} P\left(\mathcal{H}_{\mathrm{G}}^{Y}|x^{Y}\right) = P(\mathcal{H}_{\mathrm{G}}|\boldsymbol{x})\, c_{*}^{-N_{\mathrm{seg}}} \sum_{X} o_{\mathrm{L/G}}^{X} e^{\mathcal{F}^{X}\left(x^{X}\right)}, \tag{5.13a}$$

$$o_{\mathrm{L/G}} \equiv \frac{P(\mathcal{H}_{\mathrm{L}})}{P(\mathcal{H}_{\mathrm{G}})} = \sum_{X} o_{\mathrm{L/G}}^{X}. \tag{5.13b}$$

between $O_{\mathrm{S/G}}(\boldsymbol{x})$ and $O_{\mathrm{S/L}}(\boldsymbol{x})$ (see [141] for further discussion). The main draw-back of the line-robust statistic is not being able to handle coincident lines appearing in multiple detectors by its definition. Also, the line-robust statistic is not applicable to a single detector case.

5.3 The χ^2 veto in equal-SNR time intervals

As discussed in Sec. 2.3, the $\mathcal{F}$-statistic is known to be the most optimal detection statistic under ideal Gaussian noise background. However, non-Gaussian noise frequently appears in actual data output, which would degrades the detection efficiency. In particular, the $\mathcal{F}$-statistic is susceptible to narrow-band disturbances called lines which would lead to a high false-alarm rate. Furthermore, the detection statistic $\overline{2\mathcal{F}}$ composed of the $\mathcal{F}$-statistics could yield a large value beyond a detection threshold even when lines with high amplitudes appear in a few segments in the absence of a CW signal. This is because SNR consistency across the different coherent segments is not taken into account in the $\overline{2\mathcal{F}}$-statistic.

In this section, we construct χ^2 discriminator by focusing on SNR contained in each segment. A CW signal contributes to a SNR at a constant rate apart from amplitude modulation whereas a SNR arising from lines is expected to accumulate in a much different way from a CW signal. The χ^2 discriminator is designed to test the SNR consistency between the different segments.

5.3.1 χ^2 discriminator

We will start with putting some simplifying assumptions to be familiar with a χ^2 discriminator in a $\mathcal{F}$-statistic-based semi-coherent search. First, noise levels are set to be the same for each coherent segment longer than 24 hours. Second, each coherent segment has the same length. Third, a template is assumed to be perfectly matched with a true CW signal. Fourth, each segment is not overlapped. The first three assumptions are eventually relaxed later on in this chapter. From these assumptions, the $\mathcal{F}$-statistic computed from each segment can be approximately regarded as independent and identically distributed random variables. As explained in Appendix B, the expectation value and variance of the $\mathcal{F}$-statistic in the j-th segment are expressed by

$$\langle 2\mathcal{F}_j \rangle = 4 + \rho_j^2, \tag{5.15a}$$

$$\sigma^2_{2\mathcal{F}_j} = 4\left(2 + \rho_j^2\right), \tag{5.15b}$$

where the angle bracket $\langle \cdots \rangle$ denotes the ensemble average and ρ_j denotes the SNR in the j-th segment. Thanks to the aforementioned assumptions, the observed SNR contained in each segment is expected to take the same value.

Next, we consider statistical properties of the incoherent sum of the $\mathcal{F}$-statistics over all the coherent segments:

$$\mathcal{F}_{\rm tot} \equiv \sum_{j=1}^{N_{\rm seg}} \mathcal{F}_j, \tag{5.16}$$

in order to prepare for a χ^2 discriminator. In the presence of a CW signal with total SNR of $\rho_{\rm tot}$ in stationary Gaussian noise, $2\mathcal{F}_{\rm tot}$ obeys a non-central χ^2 distribution with $4N_{\rm seg}$ degrees of freedom and non-centrality $\rho^2_{\rm tot}$, where $\rho^2_{\rm tot} \equiv N_{\rm seg}\rho^2_j$. So, $2\mathcal{F}_{\rm tot}$ satisfies

$$\langle 2\mathcal{F}_{\rm tot} \rangle = N_{\rm seg}\left(4 + \rho_j^2\right), \tag{5.17a}$$

$$\sigma^2_{2\mathcal{F}_{\rm tot}} = 4N_{\rm seg}\left(2 + \rho_j^2\right). \tag{5.17b}$$

The total value of the $\mathcal{F}$-statistics can be decomposed into the following form:

$$\mathcal{F}^2_{\rm tot} = \sum_{j=1}^{N_{\rm seg}} \mathcal{F}_j^2 + \sum_{j=1}^{N_{\rm seg}} \sum_{k=1\neq j}^{N_{\rm seg}} \mathcal{F}_j\mathcal{F}_k, \tag{5.18}$$

where the second term represents the sum of the product $\mathcal{F}_j\mathcal{F}_k$ over the different indices. Since the detector noise in the different segments are regarded as independent of each other, the relation $\langle \mathcal{F}_j\mathcal{F}_k \rangle = \langle \mathcal{F}_j \rangle \langle \mathcal{F}_k \rangle$ is satisfied. Also, since the expection value of $\mathcal{F}_j$ takes the same value for all the segments thanks to the aforementioned assumptions, $\langle \mathcal{F}_j \rangle = \langle \mathcal{F}_k \rangle$ is satisfied for any set of j and k. Combining these two equations, we obtain

$$\begin{aligned}\langle \mathcal{F}^2_{\rm tot} \rangle &= N_{\rm seg}\langle \mathcal{F}_j^2 \rangle + N_{\rm seg}\left(N_{\rm seg} - 1\right)\langle \mathcal{F}_j \rangle^2 \\ &= N_{\rm seg}\left(1 + \rho_j^2\right) + N_{\rm seg}^2\left(1 + \frac{1}{2}\rho_j^2\right).\end{aligned} \tag{5.19}$$

This is consistent with Eqs. (5.17a) and (5.17b). In a similar way, $\langle \mathcal{F}_j\mathcal{F}_{\rm tot} \rangle$ is calculated as

$$\langle \mathcal{F}_j\mathcal{F}_{\rm tot} \rangle = N_{\rm seg}\left(1 + \frac{1}{2}\rho_j^2\right)^2 + \left(1 + \rho_j^2\right). \tag{5.20}$$

Next, we define $\Delta\mathcal{F}_j$ as the difference between measured value of $\mathcal{F}$ in the j-th segment

and the expected value of $\mathcal{F}$ in the j-th segment inferred from the measured value of $\mathcal{F}_{\rm tot}$,

$$\Delta\mathcal{F}_j \equiv \mathcal{F}_j - \frac{1}{N_{\rm seg}}\mathcal{F}_{\rm tot}. \tag{5.21}$$

The expectation value and variance of $\Delta\mathcal{F}_j$ are given by

$$\langle \Delta\mathcal{F}_j \rangle = 0, \tag{5.22a}$$

$$\langle (\Delta\mathcal{F}_j)^2 \rangle = \left(1 - \frac{1}{N_{\rm seg}}\right)\sigma^2_{\mathcal{F}_j}, \tag{5.22b}$$

where we made use of Eqs. (5.19) and (5.20). When CW signals with additive Gaussian noise exist in the j-th segment, $\Delta\mathcal{F}_j$ takes zero expectation value as indicated by Eq. (5.22a). On the other hand, in the presence of non-Gaussian noise in the j-th segment, $\Delta\mathcal{F}_j$ takes non-zero expectation value. Thus, the sum of $(\Delta\mathcal{F}_j)^2$ over all the segments can be regarded as the measure to distinguish CW signals from non-Gaussian noises.

Motivated by this fact, we define a χ^2 discriminator as

$$\bar{\chi}^2 \equiv \frac{N_{\rm seg}}{\sigma^2_{\mathcal{F}_{\rm tot}}}\sum_{j=1}^{N_{\rm seg}}(\Delta\mathcal{F}_j)^2 = \sum_{j=1}^{N_{\rm seg}}\frac{\left|2\mathcal{F}_j - \overline{2\mathcal{F}}\right|^2}{\sigma^2_{2\mathcal{F}_{\rm tot}}/N_{\rm seg}}. \tag{5.23}$$

After a simple calculation, the expectation value and variance of $\bar{\chi}^2$ are calculated as

$$\langle \bar{\chi}^2 \rangle = N_{\rm seg} - 1, \tag{5.24a}$$

$$\sigma^2_{\bar{\chi}^2} = \frac{N_{\rm seg}-1}{N_{\rm seg}}\left[2\left(N_{\rm seg}-1\right) + \left(N^2_{\rm seg} - 3N_{\rm seg} + 3\right)\beta_{2\mathcal{F}_{\rm tot}}\right], \tag{5.24b}$$

respectively, where $\beta_{2\mathcal{F}_{\rm tot}}$ denotes the kurtosis of $2\mathcal{F}_{\rm tot}$ defined by Eq. (B.6d) (see Appendix E). It should be noted that the mean of $\bar{\chi}^2$ depends only on the number of the coherent segments, whereas the variance depends not only on the number of the segments but also on the total SNR through the kurtosis $\beta_{2\mathcal{F}_{\rm tot}}$. This dependence differs from the original χ^2 discriminator introduced in Ref. [144]. For large values of $N_{\rm seg}$, $\sigma^2_{\bar{\chi}^2}$ approaches to $2\left(N_{\rm seg}-1\right)$ and the $\bar{\chi}^2$ discriminator approximately obeys a χ^2 distribution with $N_{\rm seg}-1$ degrees of freedom. This fact can be traced to the central limit theorem. The probability distribution function (PDF) of $2\mathcal{F}$ approaches to a Gaussian distribution as the number of segment $N_{\rm seg}$ increases. In this situation, we can directly reuse the result of [144] which indicates that the χ^2 discriminator composed of $N_{\rm seg}$ segments is distributed as a χ^2 distribution with $N_{\rm seg}-1$ degrees of freedom.

5.3.2 The threshold of χ^2 discriminator

As explained in the previous subsection, the χ^2 discriminator can be used to discriminate whether signal candidates with large values of $\overline{2\mathcal{F}}$ arise from line-noise events or not. CW signals with additive Gaussian noise are expected to have $\bar{\chi}^2$ of $N_{\rm seg}-1$ on the average from Eq. (5.24a), whereas lines are expected to have large values of $\bar{\chi}^2$ compared with $N_{\rm seg}-1$. Signal candidates which exceed a certain threshold of $\bar{\chi}^2$ should be rejected. The threshold can be determined by Monte-Calro simulations for a given number of coherent segments $N_{\rm seg}$. In the left panel of Fig. 5.1, we depict a threshold of $\bar{\chi}^2$ in the case of $N_{\rm seg} = 100$ as a function of $\overline{2\mathcal{F}}$, where $\overline{2\mathcal{F}} \equiv 2\mathcal{F}_{\rm tot}/N_{\rm seg}$. Four curves in this figure correspond to different false dismissal probabilities for the Gaussian noise, $p_{\rm FD} = 10^{-1}, 10^{-2}, 10^{-3}$, and 10^{-4}, respectively. The threshold weakly depends on $\overline{2\mathcal{F}}$ because the variance of $\bar{\chi}^2$ is related to the kurtosis of $\mathcal{F}_{\rm tot}$ in Eq. (5.24b). As opposed to [144], the threshold decreases as the expected SNR becomes large. This fact indicates that more significant lines are rejected more easily. The right panel of Fig. 5.1 shows the threshold of χ^2 as a function of $p_{\rm FD}$ for different values of $\overline{2\mathcal{F}}$.

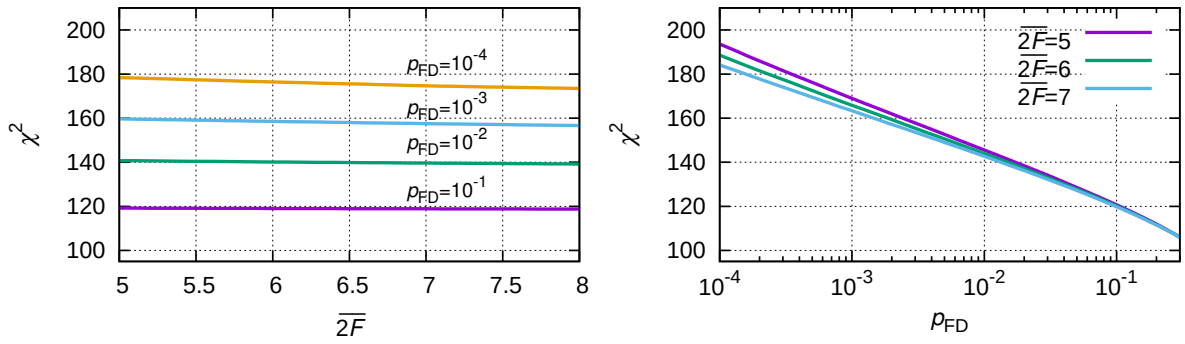

Figure 5.1: Left panel: Threshold of χ^2 as a function of $\overline{2\mathcal{F}}$ in the case of $N_{\rm seg} = 100$. Four curves correspond to different false dismissal probabilities for the Gaussian noise, $p_{\rm FD} = 10^{-1}, 10^{-2}, 10^{-3}$, and 10^{-4}, respectively. If a signal candidate exceeds the corresponding threshold for a given $p_{\rm FD}$, it should be regarded as an outlier. Right panel: The threshold of χ^2 as a function of $p_{\rm FD}$ in the case of $N_{\rm seg} = 100$. Three curves correspond to $\overline{2\mathcal{F}} = 5, 6$, and 7, respectively.

5.3.3 Validation

To see whether or not χ^2 discriminator works effectively, we generate Gaussian noise background and inject CW-like lines into N_L segments among the whole segments using the MAKEFAKEDATA_V4 code in the LAL. The amplitudes of the injected lines are set such that $\overline{2\mathcal{F}}$ ranges between 5 and 10 uniformly. After 10,000 injections, we obtain Fig. 5.2, where f_L is the fraction of the injected lines defined as $f_L \equiv N_L/N_{\rm seg}$. The

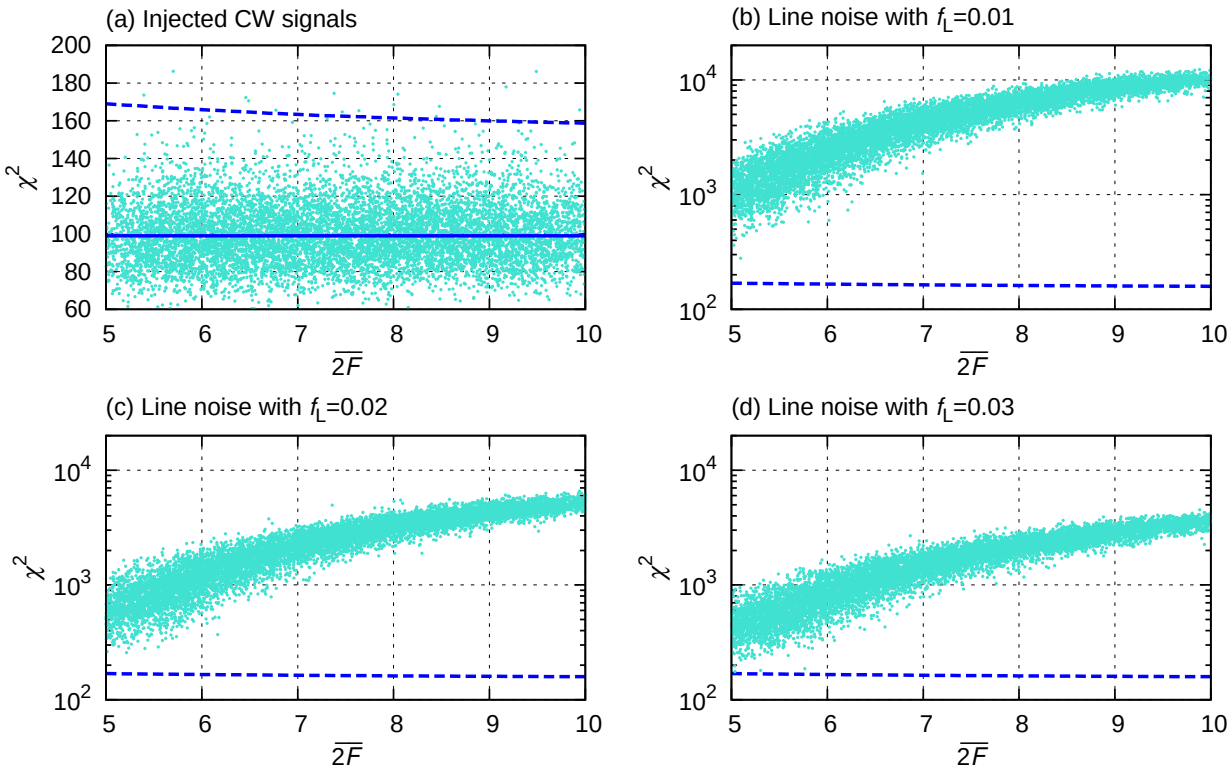

Figure 5.2: Measured values of χ^2 as a function of $\overline{2\mathcal{F}}$ for 10,000 injections into Gaussian noise background. The dotted line represents the threshold of χ^2 for $p_{\mathrm{FD}} = 1\%$. The panels (a), (b), (c), and (d) correspond to injections of CW signals, injected CW-like lines with $f_L = 0.01, 0.02$, and 0.03, respectively.

dotted line corresponds to the threshold of χ^2 for $p_{\mathrm{FD}} = 1\%$. Panel (a) in Fig. 5.2 depicts the measured values of χ^2 for each trial. As expected, the points are scattered about the solid line corresponding to Eq. (5.24a). The other panels (b), (c), and (d) in Fig. 5.2 represent the measured values of χ^2 for lines with $f_L = 1, 2$ and 3, respectively. The χ^2 values far exceed the threshold, which indicates that lines under Gaussian noise background would be vetoed easily.

Next, we perform injection tests to find detection efficiencies for the three statistics $\{\overline{2\mathcal{F}}, \overline{2\mathcal{F}}_{+\mathrm{pv}}, \overline{2\mathcal{F}}_{+\chi^2}\}$, where $\overline{2\mathcal{F}}_{+\chi^2}$ statistic is defined as a value of $\mathcal{F}$-statistic after the χ^2 veto:

$$\overline{2\mathcal{F}}_{+\chi^2} = \begin{cases} \overline{2\mathcal{F}} & \chi^2 < \chi^2_{\mathrm{thr}}\left(\overline{2\mathcal{F}}, p_{\mathrm{FD}}\right). \\ 0 & \text{otherwise.} \end{cases} \tag{5.25}$$

We inject CW signals into white Gaussian noise background using the MAKEFAKEDATA_V4 code. The injected parameters are chosen so that angular parameters $\{\alpha, \delta, \cos\iota, \psi\}$ are uniformly distributed in the range $\alpha \in [0, 2\pi]\,, \delta \in [-\pi/2, \pi/2]\,, \cos\iota \in [-1, 1]$, and $\psi \in [0, 2\pi]$. The signal frequency is assumed to obey a uniform distribution on the interval $[100, 101]$ Hz. The signal strength h_{inj} is determined so that the averaged SNR satisfies $\overline{\rho^2} = 2$. To do this, h_{inj} is set in the following way:

$$h_{\mathrm{inj}} \equiv \sqrt{\frac{\overline{2\mathcal{F}}_6 - 4}{\overline{2\mathcal{F}}_i - 4}} h_i, \tag{5.26}$$

where $\overline{2\mathcal{F}}_6 \equiv 6$ corresponds to $\overline{\rho^2} = 2$, h_i is the signal strength randomly drawn, and $\overline{2\mathcal{F}}_i$ is the measured value of $\overline{2\mathcal{F}}$[4]. We carry out 10,000 Monte-Carlo simulations for each of the values of $\overline{2\mathcal{F}}$ in the range of 4.5–7.5 with a step of 0.1. As a result, we obtain Fig. 5.3.

Figure 5.3 shows the detection efficiencies for the three detection statistics $\{\overline{2\mathcal{F}}, \overline{2\mathcal{F}}_{+\mathrm{pv}}, \overline{2\mathcal{F}}_{+\chi^2}\}$ as a funtion of the threshold $\overline{2\mathcal{F}}_{\mathrm{thr}}$. For the threshold of $\overline{2\mathcal{F}}_{+\chi^2}$, the false alarm probability is set to be 1% in this injection test. If the measured values of $\overline{2\mathcal{F}}$ exceed the threshold $\overline{2\mathcal{F}}_{\mathrm{thr}}$, signals are considered to be detected. As indicated by Fig. 5.3, the conventional $\mathcal{F}$-statistic is the most optimal detection statistic under the ideal Gaussian noise background. Our detection statistic $\overline{2\mathcal{F}}_{+\chi^2}$ overlaps with the $\mathcal{F}$-statistic in Fig. 5.3. So the detection efficiencies for these two statistics are almost comparable to each other although the maximum value of the detection efficiency for $\overline{2\mathcal{F}}_{+\chi^2}$ is 99% because we take $p_{\mathrm{FD}} = 0.01$. On the other hand, $\overline{2\mathcal{F}}_{+\mathrm{pv}}$ is inferior to the other two statistics in terms of the detection efficiencies. This is because the statistic $\overline{2\mathcal{F}}_{+\mathrm{pv}}$ excludes a single coherent

[4] Note that $\langle\overline{2\mathcal{F}}\rangle = 4 + \overline{\rho^2}$.

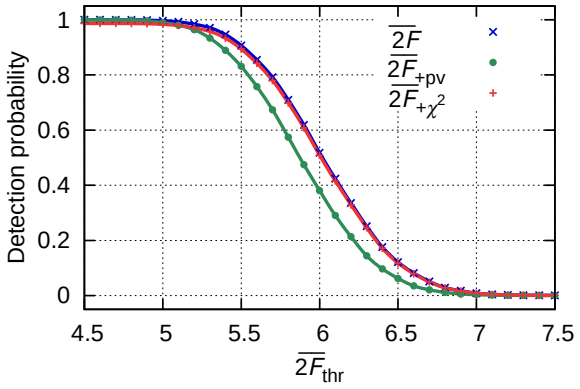

Figure 5.3: Detection probability as a function of threshold $\overline{2\mathcal{F}}_{\rm thr}$ under the ideal Gaussian noise background. Three curves represent the three detection statistics $\{\overline{2\mathcal{F}}, \overline{2\mathcal{F}}_{+\rm pv}, \overline{2\mathcal{F}}_{+\chi^2}\}$, respectively. The threshold for $\overline{2\mathcal{F}}_{+\chi^2}$ is calculated under the assumption of $p_{\rm FD} = 0.01$. For each of the statistics, if the measured value exceeds the threshold, we regard that a signal is detected. The statistics $\overline{2\mathcal{F}}$ and $\overline{2\mathcal{F}}_{+\chi^2}$ have almost the same detection efficiency while $\overline{2\mathcal{F}}_{+\rm pv}$ is interior to these two statistics.

segment containing the loudest $\mathcal{F}$-statistic value no matter whether a CW signal exists in data or not, which would lead to missing out on detectable CW signals by $\overline{2\mathcal{F}}$ and $\overline{2\mathcal{F}}_{+\chi^2}$.

5.4 The χ^2 veto in unequal SNR time-intervals

5.4.1 χ^2 discriminator

So far, we have dealt with the case of stationary noise and equal-length segments. In the following, we relax these assumptions in order to handle more realistic situations, in which case a SNR in each segment is unequal to each other. We consider the year-long observation data broken up into $N_{\rm seg}$ segments whose lengths are not necessarily equal to each other. The j-th segment is assumed to have the time length T_j and the noise spectral density S_j. Since the SNR in the j-th coherent segment is approximately proportional to $\sqrt{T_j/S_j}$ for $T_j \gtrsim 24$ hours, the variation in SNR for each coherent segment can be corrected in the following way:

$$\rho_j^2 = N_{\rm seg} w_j \overline{\rho^2}, \tag{5.27}$$

where $\overline{\rho^2}$ denotes the average SNR and w_j is defined by

$$w_j \equiv \frac{T_j}{S_j}\left[\sum_{k=1}^{N_{\rm seg}} \frac{T_k}{S_k}\right]^{-1}. \tag{5.28}$$

From this definition, $\sum_{j=1}^{N_{\rm seg}} w_j = 1$ is satisfied. It is convenient to introduce a new parameter κ_n related to w_j as

$$\kappa_n \equiv \frac{1}{N_{\rm seg}} \sum_{j=1}^{N_{\rm seg}} \left(N_{\rm seg} w_j\right)^n - 1, \tag{5.29}$$

where n is an integer. For any value of n, κ_n takes non-negative value as verified in Appendix F. The parameter κ_n takes the minimum value of zero when $w_1 = \cdots = w_n = 1/N_{\rm seg}$ which corresponds to the case of equal-SNR time intervals.

In a similar way to Sec. 5.3.1, we define χ^2 as the difference between the measured SNR and the expected SNR in each segment,

$$\chi^2 \equiv \sum_{j=1}^{N_{\rm seg}} \frac{\left|\left(2\mathcal{F}_j - 4\right) - N_{\rm seg} w_j \left(\overline{2\mathcal{F}} - 4\right)\right|^2}{w_j \sigma^2_{2\mathcal{F}_{\rm tot}}}, \tag{5.30}$$

where w_j defined by Eq. (5.28) correct the variation in SNR for each segment induced by non-stationary noises and unequal length of segment. After a similar calculation to Sec. 5.3.1, we obtain the expectation value and variance of χ^2 discriminator as

$$\langle \chi^2 \rangle = N_{\rm seg} - 1 + \frac{2N^2_{\rm seg}}{\sigma^2_{\mathcal{F}_{\rm tot}}} \kappa_{-1}, \tag{5.31a}$$

$$\sigma_{\chi^2} = \sigma_{\bar{\chi}^2} + \frac{2}{\sigma^4_{\mathcal{F}_{\rm tot}}} \left\{ 10 N^3_{\rm seg} \kappa_{-2} + 10 N^2_{\rm seg} \left(N_{\rm seg}\rho^2 - 4\right) \kappa_{-1} + \left[6\left(1 - 3\rho^2\right) + N_{\rm seg}\left(\rho^2 - 2\right)^2\right] \kappa_{+2} \right\}, \tag{5.31b}$$

where κ_{-2}, κ_{-1} and κ_{+2} are defined by Eq. (5.29). The coefficients κ_n result from a non-equality of SNRs in the coherent segments. Unlike Eq. (5.15a), $\langle \chi^2 \rangle$ depends on an observed SNR as well as $\sigma^2_{\chi^2}$.

5.4.2 Performance tests

LIGO S5 data

In this section, we conduct performance tests for a χ^2 discriminator introduced in the previous subsection using an actual data set. We analyze the initial LIGO data during the entire fifth science run (S5) that took place during about two years between November 4, 16:00 UTC 2005 and October 1, 00:00 UTC 2007 (from 815155213 to 875232014 in GPS time). The LIGO S5 data are comprised of data obtained from a three-detector network: two detectors at Hanford (H1 and H2) and one detector at Livingston (L1). So far, the S5 data have been employed to search for CWs from unknown pulsars over the whole sky by Einstein@Home that is one of volunteer projects related to distributed computing

[111, 113]. Here, we make use of the data collected from the H1 detector to validate how our veto method works in the actual data set.

We divide the S5 observation data set into 101 segments with a length of 25 hours each of which will be analyzed coherently using the $\mathcal{F}$-statistic. Each coherent segment is not necessarily contiguous but are within the range of 40 hours. Each segment is divided into shorter segment of 1,800 seconds, high-pass filtered at 40 Hz, windowed by a Tukey window, and followed by computing short-time-baseline Fourier transforms (SFTs). This process gives rise to 5,686 SFT segments.

Template placement and searched frequency band

We employ HierarchSearchGCT code [138, 139] to produce the $\mathcal{F}$-statistic from each coherent segment. The grid spacings are constructed so that the single-dimension metric mismatch is equal to 0.03. For simplicity, we make use of templates laid out on a rectangle grid that are related to the length of coherent segments, the single-dimensional mismatch, and the frequency by

$$\Delta f = \frac{\sqrt{12m}}{\pi T_{\mathrm{coh}}} \simeq 1.33 \times 10^{-6}\ \ [\mathrm{Hz}] \left(\frac{m}{0.03}\right)^{1/2} \left(\frac{40\ \mathrm{h}}{T_{\mathrm{coh}}}\right), \tag{5.32a}$$

$$\Delta \dot{f} = \frac{\sqrt{720m}}{\pi T_{\mathrm{coh}}^2} \simeq 7.13 \times 10^{-11}\ \ [\mathrm{Hz/s}] \left(\frac{m}{0.03}\right)^{1/2} \left(\frac{40\ \mathrm{h}}{T_{\mathrm{coh}}}\right)^2, \tag{5.32b}$$

$$\Delta\alpha = \Delta\delta = \frac{\sqrt{2m}}{\pi f \tau_{\mathrm{E}} \cos\delta_D} \simeq 0.101\ \ [\mathrm{rad}] \left(\frac{m}{0.03}\right)^{1/2} \left(\frac{53\ \mathrm{Hz}}{f}\right), \tag{5.32c}$$

where δ_D is the detector latitude, $\tau_{\mathrm{E}} \equiv R_{\mathrm{E}}/c$ is the travel time of light from the Earth center to the detector, and m is the single-dimensional mismatch. To reduce the computational costs, the spin-down parameters $\{\dot{f}, \ddot{f}, \cdots\}$ are not searched over in our analysis for simplicity. Hence, the spacing of frequency bins is set to be $\Delta f \simeq 1.3 \times 10^{-6}$ Hz. The spacings of the sky positions are $\Delta\alpha = \Delta\delta \simeq 0.10\,(53\ \mathrm{Hz}/f)$ radians.

We take the following four narrow frequency band of bandwidth 0.01 Hz as representative examples to calculate detection efficiency of the χ^2 statistics. The two out of the four bands are noisy bands with multiple lines whereas the remaining two are quiet bands obeying an almost Gaussian distribution:

(A) a noisy frequency band with multiple lines $f \in [52.47, 52.48]$ Hz.

(B) a noisy frequency band with multiple lines $f \in [58.60, 58.61]$ Hz.

(C) a quiet frequency band following almost Gaussian distribution $f \in [54.87, 54.88]$ Hz.

(D) a quiet frequency band following almost Gaussian distribution $f \in [58.10, 58.11]$ Hz.

Figure 5.4 depicts noise weghts w_j defined by Eq. (5.28) for these four frequency bands. The values of w_j vary by a factor of a few. In the case of equal-SNR time intervals, the weights w_j are expected to be $1/N_{\rm seg} \simeq 0.01$ and indicated by the dotted lines in Fig. 5.4.

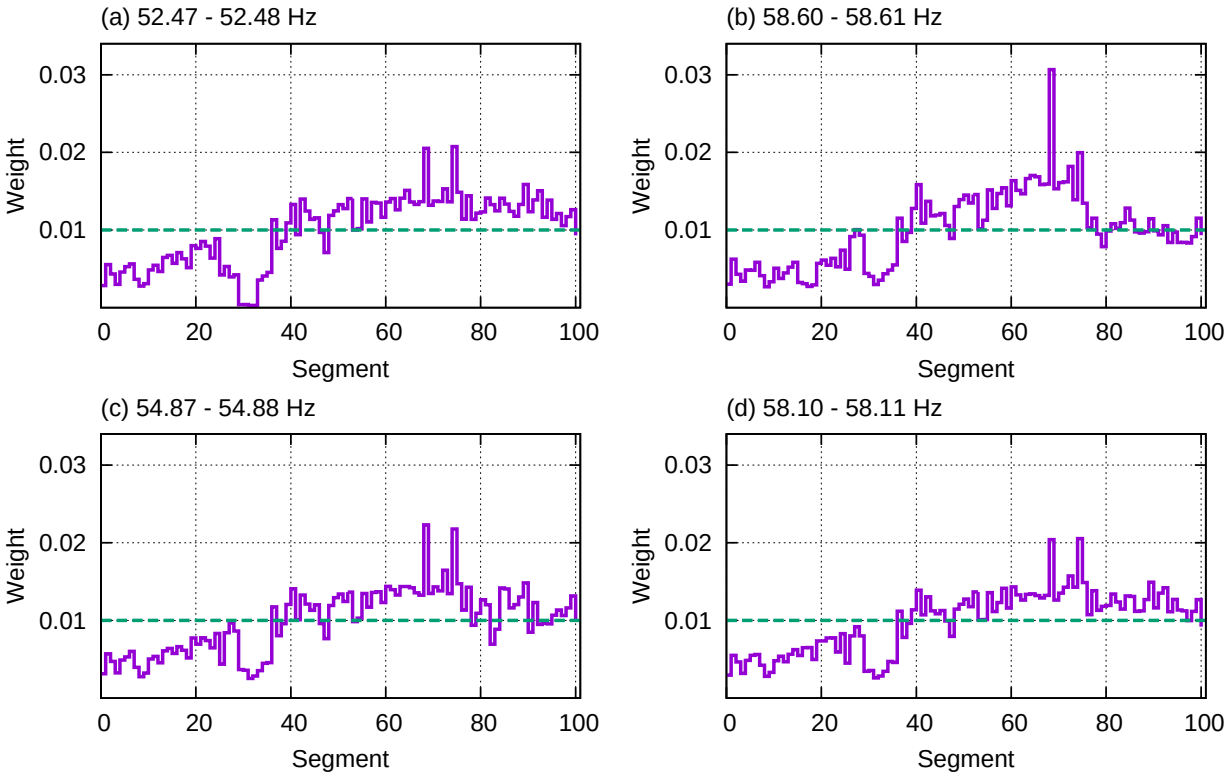

Figure 5.4: Time evolution of weights defined by Eq. (5.28) for the four frequency bands. In the case of equal-SNR time intervals, values of weights w_j are expected to be about 0.01 and agree with dotted lines.

Detection threshold for each detection statistic

In the previous section, we find the threshold for χ^2 statistic by injecting CW signals into generated white Gaussian noise. Instead of the simulated data, we inject CW signals into the LIGO S5 data by the MAKEFAKEDATA_V4 code to obtain the threshold for the χ^2 veto. The signal parameters $\{f, \alpha, \delta, \cos\iota, \psi\}$ are chosen randomly within the frequency band under the assumption that these parameters follow uniform distributions. We carry out 10,000 Monte-Carlo simulations for each of the $\overline{2\mathcal{F}}$ values in the range of 5–11 with a step of 1. The $\overline{2\mathcal{F}}$ values are calculated for perfectly matched templates. The threshold for the χ^2 statistic is chosen so that the probability that injected signals are overlooked by mistake is 5%.

First, we carry out an all-sky search for each frequency band without CW injections. The total number of templates is $N_{\rm temp} \simeq 1.5 \times 10^7$ because $N_{\rm freq} \simeq 0.01$ Hz$/\Delta f \simeq$

7.5×10^3 and $N_{\rm sky} \simeq 2\pi^2/(\Delta\alpha\Delta\delta) \simeq 2.0 \times 10^3$. The loudest values of the three statistics $\{\overline{2\mathcal{F}}, \overline{2\mathcal{F}}_{+\rm pv}, \overline{2\mathcal{F}}_{+\chi^2}\}$ among the whole template for each frequency band are registered for the subsequent injection tests. It is known that there are no significant signal candidates in the S5 data by virtue of the previous all-sky searches [111, 113]. So, when the values of each detection statistic of injected CW signals exceed one of the loudest noise candidate, we can regard that the injected signals are detected. In other words, we use the observed values of the detection statistics of the loudest noise candidate as the threshold for CW detections.

Figure 5.5 shows the cumulative number of noise candidates whose values of the three detection statistics $\{\overline{2\mathcal{F}}, \overline{2\mathcal{F}}_{+\rm pv}, \overline{2\mathcal{F}}_{+\chi^2}\}$ exceed $\overline{2\mathcal{F}}$. For $\overline{2\mathcal{F}}$, a huge number of noise candidates take high values in comparison with the other two detection statistics, $\overline{2\mathcal{F}}_{+\rm pv}$ and $\overline{2\mathcal{F}}_{+\chi^2}$. because the $\mathcal{F}$-statistic is apt to be affected by noise lines. In contrast, $\overline{2\mathcal{F}}_{+\rm pv}$ and $\overline{2\mathcal{F}}_{+\chi^2}$ considerably reduce the observed values of the $\mathcal{F}$-statistic by the veto processes. In the panel (a) of Fig. 5.5, our χ^2 veto rejects the noise candidates more effectively than the permanence veto. This is because there exist noise lines existing over multiple segments in the frequency range of 52.47–52.48 Hz. As a next step, we check whether the veto methods reject true CW signals or not, and then we compare detection efficiencies of $\overline{2\mathcal{F}}_{+\rm pv}$ and $\overline{2\mathcal{F}}_{+\chi^2}$-statistics.

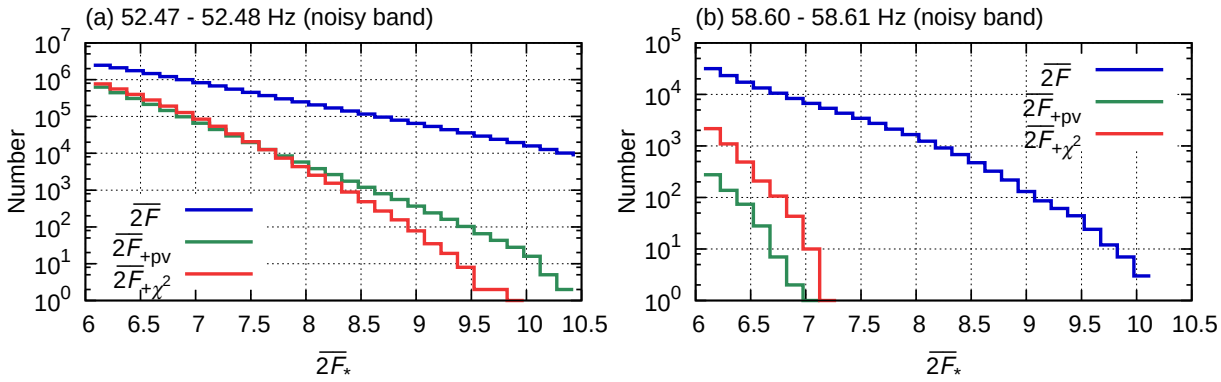

Figure 5.5: Histograms for the number of noise candidates that satisfies $\overline{2\mathcal{F}} > \overline{2\mathcal{F}}_*$ for each frequency band. The panel (a) and (b) correspond to the two noisy frequency bands.

Procedure for calculating detection efficiency

We inject CW signals into the LIGO S5 data within each frequency band using the MAKEFAKEDATA_V4 code in order to calculate the detection efficiency. The sky positions of the injected signals are assumed to be uniformly distributed over the entire sky. Also, the orientations of the sources with respect to the H1 detector are assumed to obey uniform distributions. We carry out 1,000 Monte-Carlo simulations for each of the values of $h_0/\sqrt{\overline{S_n}}$ in the range of 0.02–3.20 with a step of 0.02, where $\overline{S_n}$ denotes the strain

sensitivity averaged over the entire observation run. For each injection, a parameter space to be searched over is constructed so that a frequency range is 1 mHz band at around the signal frequency and a sky region is a sky patch consisting of 100 grid points close to the putative source position from a standpoint of the metric (see Sec. 2.5.1 for more details) [77]. For each of the statistics $\{\overline{2\mathcal{F}}, \overline{2\mathcal{F}}_{+\mathrm{pv}}, \overline{2\mathcal{F}}_{+\chi^2}\}$, if one or more signal candidates have the larger statistics than the predetermined threshold, we regard that the signals are detected.

Results

Figure 5.6 shows the detection efficiencies for the aforementioned four frequency band (A), (B), (C), and (D). Unlike Fig. 5.3, the horizontal axis is shown in units of normalized amplitude $h_0/\sqrt{\overline{S_n}}$ in place of $\overline{2\mathcal{F}}$ in order to easily relate to physical quantities. The normalization factor $\overline{S_n}$ denotes the one-sided spectral density of the S5 data averaged over the whole segments. In each panel, the blue, green, and red lines correspond to the detection statistics $\overline{2\mathcal{F}}, \overline{2\mathcal{F}}_{+\mathrm{pv}}$, and $\overline{2\mathcal{F}}_{+\chi^2}$, respectively.

The panels (a) and (b) of Fig. 5.6 correspond to the two noisy frequency bands (A) and (B), respectively. These panels indicate that the conventional $\mathcal{F}$-statistic has much worse efficiency than the other two statistics in noisy bands because the $\mathcal{F}$-statistic is susceptible to lines, which results in a high false alarm rate. Meanwhile, the newly proposed detection statistic $\overline{2\mathcal{F}}_{+\chi^2}$ has the best detection efficiency in these noisy bands. In particular, $\overline{2\mathcal{F}}_{+\chi^2}$ in the panel (a) works more powerfully than the panel (b). This feature can be traced to the number of lines existing in coherent segments. Whereas $\overline{2\mathcal{F}}_{+\mathrm{pv}}$ can only exclude lines in a signle coherent segment, $\overline{2\mathcal{F}}_{+\chi^2}$ can deal with lines existing over multiple coherent segments. For example, in the panel (a) of Fig. 5.6, the detection probabilities of $\overline{2\mathcal{F}}$, $\overline{2\mathcal{F}}_{+\mathrm{pv}}$, and $\overline{2\mathcal{F}}_{+\chi^2}$ for $h_0/\sqrt{\overline{S_n}} = 0.1$ are 17.5%, 27.8%, and 43.0%, respectively. This indicates that the χ^2 veto process rejects strong noise lines but retains injected CW signals. Thus, the $\mathcal{F}_{+\chi^2}$-statistic more easily detects CW signals buried in noisy data. The panels (c) and (d) of Fig. 5.6 correspond to the two quiet frequency bands (C) and (D), respectively. As can be seen these panels, detection powers of the three detection statistics are almost comparable to each other. In the panel (d), $\overline{2\mathcal{F}}$ are slightly better than the other two statistics because noise in this frequency band approximately obey Gaussian distributions, in which case the $\overline{2\mathcal{F}}$ is the best statistic as in Fig. 5.3.

We also constraint on GW strain amplitudes when the detection thresholds are set by using the loudest noise candidates[5]. From Fig. 5.6, upper limits on $h_0/\sqrt{\overline{S_n}}$ with a 95% confidence level for $\overline{2\mathcal{F}}, \overline{2\mathcal{F}}_{+\mathrm{pv}}$, and $\overline{2\mathcal{F}}_{+\chi^2}$ are 0.27, 0.25, and 0.20 in noisy frequency bands of 52.47–52.48 Hz, respectively. These upper limits can be more physically interpreted in

[5] In a wide-parameter-space search, a detection threshold is usually limited by a computer's memory so that significant signal candidates are registered.

terms of upper limits on the ellipticity ε using Eq. (2.11b) for a fixed distance to the source. If a NS is located at a distance of 0.1 kpc, upper limits on ε are $2.79 \times 10^{-3}, 2.58 \times 10^{-3}$, and 2.04×10^{-3}, respectively.

Label	f (Hz)	$\sqrt{\overline{S_n}}$ ($\mathrm{Hz}^{-1/2}$)	max $\overline{2\mathcal{F}}$	max $\overline{2\mathcal{F}}_{+\mathrm{pv}}$	max $\overline{2\mathcal{F}}_{+\chi^2}$
(A)	52.47–52.48	2.96×10^{-22}	14.38	10.43	9.79
(B)	58.60–58.61	1.89×10^{-22}	10.03	6.99	7.20
(C)	54.87–54.88	2.01×10^{-22}	6.12	5.73	6.12
(D)	58.10–58.11	1.70×10^{-22}	6.15	5.72	6.15

Table 5.1: Analyzed frequency bands for performance tests of detection statistics using the LIGO S5 data. Labels (A) and (B) correspond to two noisy frequency bands, whereas labels (C) and (D) correspond to two quiet frequency bands. The column labeled $\sqrt{\overline{S_n}}$ represents the strain sensitivity averaged over the whole segments. The detection statistics $\overline{2\mathcal{F}}, \overline{2\mathcal{F}}_{+\mathrm{pv}}$, and $\overline{2\mathcal{F}}_{+\chi^2}$ are defined as Eqs. (5.4), (5.8a), and (5.25), respectively. The highest values of the detection statistics $\overline{2\mathcal{F}}, \overline{2\mathcal{F}}_{+\mathrm{pv}}, \overline{2\mathcal{F}}_{+\chi^2}$ without injections are denoted by max $\overline{2\mathcal{F}}$, max $\overline{2\mathcal{F}}_{+\mathrm{pv}}$, max $\overline{2\mathcal{F}}_{+\chi^2}$, respectively, which are used as detection thresholds in Fig. 5.6.

5.5 Conclusion and discussion

In this chapter, we proposed the χ^2 veto for semi-coherent $\mathcal{F}$-statistic-based search, focusing on the SNR consistency across the different segments. Non-Gaussian narrow-band disturbances, or lines frequently appear in detector data and can mimic CW signals. Lines would produce a high false alarm rate and degrade a detection efficiency of $\overline{2\mathcal{F}}$ if no veto method is applied. The newly proposed χ^2 veto is designed to check whether or not an observed SNR accumulates in a way that is consistent with a CW signal. As opposed to the currently existing veto methods introduced in Sec. 5.2, the χ^2 veto can deal with multiple lines existing over two or more segments in a single detector and coincident lines in a multi-detector network. We investigated the performance of the χ^2 veto using the LIGO S5 data. We found that the $\overline{2\mathcal{F}}$ values after the χ^2 veto process are reduced drastically in the noisy frequency bands as shown in Fig. 5.5. Also, we tested its detection power in order to check to what extent the χ^2 veto does not miss out on detectable CW signals. Figure 5.6 indicates that the χ^2 veto process improves the detection efficiency in the noisy frequency bands in comparison with the other two detection statistics. This is due to the fact that the χ^2 veto process excludes strong noise lines but retains injected CW signals.

It should be noted that our veto method would miss out on detectable transient CWs that are CWs of duration of the order of hours–weeks. Such transient CWs are considered

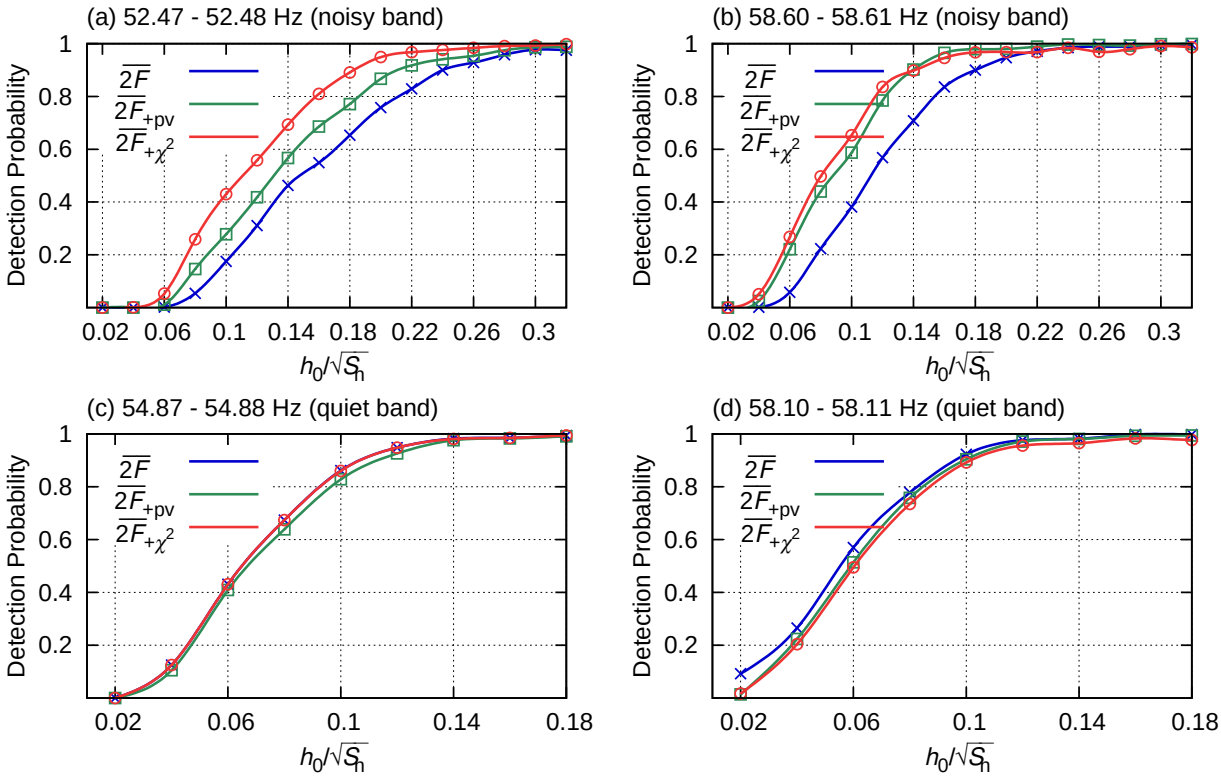

Figure 5.6: Detection probability as a function of normalized amplitude $h_0/\sqrt{\overline{S}_n}$ for each frequency band, where $\sqrt{\overline{S}_n}$ denotes the average strain sensitivity over the whole segments. The panels (a) and (b) correspond to the two noisy frequency bands, whereas the panels (c) and (d) correspond to the two quiet frequency bands. The detection statistics $\overline{2\mathcal{F}}$, $\overline{2\mathcal{F}}_{+\mathrm{pv}}$, and $\overline{2\mathcal{F}}_{+\chi^2}$ are defined as Eqs. (5.4), (5.8a), and (5.25), respectively.

to be potentially produced from magnetar giant flares [148], glitching NSs [149], and maybe wobbling NSs [35]. Since our veto method checks SNR-consistency across the whole segments of the order of a year, these transient CWs would be excluded from signal candidates. However, several search methods specific to them have been proposed by several authors [150, 143].

As future prospects, it would be interesting to extend the χ^2 veto to a multi-detector network case. The currently used veto method, the line-robust statistic requires two or more detectors because in its framework line is defined as a narrow-band disturbance appearing only in a single detector. So, this method cannot deal with coinsident lines. In fact, in the past $\mathcal{F}$-statistic-based semi-coherent search [113], 0.46% of final high-significant signal candidates passed the consistency check between a multi-detector network, and so are considered to arise from coincident lines [143]. Furthermore, when we use line-robust statistic as a veto method, detection sensitivity would be strongly limited by duty cycles of detectors that are the fraction of available data during the entire observation run. For example, let us consider two-detector network whose duty cycles are assumed to be $r_1 = r_2 = 50\%$ (For LIGO S6 run, the duty cycles of H1 and L1 detectors are 50.6% and 47.9%, respectively [14]). In this case, the line-robust statistic makes use of only $r_1 r_2 = 25\%$ data on average. In contrast, the χ^2 veto is applicable to a single-detector and so can use $(r_1 + r_2)/2 = 50\%$ data on average. Hence, semi-coherent search based on the χ^2 veto may potentially improve detection power by a few factors.

Chapter 6

Conclusion

In this thesis, we studied CWs from compact stars with a focus on data analysis using actual data set. The main source of CW signals are a rapidly spinning NSs and there exist so many uncertainties of NS physics related to equation-of-state of NSs such as maximum possible value of ellipticity, wobbling motions of NSs, generation mechanism of CWs, and relation between EM and CW emissions. CW search is expected to give new insights into these unclear issues.

In Chapter 2, we summarized CW sources, emission mechanisms, and a link between NS's equation-of-state and its ellipticity. Then, we gave an overview on data analysis tools for CW search that we need in the subsequent three chapters.

Chapter 3 is concerned with low-frequency CWs that have not been investigated due to seismic noise by the currently existing ground-based laser-interferometric GW detectors. To search for unexplored low-frequency regions below 10 Hz, we employed a recently proposed TOBA detector. TOBA is a low-frequency terrestrial GW detector consisting of two orthogonal bar-shaped test masses. Recently, multi-output configuration of TOBA has been proposed in [18], which leads to three independent output signals from a single detector. We give a short review of its figure-of-merits in terms of parameter estimation accuracies including short updates. Then, we moved on to an all-sky search for low-frequency CWs using the Phase-II TOBA that is a prototype detector of the multi-output TOBA. While data obtained from bar rotations on yz and zx planes were not incorporated in our analysis because of their worse sensitivities, we succeeded in setting the most stringent upper limits on GW strain amplitudes with confidence level 95% as 3.6×10^{-12} within 6–7 Hz frequency band.

Chapter 4 focused on KAGRA that is the first Japanese km-scale interferometric GW detector. The iKAGRA test run was conducted during three weeks in March and April in 2016, and now KAGRA is being upgraded toward its full configuration with a cryogenic Fabry-Perot laser interferometer. We performed a targeted CW search for known isolated pulsars using the iKAGRA data. The motivation of this study is to validate the search pipeline, to find program-related problems at the early stage, and to gain experiences to analyze actual data toward the full configuration operation. We investigated CW signals from 63 known isolated pulsars within 50–1,000 Hz frequency band. No significant

signal candidates were found. The upper limits on the GW strain amplitudes with 95% confidence level are of the order of 10^{-18} that are consistent with the upper limits theoretically calculated from noise level of the iKAGRA. We confirmed that our search pipeline correctly operates as expected.

In Chapter 5, we presented a χ^2 veto method for $\mathcal{F}$-statistic-based semi-coherent search for unknown CW sources in order to deal with sharp spectral noise lines that frequently hampers detection sensitivity to CW signals. Our veto method is designed to check whether or not an observed SNR accumulates as expected in the case of true CW signals. Its unique feature is the applicability to multiple lines existing over two or more coherent segments in a single detector and coincident lines in a multi-detector network. After its formulation, we conducted its performance tests using data from the LIGO Hanford detector during the S5 observation run. We found that our veto method successfully rejects noise lines. Consequently, detection probabilities for unknown CW signals in noisy frequency bands are significantly improved before and after our veto process (e.g., the detection probabilities are 17.5% for the pure $\mathcal{F}$-statistic and 43.0% for the $\mathcal{F}$-statistic after our veto process at $h_0/\sqrt{\overline{S_n}} = 0.1$ in 52.47–52.48 Hz frequency band). As a future work, our veto method will be extended to a multi-detector network.

KAGRA plans to start its observation run with the full configuration within a few years. Since KAGRA is being constructed in underground to mitigate seismic noise, it is expected to have an advantage in lower-frequency regions compared with the other large-scale ground-based interferometric detectors. As discussed in Chapter 4, KAGRA will surpass spin-down limits for about 50 known isolated pulsars in these regions, which indicates that we will be close to detections of CW signals. Also, a wide-parameter-space search for unknown CW sources in low-frequency region inaccessible by the other ground-based detectors will be conducted only by KAGRA, in which case the χ^2 veto method introduced in Chapter 5 would play important roles in rejecting unpredictable noise lines and improving the detection efficiency of CWs. KAGRA has enough chance of the first detection of a CW source, which would shed light on unclear aspects of NS physics.

Appendix A

PDF for Gaussian noise

On the assumption of stationarity and the Gaussianity for detector noise, the correlation between the different Fourier components of the noise is written as

$$\langle \tilde{n}(f)\, \tilde{n}^*(f') \rangle = \frac{1}{2}\delta(f - f')\, S_n(f), \tag{A.1}$$

where T denotes the observation time and $S_n(f)$ is called the one-sided noise spectral density. The discrete version of Eq. (A.1) is

$$\langle \tilde{n}_k \tilde{n}^*_{k'} \rangle = \frac{T}{2}\delta_{kk'} S_{n,k}, \tag{A.2}$$

where the index k corresponds to f_k[1]. Because both the real and imaginary part of $\tilde{n}_k$, $\tilde{n}_{k,r}$ and $\tilde{n}_{k,i}$ obey the same Gaussian distribution, their expection value and variance are

$$\langle \tilde{n}_{k,r} \rangle = \langle \tilde{n}_{k,i} \rangle = 0, \tag{A.4a}$$

$$\langle \tilde{n}^2_{k,r} \rangle = \langle \tilde{n}^2_{k,i} \rangle = \frac{T}{4} S_{n,k}, \tag{A.4b}$$

where we used $|\tilde{n}_k|^2 = \tilde{n}^2_{k,r} + \tilde{n}^2_{k,i}$ and Eq. (A.2). The PDF for the detector noise in Fourier space obeys

$$\begin{aligned} p(\tilde{n}_k) &= p(\tilde{n}_{k,r}, \tilde{n}_{k,i}) = p(\tilde{n}_{k,r})\, p(\tilde{n}_{k,i}) \\ &\propto \exp\left[-\frac{\tilde{n}^2_{k,r}}{2\sigma^2_{n_k}}\right] \exp\left[-\frac{\tilde{n}^2_{k,i}}{2\sigma^2_{n_k}}\right] \\ &= \exp\left[-\frac{|\tilde{n}(f_k)|^2}{2\sigma^2_{n_k}}\right], \end{aligned} \tag{A.5}$$

[1] We made use of the following approximation.

$$\delta(f) \simeq \int_{-T/2}^{T/2} e^{-2\pi i f t} dt = T\frac{\sin(\pi f T)}{\pi f T} \underset{f\to 0}{\longrightarrow} T. \tag{A.3}$$

where $\sigma_{n_k}^2 \equiv TS_{n,k}/4$. Using the above equation, we obtain the PDF for the detector noise as

$$\begin{aligned} p\left(n\right) &\propto \prod_{k=0}^{N/2} \exp\left[-\frac{\left|\tilde{n}_k\right|^2}{2\sigma_{n_k}^2}\right] = \exp\left[-\frac{1}{2}\sum_{k=0}^{N/2}\frac{4\left|\tilde{n}_k\right|^2}{TS_{n,k}}\right] \\ &= \exp\left[-\frac{1}{2}\times 4\frac{f_{\rm Nyq}}{N/2}\sum_{k=0}^{N/2}\frac{\left|\tilde{n}_k\right|^2}{S_{n,k}}\right] = \exp\left[-\frac{1}{2}\times 4\int_0^{f_{\rm Nyq}}\frac{\left|\tilde{n}\left(f\right)\right|^2}{S_n\left(f\right)}df\right] \\ &\simeq \exp\left[-\frac{1}{2}\times 4\int_0^{\infty}\frac{\left|\tilde{n}\left(f\right)\right|^2}{S_n\left(f\right)}df\right] = \exp\left[-\frac{1}{2}\left(n|n\right)\right], \end{aligned} \tag{A.6}$$

where $f_{\rm Nyq} = N/2T$ is the Nyquist frequency.

Appendix B

Statistical properties of $\mathcal{F}$-statistic

B.1 Moment-generating function

In general, random variables are statistically characterized by probability distribution functions (PDF). Also, their statistical properties can be described by moment-generating functions (MGF) which have exactly the same information as the distribution functions in many cases. MGF of a random variable X is defined as

$$M_X(\theta) \equiv E\left[e^{\theta X}\right], \tag{B.1}$$

where $E[X]$ denotes the expectation value of X. As the name implies, the MGF generates the moments of X as

$$E[X^n] = \frac{d^n M_X(\theta)}{d\theta^n}\Big|_{\theta=0}. \tag{B.2}$$

Also, there exists another useful propertity such that a MGF of a linear combination of random variables X and Y is a product of the MGF of X and Y:

$$M_{X+Y}(\theta) = M_X(\theta) M_Y(\theta). \tag{B.3}$$

For example, let us consider a random variable S_N representing a linear combination of N random variables X_i $(i = 1, \cdots, N)$ each of which follows a non-central χ^2 distribution with k_i degrees of freedom and non-centrality λ_i; $S_N = X_1 + X_2 + \cdots + X_N$. The MGF of each X_i is expressed as

$$M_{X_i}(\theta; k_i, \lambda_i) = \frac{e^{\lambda_i \theta/(1-2\theta)}}{(1-2\theta)^{k_i/2}}. \tag{B.4}$$

The combination of Eqs. (B.3) and (B.4) gives rise to the MGF of S_N as

$$\begin{aligned} M_{S_N}(\theta) &= M_{X_1}(\theta; k_1, \lambda_1) M_{X_2}(\theta; k_2, \lambda_2) \cdots M_{X_N}(\theta; k_N, \lambda_N) \\ &= \frac{e^{\lambda_1 \theta/(1-2\theta)}}{(1-2\theta)^{k_1/2}} \frac{e^{\lambda_2 \theta/(1-2\theta)}}{(1-2\theta)^{k_2/2}} \cdots \frac{e^{\lambda_N \theta/(1-2\theta)}}{(1-2\theta)^{k_N/2}} \end{aligned}$$

$$= \frac{e^{\Lambda_N \theta/(1-2\theta)}}{(1-2\theta)^{K_N/2}}. \tag{B.5}$$

Because of one-to-one coresopndence between the PDF and the MGF, the random variable S_N obeys the non-central χ^2 distribution with $K_N = k_1 + \cdots + k_N$ degrees of freedom and non-centrality $\Lambda_N = \lambda_1 + \cdots + \lambda_N$.

B.2 Statistical properties of $\mathcal{F}$-statistic

Let X be a random variable distributed according to a non-central χ^2 distribution with $k > 0$ degrees of freedom and a non-centrality parameter ρ^2. The first few moments for X are given by

$$\langle X \rangle = k + \rho^2, \tag{B.6a}$$

$$\sigma_X^2 = 2\left(k + 2\rho^2\right), \tag{B.6b}$$

$$\gamma_X = \frac{2^{3/2}\left(k + 3\rho^2\right)}{\left(k + 2\rho^2\right)^{3/2}}, \tag{B.6c}$$

$$\beta_X = \frac{12\left(k + 4\rho^2\right)}{\left(k + 2\rho^2\right)^2}, \tag{B.6d}$$

where $\langle X \rangle, \sigma_X^2, \gamma_X$, and β_X denote the mean, variance, skewness, and excess kurtosis for X, respectively. In the presence of a CW signal, $2\mathcal{F}_j$ and $2\mathcal{F}_{\text{tot}}$ obey non-central χ^2 distributions with 4 and $4N$ degrees of freedom and non-centralities ρ_j^2 and ρ_{tot}^2, respectively. So, Eqs. (B.6a)–(B.6d) can be applied to $2\mathcal{F}_i$ and $2\mathcal{F}_{\text{tot}}$ after appropriately replacing k and ρ^2 with the corresponding values. In the absence of a CW signal, $2\mathcal{F}_j$ and $2\mathcal{F}_{\text{tot}}$ obey χ^2 distributions with 4 and $4N$ degrees of freedom. This is a special case of the non-central χ^2 distribution with $\rho_j^2 = 0$ and $\rho_{\text{tot}}^2 = 0$.

Appendix C

Antenna pattern function

C.1 Definition

An incident GW is described as a tensorial quantity h_{jk}, while an observed quantity by a GW detector is a scalar quantity h. The GW signal h is related to h_{jk} by a detector tensor D^{jk} that contains geometrical information such as location of the detector on the Earth and direction of the detector with respect to the GW source. Under the assumption of the long wavelength limit $\hat{\boldsymbol{N}} \cdot \boldsymbol{x}/\lambda \ll 1$, a GW wavefrom is described by

$$\begin{aligned} h_{jk}(t, \boldsymbol{x}) &= \int_{-\infty}^{\infty} df\ \tilde{h}_{jk}(f)\, e^{-2\pi i f\left(t - \hat{\boldsymbol{N}}\cdot\boldsymbol{x}/c\right)} \\ &= \sum_{A=+,\times} e^{A}_{jk}(\hat{\boldsymbol{N}}) \int_{-\infty}^{\infty} df\ \tilde{h}_{A}(f)\, e^{-2\pi i f\left(t - \hat{\boldsymbol{N}}\cdot\boldsymbol{x}/c\right)} \\ &\simeq \sum_{A=+,\times} e^{A}_{jk}(\hat{\boldsymbol{N}}) \int_{-\infty}^{\infty} df\ \tilde{h}_{A}(f)\, e^{-2\pi i f t} \\ &= \sum_{A=+,\times} e^{A}_{jk}(\hat{\boldsymbol{N}}) h_{A}(t)\,, \end{aligned} \tag{C.1}$$

where $h_A(t)$, $\hat{\boldsymbol{N}}$, e^A_{jk} denote the GW strain at the coordinate origin $\boldsymbol{x} = \boldsymbol{0}$, the unit vector of the direction of the incoming GW, and the polarization tensor, respectively. The index A stands for two polarization mode, cross mode and plus mode. The waveform $h_{jk}(t, \boldsymbol{x})$ is converted into the GW signal h by the detector tensor D^{jk} as follows:

$$\begin{aligned} h(t) &\equiv D^{jk}(t)\, h_{jk}(t) \\ &= \sum_{A=+,\times} D^{jk}(t)\, e^{A}_{jk}(\hat{\boldsymbol{N}}) h_{A}(t) \\ &= \sum_{A=+,\times} F_{A}(t, \hat{\boldsymbol{N}}) h_{A}(t)\,, \end{aligned} \tag{C.2}$$

where F_A are often referred to as antenna pattern functions and are defined as

$$F_{+,\times}(t, \hat{\boldsymbol{N}}) \equiv D^{jk}(t)\, e^{+,\times}_{jk}(\hat{\boldsymbol{N}}). \tag{C.3}$$

The pattern functions F_A represent to the response of the detector to the two independent polarization modes of GW.

C.2 Concrete expressions for antenna pattern functions

The response of a GW detector to an incoming GW depends on its relative position and orientation to the GW source. Such a geometrical information on the detector and the sources is encoded in the antenna-pattern functions $F_{+,\times}$. Since the relative motion of the detector with respect to the sources is negligible for short-duration signals, $F_{+,\times}$ can be regarded as a constant. On the other hand, for long-duration signals the detector and the source cannot be regarded as at rest with respect to each other because of the Earth's rotation and revolution. These relative motions induce the amplitude-modulation and phase-modulation of the signal. To take into account these effects, we follow the formulation presented by Jaranowski, Królak and Schutz [57]. The GW waveform $h(t)$ in the proper antenna frame where the two bars are alined with x-axis and y-axis respectively can be related to the waveform $h'(t)$ in the wave-coming frame by

$$h(t) = M(t)\, h'(t)\, M(t)^{\mathrm{T}}, \tag{C.4}$$

where $M(t)$ denotes a 3-dimensional transformation matrix. The matrix $M(t)$ is defined by

$$M = M_3 M_2 M_1^{\mathrm{T}}, \tag{C.5}$$

where M_1 is the transformation matrix from the wave-coming frame to celestial sphere frame, M_2 is the transformation matrix from the celestial sphere frame to the cardinal frame and M_3 is the transformation matrix from the cardinal frame to the proper antenna frame (see [31, 57] for more details). The transformation matrices M_1, M_2 and M_3 are given as follows:

$$M_1 = \begin{pmatrix} \sin\alpha\cos\psi - \cos\alpha\sin\delta\sin\psi & -\cos\alpha\cos\psi - \sin\alpha\sin\delta\sin\psi & \cos\delta\sin\psi \\ -\sin\alpha\sin\psi - \cos\alpha\sin\delta\cos\psi & \cos\alpha\sin\psi - \sin\alpha\sin\delta\cos\psi & \cos\delta\cos\psi \\ -\cos\alpha\cos\delta & -\sin\alpha\cos\delta & -\sin\alpha \end{pmatrix}, \tag{C.6a}$$

$$M_2 = \begin{pmatrix} \sin\delta_D\cos\alpha_D(t) & \sin\delta_D\sin\alpha_D(t) & -\cos\delta_D \\ -\sin\alpha_D(t) & \cos\alpha_D(t) & 0 \\ \cos\delta_D\cos\alpha_D(t) & \cos\delta_D\sin\alpha_D(t) & \sin\delta_D \end{pmatrix}, \tag{C.6b}$$

$$M_3 = \begin{pmatrix} -\sin(\gamma - \zeta/2) & \cos(\gamma - \zeta/2) & 0 \\ -\cos(\gamma - \zeta/2) & -\sin(\gamma - \zeta/2) & 0 \\ 0 & 0 & 1 \end{pmatrix}. \tag{C.6c}$$

where α, δ, α_D, δ_D, γ, and ζ denote the right ascension, the declination, the latitude and longitude of the detector position, the angle between the local East direction and the bisector of the detector, and the angle formed by the two arms, respectively.

C.2.1 Laser interferometer

In the proper detector frame, the horizontal motions of the two end mirrors are induced by the GW tidal force. When the GW force produces the small horizontal motion of the x end mirror in the x-axis, the resulting GW response is expressed by $h_{ij}n_x^j n_x^k$. The GW signals can be read from the differential motions of the mirrors in the arms. Thus, the detector tensor of the laser interferometer is expressed by

$$D^{jk} = \frac{1}{2}\left(n_x^j n_x^k - n_y^j n_y^k\right), \tag{C.7}$$

where $\boldsymbol{n}_x$ and $\boldsymbol{n}_y$ are the unit vectors pointing toward the x and y-directions respectively in the proper detector frame. Combining Eqs. (C.2)−(C.7) yields the concrete expressions for the antenna pattern functions

$$F_+(t) = \sin\zeta\left[a(t)\cos 2\psi + b(t)\sin 2\psi\right], \tag{C.8a}$$

$$F_\times(t) = \sin\zeta\left[b(t)\cos 2\psi - a(t)\sin 2\psi\right], \tag{C.8b}$$

where modulation functions $a(t)$ and $b(t)$ are defined by

$$\begin{aligned} a(t) = {} & \frac{1}{4}\sin\gamma\left(1+\sin^2\delta_D\right)\left(1+\sin^2\delta\right)\cos\left[2\left(\alpha-\alpha_D(t)\right)\right] \\ & - \frac{1}{2}\cos 2\gamma\sin\delta_D\left(1+\sin^2\delta\right)\sin\left[2\left(\alpha-\alpha_D(t)\right)\right] \\ & + \frac{1}{4}\sin 2\gamma\sin 2\delta_D\sin 2\delta\cos\left[\alpha-\alpha_D(t)\right] \\ & - \frac{1}{2}\cos 2\gamma\cos\delta_D\sin 2\delta\sin\left[\alpha-\alpha_D(t)\right] \\ & + \frac{3}{4}\sin 2\gamma\cos^2\delta_D\cos^2\delta, \end{aligned} \tag{C.9a}$$

$$\begin{aligned} b(t) = {} & \cos 2\gamma\sin\delta_D\sin\delta\cos\left[2\left(\alpha-\alpha_D(t)\right)\right] \\ & + \frac{1}{2}\sin 2\gamma\left(1+\sin^2\delta_D\right)\sin\delta\sin\left[2\left(\alpha-\alpha_D(t)\right)\right] \\ & + \cos 2\gamma\cos\delta_D\cos\delta\cos\left[\alpha-\alpha_D(t)\right] \end{aligned}$$

$$+\frac{1}{2}\sin 2\gamma \sin 2\delta_D \cos\delta \sin\left[\alpha-\alpha_D\left(t\right)\right]. \tag{C.9b}$$

C.2.2 Multi-output TOBA

As discussed in Sec. 3.1.2, the two orthogonal bars rotate differentially by the tidal force from an incoming GW. When the tidal force produces the small rotation of the bar on the x-axis toward the y-direction, the resulting GW signal is expressed by $h_{jk}n_x^j n_y^k$. Similarly, detector tensors for the three detector outputs are expressed by

$$D_{\mathrm{I}}^{jk} = \frac{1}{2}\left(n_x^j n_y^k + n_y^j n_x^k\right) = n_x^j n_y^k, \tag{C.10a}$$

$$D_{\mathrm{II}}^{jk} = \frac{1}{2} n_x^j n_z^k, \tag{C.10b}$$

$$D_{\mathrm{III}}^{jk} = \frac{1}{2} n_y^j n_z^k. \tag{C.10c}$$

Using Eqs. (C.2)−(C.6c) and (C.10a)−(C.10c), we obtain the antenna pattern functions of the multi-output TOBA as follows:

$$F_{+,i}\left(t\right) = a_i\left(t\right)\cos 2\psi + b_i\left(t\right)\sin 2\psi, \tag{C.11a}$$

$$F_{\times,i}\left(t\right) = b_i\left(t\right)\cos 2\psi - a_i\left(t\right)\sin 2\psi, \tag{C.11b}$$

where i =I, II, III and modulation functions are given by

$$\begin{aligned}
a_{\mathrm{I}}\left(t\right) = {} & \frac{3}{4}\cos 2\gamma \cos^2\delta_D \cos^2\delta \\
& + \frac{1}{4}\cos 2\gamma \left(1+\sin^2\delta_D\right)\left(1+\sin^2\delta\right)\cos\left[2\left(\alpha-\alpha_D\left(t\right)\right)\right] \\
& + \frac{1}{4}\cos 2\gamma \sin 2\delta_D \sin 2\delta \cos\left[\alpha-\alpha_D\left(t\right)\right] \\
& + \frac{1}{2}\sin 2\gamma \cos\delta_D \sin 2\delta \sin\left[\alpha-\alpha_D\left(t\right)\right] \\
& + \frac{1}{2}\sin 2\gamma \sin\delta_D \left(1+\sin^2\delta\right)\sin\left[2\left(\alpha-\alpha_D\left(t\right)\right)\right],
\end{aligned} \tag{C.12a}$$

$$\begin{aligned}
b_{\mathrm{I}}\left(t\right) = {} & -\sin 2\gamma \cos\delta_D \cos\delta \cos\left[\alpha-\alpha_D\left(t\right)\right] \\
& - \sin 2\gamma \sin\delta_D \sin\delta \cos\left[2\left(\alpha-\alpha_D\left(t\right)\right)\right] \\
& + \frac{1}{2}\cos 2\gamma \sin 2\delta_D \cos\delta \sin\left[\alpha-\alpha_D\left(t\right)\right] \\
& + \frac{1}{2}\cos 2\gamma \left(1+\sin^2\delta_D\right)\sin\delta \sin\left[2\left(\alpha-\alpha_D\left(t\right)\right)\right],
\end{aligned} \tag{C.12b}$$

$$\begin{aligned}
a_{\mathrm{II}}\left(t\right) = {} & \frac{1}{4}\sin\left(\gamma+\frac{\pi}{4}\right)\sin\delta_D \sin 2\delta \sin\left[\alpha-\alpha_D\left(t\right)\right] \\
& - \frac{1}{4}\cos\left(\gamma+\frac{\pi}{4}\right)\cos 2\delta_D \sin 2\delta \cos\left[\alpha-\alpha_D\left(t\right)\right]
\end{aligned}$$

$$
\begin{aligned}
&+\frac{1}{8}\cos\left(\gamma+\frac{\pi}{4}\right)\sin 2\delta_D\cos 2\delta\left(1+\sin^2\left[\left(\alpha-\alpha_D\left(t\right)\right)\right]\right)\\
&+\frac{3}{8}\cos\left(\gamma+\frac{\pi}{4}\right)\sin 2\delta_D\sin^2\left[\alpha-\alpha_D\left(t\right)\right]\\
&-\frac{1}{4}\sin\left(\gamma+\frac{\pi}{4}\right)\cos\delta_D\left(1+\sin^2\delta\right)\sin\left[2\left(\alpha-\alpha_D\left(t\right)\right)\right], \qquad \text{(C.12c)}\\
b_{\mathrm{II}}\left(t\right) = &-\frac{1}{2}\sin\left(\gamma+\frac{\pi}{4}\right)\sin\delta_D\cos\delta\cos\left[\alpha-\alpha_D\left(t\right)\right]\\
&-\frac{1}{2}\cos\left(\gamma+\frac{\pi}{4}\right)\cos 2\delta_D\cos\delta\sin\left(\alpha-\alpha_D\left(t\right)\right)\\
&+\frac{1}{2}\sin\left(\gamma+\frac{\pi}{4}\right)\cos\delta_D\sin\delta\cos\left[2\left(\alpha-\alpha_D\left(t\right)\right)\right]\\
&-\frac{1}{4}\cos\left(\gamma+\frac{\pi}{4}\right)\sin 2\delta_D\sin\delta\sin\left[2\left(\alpha-\alpha_D\left(t\right)\right)\right], \qquad \text{(C.12d)}\\
a_{\mathrm{III}}\left(t\right) = &-\frac{3}{8}\sin\left(\gamma+\frac{\pi}{4}\right)\sin 2\delta_D\cos^2\delta\\
&+\frac{1}{4}\sin\left(\gamma+\frac{\pi}{4}\right)\cos 2\delta_D\sin 2\delta\cos\left[\alpha-\alpha_D\left(t\right)\right]\\
&+\frac{1}{4}\cos\left(\gamma+\frac{\pi}{4}\right)\sin\delta_D\sin 2\delta\sin\left[\alpha-\alpha_D\left(t\right)\right]\\
&+\frac{1}{8}\sin\left(\gamma+\frac{\pi}{4}\right)\sin 2\delta_D\left(1+\sin^2\delta\right)\cos\left[2\left(\alpha-\alpha_D\left(t\right)\right)\right]\\
&-\frac{1}{4}\cos\left(\gamma+\frac{\pi}{4}\right)\cos\delta_D\left(1+\sin^2\delta\right)\sin\left[2\left(\alpha-\alpha_D\left(t\right)\right)\right], \qquad \text{(C.12e)}\\
b_{\mathrm{III}}\left(t\right) = &-\frac{1}{2}\cos\left(\gamma+\frac{\pi}{4}\right)\sin\delta_D\cos\delta\cos\left[\alpha-\alpha_D\left(t\right)\right]\\
&+\frac{1}{2}\sin\left(\gamma+\frac{\pi}{4}\right)\cos 2\delta_D\cos\delta\sin\left[\alpha-\alpha_D\left(t\right)\right]\\
&+\frac{1}{2}\cos\left(\gamma+\frac{\pi}{4}\right)\cos\delta_D\sin\delta\cos\left[2\left(\alpha-\alpha_D\left(t\right)\right)\right]\\
&+\frac{1}{2}\sin\left(\gamma+\frac{\pi}{4}\right)\cos 2\delta_D\cos\delta\sin\left[\alpha-\alpha_D\left(t\right)\right]\\
&+\frac{1}{4}\sin\left(\gamma+\frac{\pi}{4}\right)\sin 2\delta_D\sin\delta\sin\left[2\left(\alpha-\alpha_D\left(t\right)\right)\right]. \qquad \text{(C.12f)}
\end{aligned}
$$

Appendix D

Fisher analysis

In this appendix, we provide a brief review of Fisher analysis to evaluate parameter estimation errors for a network of $N_{\rm det}$ detectors (see [151, 152] for more details). Each detector output $s_X(t)$ is assumed to be written as a linear sum of noise $n_X(t)$ and the GW signal $h_X(t)$, $s_X(t) = h_X(t) + n_X(t)$. If noise is stationary, the correlation between the Fourier components of the noise can be expressed by

$$\langle \tilde{n}_X(f)\, \tilde{n}_Y^*(f') \rangle = \frac{1}{2}\delta(f - f')\, S_n(f)_{XY}\,, \tag{D.1}$$

where $\langle \cdots \rangle$ denotes the ensemble average and $\boldsymbol{S}_n(f)$ is a one-sided power spectral density matrix of the detector network. It is convenient to introduce a noise-weighted inner product between $N_{\rm det}$-dimensional vector functions $\boldsymbol{f}(t)$ and $\boldsymbol{g}(t)$,

$$\left(\boldsymbol{f}\middle|\boldsymbol{g}\right) = 4{\rm Re}\sum_{X,Y=1}^{N_{\rm det}} \int_0^\infty \frac{\tilde{f}_X(f)\,\tilde{g}_Y^*(f)}{S_n(f)_{XY}} df, \tag{D.2}$$

where Re denotes the real part and $N_{\rm det}$ is the number of detectors. Using this inner product, SNR for the GW signal $\boldsymbol{h}(t)$ can be written as

$$\frac{S}{N} = \left(\boldsymbol{h}\middle|\boldsymbol{h}\right)^{1/2}. \tag{D.3}$$

We assume that the GW signal $\boldsymbol{h}(t)$ is characterized by a collection of unknown parameters $\boldsymbol{\lambda} = \{\lambda_1, \cdots, \lambda_n\}$. When the noise is Gaussian in addition to stationary, the statistical errors caused by the randomness of detector noise are estimated by

$$\langle \Delta\lambda^i \Delta\lambda^j \rangle = \left(\Gamma^{-1}\right)_{ij}, \tag{D.4}$$

for large SNR. The matrix Γ_{ij} is referred to as the Fisher information matrix

$$\Gamma_{ij} = \left(\frac{\partial \boldsymbol{h}}{\partial \lambda^i}\middle|\frac{\partial \boldsymbol{h}}{\partial \lambda^j}\right). \tag{D.5}$$

To estimate the angular resolution of the detectors, we use the error in solid angle defined by

$$\Delta\Omega \equiv 2\pi \left|\sin\delta\right| \sqrt{\langle\Delta\alpha^2\rangle\langle\Delta\delta^2\rangle - \langle\Delta\alpha\Delta\delta\rangle^2}. \tag{D.6}$$

Appendix E

Calculation of the variance of the χ^2 discriminator

In this appendix, we derive the variance of the χ^2 discriminator defined by Eq. (5.23). Since $\mathcal{F}$-statistic values of different segments are treated as independent and identically distributed random variables in the case of the equal-SNR time intervals, $\sigma^2_{\bar{\chi}^2}$ can be reduced to the following form:

$$\begin{aligned}
\sigma^2_{\bar{\chi}^2} &\equiv \langle\left(\bar{\chi}^2\right)^2\rangle - \langle\bar{\chi}^2\rangle^2 \\
&= \frac{N^2}{\sigma^4_{\mathcal{F}_{\mathrm{tot}}}}\left[\sum_{j,k=1}^{N}\langle\left(\Delta\mathcal{F}_j\right)^2\left(\Delta\mathcal{F}_k\right)^2\rangle - \left(\sum_{j=1}^{N}\langle\left(\Delta\mathcal{F}_j\right)^2\rangle\right)^2\right] \\
&= \frac{N^2}{\sigma^4_{\mathcal{F}_{\mathrm{tot}}}}\left[\sum_{j=1}^{N}\langle\left(\Delta\mathcal{F}_j\right)^4\rangle + \sum_{j=1}^{N}\sum_{k\neq j}^{N}\langle\left(\Delta\mathcal{F}_j\right)^2\left(\Delta\mathcal{F}_k\right)^2\rangle - \left(\sum_{j=1}^{N}\langle\left(\Delta\mathcal{F}_j\right)^2\rangle\right)^2\right] \\
&= \frac{N^3}{\sigma^4_{\mathcal{F}_{\mathrm{tot}}}}\left[\langle\left(\Delta\mathcal{F}_j\right)^4 - \langle\left(\Delta\mathcal{F}_j\right)^2\rangle^2\right].
\end{aligned} \tag{E.1}$$

The first term in Eq. (E.1) is decomposed into

$$\langle\left(\Delta\mathcal{F}_j\right)^4\rangle = \langle\mathcal{F}_j^4\rangle - \frac{4}{N}\underline{\langle\mathcal{F}_j^3\mathcal{F}_{\mathrm{tot}}\rangle}_{\text{ⓐ}} + \frac{6}{N^2}\underline{\langle\mathcal{F}_j^2\mathcal{F}_{\mathrm{tot}}^2\rangle}_{\text{ⓑ}} - \frac{4}{N^3}\underline{\langle\mathcal{F}_j\mathcal{F}_{\mathrm{tot}}^3\rangle}_{\text{ⓒ}} + \frac{1}{N^4}\underline{\langle\mathcal{F}_{\mathrm{tot}}^4\rangle}_{\text{ⓓ}}. \tag{E.2}$$

The four terms ⓐ, ⓑ, ⓒ, and ⓓ are calculated as

$$\text{ⓐ} = \langle\mathcal{F}_j^4\rangle + (N-1)\langle\mathcal{F}_j^3\rangle\langle\mathcal{F}_j\rangle, \tag{E.3a}$$

$$\text{ⓑ} = \langle\mathcal{F}_j^4\rangle + 2(N-1)\langle\mathcal{F}_j^3\rangle\langle\mathcal{F}_j\rangle + (N-1)\langle\mathcal{F}_j^2\rangle^2 + (N-1)(N-2)\langle\mathcal{F}_j^2\rangle\langle\mathcal{F}_j\rangle^2, \tag{E.3b}$$

$$\begin{aligned}
\text{ⓒ} = {} & \langle\mathcal{F}_j^4\rangle + 4(N-1)\langle\mathcal{F}_j^3\rangle\langle\mathcal{F}_j\rangle + 3(N-1)\langle\mathcal{F}_j^2\rangle^2 + 6(N-1)(N-2)\langle\mathcal{F}_j\rangle^2\langle\mathcal{F}_j^2\rangle^2 \\
& + (N-1)(N-2)(N-3)\langle\mathcal{F}_j\rangle^4,
\end{aligned} \tag{E.3c}$$

$$\text{ⓓ} = N^4\langle\mathcal{F}_j\rangle, \tag{E.3d}$$

where the expectation values of $\mathcal{F}_j, \mathcal{F}_j^2, \mathcal{F}_j^3$, and $\mathcal{F}_j^4$ are expressed as

$$\langle \mathcal{F}_j \rangle = 2 + \frac{1}{2}\rho_j^2, \tag{E.4a}$$

$$\langle \mathcal{F}_j^2 \rangle = 6 + 3\rho_j^2 + \frac{1}{4}\rho_j^4, \tag{E.4b}$$

$$\langle \mathcal{F}_j^3 \rangle = 24 + 18\rho_j^2 + 3\rho_j^4 + \frac{1}{8}\rho_j^6, \tag{E.4c}$$

$$\langle \mathcal{F}_j^4 \rangle = 120 + 120\rho_j^2 + 30\rho_j^4 + \frac{5}{2}\rho_j^6 + \frac{1}{16}\rho_j^8. \tag{E.4d}$$

Collecting the above results, we find the concrete expression for $\sigma_{\bar{\chi}^2}^2$ as

$$\begin{aligned}\sigma_{\bar{\chi}^2}^2 &= \frac{2N^3\,(N-1)}{\sigma_{\mathcal{F}_{\text{tot}}}^4}\left[2\left(5N^2-11N+9\right)+2\left(5N^2-11N+9\right)\rho_j^2+N\,(N-1)\,\rho_j^4\right] \\ &= \frac{N-1}{N}\left[2\,(N-1)+\left(N^2-3N+3\right)\beta_{2\mathcal{F}_{\text{tot}}}\right],\end{aligned} \tag{E.5}$$

where $\beta_{2\mathcal{F}_{\text{tot}}}$ denotes the kurtosis of $2\mathcal{F}_{\text{tot}}$ defined by Eq. (B.6d).

Appendix F

Minimum value of κ_η

We wish to find the set of $\boldsymbol{w} = \{w_1, \cdots, w_N\}$ that minimizes $\kappa_n(\boldsymbol{w})$ subject to the constraint $\sum_{j=1}^{N} w_j = 1$. According to the method of Lagrange multipliers, this can be done by using the Lagrange function,

$$\mathcal{L}(\lambda_0, \boldsymbol{w}) = \kappa_n(\boldsymbol{w}) - \lambda_0 \left(\sum_{j=1}^{N} w_j - 1 \right) \tag{F.1}$$

where $\kappa_n(\boldsymbol{w})$ is defined by Eq. (5.29) and λ_0 is a constant called the Lagrange multiplier. Setting the partial derivatives of Eq. (F.1) with respect to λ_0 and $\boldsymbol{w}$ to be zero,

$$\partial_{\lambda_0} \mathcal{L} = -\sum_{j=1}^{N} w_j + 1 = 0, \tag{F.2}$$

$$\partial_{w_j} \mathcal{L} = n (N w_j)^{n-1} - \lambda_0 = 0, \tag{F.3}$$

we obtain the critical point as $\lambda_0 = n$ and $w_1 = \cdots = w_N = 1/N$. In order to check whether this point is a local minimum or not, it is useful to introduce the bordered Hessian matrix defined by a square matrix of second-order partial derivatives of the Lagrange function (F.1),

$$H = \begin{pmatrix} \partial_{\lambda_0 w_0} \mathcal{L} & \partial_{\lambda_0 w_j} \mathcal{L} \\ \partial_{\lambda_0 w_j} \mathcal{L} & \partial_{w_j w_k} \mathcal{L} \end{pmatrix}. \tag{F.4}$$

At the critical point, the Hessian is evaluated as $\det(H) = -N^N [n(n-1)]^{N-1} < 0$ for $n \neq 0, 1$ and $N \geq 1$. Since $\mathcal{L}(\lambda_0, \boldsymbol{w})$ has a single critical point, $\kappa_n(\boldsymbol{w})$ takes the minimum value of zero at the critical point $w_1 = \cdots = w_N = 1/N$ for $n \neq 0, 1$. Since $\kappa_0 = \kappa_1 = 0$, $\kappa_n \geq 0$ is satisfied for any integer n.

Acknowledgements

First of all, I would like to express my sincere gratitude to my supervisor, Prof. Jun'ichi Yokoyama. He gave me continuous support and encouragement during my time as a graduate student. I deeply thank Prof. Yousuke Itoh for guiding me through continuous wave analysis, for exciting and fruitful discussions, and for supporting throughout my Ph.D. period.

I would like to be grateful to Prof. Masaki Ando, Dr. Ayaka Shoda, and Yuya Kuwahara for giving me an opportunity to work in the TOBA project. I was fortunate to have done a key part of the initial work on the multi-output TOBA. It has been a pleasure to have worked with many highly-qualified people in the KAGRA group. In particular, I would like to thank Prof. Nobuyuki Kanda, Prof. Hideyuki Tagoshi, Prof. Ken-ichi Oohara, Prof. Yuta Michimura, Dr. Koh Ueno, Dr. Tatsuya Narikawa, and Dr. Takaaki Yokozawa for fruit discussions.

I would also like to thank my office mates, past and present, in RESCEU with whom I have enjoyed various coffee breaks. Special thanks to Dr. Yuhei Miyamoto and Dr. Tomohiro Nakama for sharing many hilarious moments. I am grateful for support from administrative staff in RESCEU: Sayuri Nagano, Mieko Minamisawa, and Chiyo Ueda.

My research was also supported by a Grant-in-Aid from the Japan Society for the Promotion of Science (JSPS KAKENHI Grant Number JP 14J08636) throughout my Ph.D. years.

Bibliography

[1] B. P. Abbott et al. Observation of Gravitational Waves from a Binary Black Hole Merger. *Phys. Rev. Lett.*, 116(6):061102, 2016.

[2] B. P. Abbott et al. Properties of the Binary Black Hole Merger GW150914. *Phys. Rev. Lett.*, 116(24):241102, 2016.

[3] B. P. Abbott et al. GW150914: First results from the search for binary black hole coalescence with Advanced LIGO. *Phys. Rev.*, D93(12):122003, 2016.

[4] B. P. Abbott et al. GW151226: Observation of Gravitational Waves from a 22-Solar-Mass Binary Black Hole Coalescence. *Phys. Rev. Lett.*, 116(24):241103, 2016.

[5] B. S. Sathyaprakash and B. F. Schutz. Physics, Astrophysics and Cosmology with Gravitational Waves. *Living Rev. Rel.*, 12:2, 2009.

[6] J. Weber. Detection and Generation of Gravitational Waves. *Phys. Rev.*, 117:306–313, 1960.

[7] J. Weber. Evidence for discovery of gravitational radiation. *Phys. Rev. Lett.*, 22:1320–1324, 1969.

[8] M. E. Gertsenshtein and V. I. Pustovoit. On the detection of low frequency gravitational waves. *Sov. Phys. JETP*, 16:433–435, 1963.

[9] G. E. Moss, L. R. Miller, and R. L. Forward. Photon-noise-limited laser transducer for gravitational antenna. *Appl. Opt.*, 10:2495–2498, 1971.

[10] J. Aasi et al. Advanced LIGO. *Class. Quant. Grav.*, 32:074001, 2015.

[11] F. Acernese et al. Advanced Virgo: a second-generation interferometric gravitational wave detector. *Class. Quant. Grav.*, 32(2):024001, 2015.

[12] Yoichi Aso et al. Interferometer design of the KAGRA gravitational wave detector. *Phys.Rev.*, D88(4):043007, 2013.

[13] Baba Iyer et al. LIGO-India Technical Report No. LIGO-M1100296. https://dcc.ligo.org/LIGO-M1100296/public/main, 2011.

[14] J. Aasi et al. Gravitational waves from known pulsars: results from the initial detector era. *Astrophys. J.*, 785:119, 2014.

[15] R N Manchester, G B Hobbs, A Teoh, and M Hobbs. The Australia Telescope National Facility pulsar catalogue. *Astron. J.*, 129:1993, 2005.

[16] Ramesh Narayan. The birthrate and initial spin period of single radio pulsars. *Astrophys. J.*, 319:162–179, 1987.

[17] Kazunari Eda, Ayaka Shoda, Yousuke Itoh, and Masaki Ando. Improving parameter estimation accuracy with torsion-bar antennas. *Phys. Rev.*, D90(6):064039, 2014.

[18] Kazunari Eda, Ayaka Shoda, Yuya Kuwahara, Yousuke Itoh, and Masaki Ando. All-sky coherent search for continuous gravitational waves in 6-7 Hz band with a torsion-bar antenna. *PTEP*, 2016(1):011F01, 2016.

[19] Kazunari Eda and Yousuke Itoh. Chi-squared veto in $\mathcal{F}$-statistic-based semi-coherent search for continuous gravitational wave. (in preparation), 2017.

[20] D. R. Lorimer and M. Kramer. *Handbook of Pulsar Astronomy (Cambridge Observing Handbooks for Research Astronomers*. Cambridge University Press, Cambridge, 2012.

[21] Stuart L Shapiro and Saul A Teukolsky. *Black holes, white dwarfs and neutron stars: the physics of compact objects*. John Wiley & Sons, 2008.

[22] N. Chamel and P. Haensel. Physics of Neutron Star Crusts. *Living Rev. Rel.*, 11:10, 2008.

[23] Gordon Baym and David Pines. Neutron starquakes and pulsar speedup. *Annals of Physics*, 66(2):816–835, 1971.

[24] David Pines and Jacob Shaham. The elastic energy and character of quakes in solid stars and planets. *Physics of the Earth and Planetary Interiors*, 6(1):103–115, 1972.

[25] D. I. Jones. Gravitational waves from rotating neutron stars. *Class. Quant. Grav.*, 19:1255–1266, 2002.

[26] C. J. Horowitz and Kai Kadau. The Breaking Strain of Neutron Star Crust and Gravitational Waves. *Phys. Rev. Lett.*, 102:191102, 2009.

[27] Benjamin J. Owen. Maximum elastic deformations of compact stars with exotic equations of state. *Phys. Rev. Lett.*, 95:211101, 2005.

[28] B. Haskell, N. Andersson, D. I. Jones, and L. Samuelsson. Are neutron stars with crystalline color-superconducting cores relevant for the LIGO experiment? *Phys. Rev. Lett.*, 99:231101, 2007.

[29] Matthew Pitkin. Prospects of observing continuous gravitational waves from known pulsars. *Mon. Not. Roy. Astron. Soc.*, 415:1849–1863, 2011.

[30] J. P. Ostriker and J. E. Gunn. On the nature of pulsars. 1. Theory. *Astrophys. J.*, 157:1395–1417, 1969.

[31] S. Bonazzola and E. Gourgoulhon. Gravitational waves from pulsars: Emission by the magnetic field induced distortion. *Astron.Astrophys.*, 312:675, 1996.

[32] M. Zimmermann and E. Szedenits. Gravitational waves from rotating and precessing rigid bodies: simple models and applications to pulsars. *Phys. Rev.*, D20:351–355, 1979.

[33] Curt Cutler and David Ian Jones. Gravitational wave damping of neutron star wobble. *Phys. Rev.*, D63:024002, 2001.

[34] B. Bertotti and A. M. Anile. Gravitational Slowing Down of Solid Spinning Bodies. *Astron. Astrophys.*, 28:429, 1973.

[35] D. I. Jones and N. Andersson. Gravitational waves from freely precessing neutron stars. *Mon. Not. Roy. Astron. Soc.*, 331:203, 2002.

[36] D. I. Jones and N. Andersson. Freely precessing neutron stars: model and observations. *Mon. Not. Roy. Astron. Soc.*, 324:811, 2001.

[37] Bennett Link and Richard I. Epstein. Precession interpretation of the isolated pulsar psr b1828-11. *Astrophys. J.*, 556:392, 2001.

[38] T. V. Shabanova, A. G. Lyne, and J. O. Urama. Evidence for free precession in the pulsar b1642-03. *Astrophys. J.*, 552:321, 2001.

[39] Curt Cutler. Gravitational waves from neutron stars with large toroidal B fields. *Phys. Rev.*, D66:084025, 2002.

[40] Kazuo Makishima, Teruaki Enoto, Junko S. Hiraga, Toshio Nakano, Kazuhiro Nakazawa, Soki Sakurai, Makoto Sasano, and Hiroaki Murakami. Possible Evidence for Free Precession of a Strongly Magnetized Neutron Star in the Magnetar 4U 0142+61. *Phys. Rev. Lett.*, 112(17):171102, 2014.

[41] Kazuo Makishima, Teruaki Enoto, Hiroaki Murakami, Yoshihiro Furuta, Toshio Nakano, Makoto Sasano, and Kazuhiro Nakazawa. Discovery of a 36 ks Phase Modulation in the Hard X-ray Pulses from the Magnetar 1E 1547.0−5408. 2015.

[42] D. I. Jones. Gravitational wave emission from rotating superfluid neutron stars. *Mon. Not. Roy. Astron. Soc.*, 402:2503, 2010.

[43] Kenji Ono, Kazunari Eda, and Yousuke Itoh. New estimation method for mass of an isolated neutron star using gravitational waves. *Phys. Rev.*, D91(8):084032, 2015.

[44] Kazunari Eda, Kenji Ono, and Yousuke Itoh. Determination of mass of an isolated neutron star using continuous gravitational waves with two frequency modes: an effect of a misalignment angle. *J. Phys. Conf. Ser.*, 716(1):012026, 2016.

[45] Greg Ushomirsky, Lars Bildsten, and Curt Cutler. Gravitational waves from low mass X-ray binaries: A Status report. 1999. [AIP Conf. Proc.523,65(2000)].

[46] Lars Bildsten. Gravitational radiation and rotation of accreting neutron stars. *Astrophys. J.*, 501:L89, 1998.

[47] L. Sammut, C. Messenger, A. Melatos, and B. J. Owen. Implementation of the frequency-modulated sideband search method for gravitational waves from low mass X-ray binaries. *Phys. Rev.*, D89(4):043001, 2014.

[48] C. F. Bradshaw, E. B. Fomalont, and B. J. Geldzahler. High-Resolution Parallax Measurements of Scorpius X-1. *Astrophys. J. Lett.*, 512(2):L121, 1999.

[49] B. Abbott et al. Coherent searches for periodic gravitational waves from unknown isolated sources and Scorpius X-1: Results from the second LIGO science run. *Phys. Rev.*, D76:082001, 2007.

[50] J. Aasi et al. Directed search for gravitational waves from Scorpius X-1 with initial LIGO data. *Phys. Rev.*, D91(6):062008, 2015.

[51] Grant David Meadors, Evan Goetz, and Keith Riles. Tuning into Scorpius X-1: adapting a continuous gravitational-wave search for a known binary system. *Class. Quant. Grav.*, 33(10):105017, 2016.

[52] John T. Whelan, Santosh Sundaresan, Yuanhao Zhang, and Prabath Peiris. Model-Based Cross-Correlation Search for Gravitational Waves from Scorpius X-1. *Phys. Rev.*, D91:102005, 2015.

[53] Paola Leaci and Reinhard Prix. Directed searches for continuous gravitational waves from binary systems: parameter-space metrics and optimal Scorpius X-1 sensitivity. *Phys. Rev.*, D91(10):102003, 2015.

[54] C. Messenger et al. Gravitational waves from Scorpius X-1: A comparison of search methods and prospects for detection with advanced detectors. *Phys. Rev.*, D92(2):023006, 2015.

[55] M. Maggiore. *Gravitational Waves: Volume 1: Theory and Experiments*. Oxford University Press, Oxford, 2007.

[56] Piotr Jaranowski and Andrzej Krolak. Data analysis of gravitational wave signals from spinning neutron stars. 2. Accuracy of estimation of parameters. *Phys. Rev.*, D59:063003, 1999.

[57] Piotr Jaranowski, Andrzej Krolak, and Bernard F. Schutz. Data analysis of gravitational - wave signals from spinning neutron stars. 1. The Signal and its detection. *Phys. Rev.*, D58:063001, 1998.

[58] Bruce Allen, Maria Alessandra Papa, and Bernard F. Schutz. Optimal strategies for sinusoidal signal detection. *Phys. Rev.*, D66:102003, 2002.

[59] Curt Cutler and Bernard F. Schutz. The Generalized F-statistic: Multiple detectors and multiple GW pulsars. *Phys. Rev.*, D72:063006, 2005.

[60] Piotr Jaranowski and Andrzej Krolak. Search for gravitational waves from known pulsars using $\mathcal{F}$ and $\mathcal{G}$ statistics. *Class. Quant. Grav.*, 27:194015, 2010.

[61] Karl Wette. Estimating the sensitivity of wide-parameter-space searches for gravitational-wave pulsars. *Phys. Rev.*, D85:042003, 2012.

[62] B. Abbott et al. Setting upper limits on the strength of periodic gravitational waves using the first science data from the GEO 600 and LIGO detectors. *Phys. Rev.*, D69:082004, 2004.

[63] Cristiano Palomba. Simulation of a population of isolated neutron stars evolving through the emission of gravitational waves. *Mon. Not. Roy. Astron. Soc.*, 359:1150–1164, 2005.

[64] B. Abbott et al. Upper limits on gravitational wave emission from 78 radio pulsars. *Phys. Rev.*, D76:042001, 2007.

[65] A. G. Lyne, R. S. Pritchard, and F Graham-Smith. Twenty-Three Years of Crab Pulsar Rotational History. *Mon. Not. Roy. Astron. Soc.*, 265:1003, 1996.

[66] A. G. Lyne, R. S. Pritchard, F Graham-Smith, and F Camilo. Very low braking index for the Vela pulsar. *Nature*, 381:497–498, 1996.

[67] B. Abbott et al. Limits on gravitational wave emission from selected pulsars using LIGO data. *Phys. Rev. Lett.*, 94:181103, 2005.

[68] B. Abbott et al. Beating the spin-down limit on gravitational wave emission from the Crab pulsar. *Astrophys. J.*, 683:L45–L50, 2008. [Erratum: Astrophys. J.706,L203(2009)].

[69] B. P. Abbott et al. Searches for gravitational waves from known pulsars with S5 LIGO data. *Astrophys. J.*, 713:671–685, 2010.

[70] J. Abadie et al. Beating the spin-down limit on gravitational wave emission from the Vela pulsar. *Astrophys. J.*, 737:93, 2011.

[71] Rejean J. Dupuis and Graham Woan. Bayesian estimation of pulsar parameters from gravitational wave data. *Phys. Rev.*, D72:102002, 2005.

[72] Reinhard Prix and Badri Krishnan. Targeted search for continuous gravitational waves: Bayesian versus maximum-likelihood statistics. *Class. Quant. Grav.*, 26:204013, 2009.

[73] Pia Astone, Kazimierz M. Borkowski, Piotr Jaranowski, and Andrzej Krolak. Data analysis of gravitational wave signals from spinning neutron stars. 4. An All sky search. *Phys. Rev.*, D65:042003, 2002.

[74] R. Balasubramanian, B. S. Sathyaprakash, and S. V. Dhurandhar. Gravitational waves from coalescing binaries: Detection strategies and Monte Carlo estimation of parameters. *Phys. Rev.*, D53:3033–3055, 1996. [Erratum: Phys. Rev.D54,1860(1996)].

[75] Benjamin J. Owen. Search templates for gravitational waves from inspiraling binaries: Choice of template spacing. *Phys. Rev.*, D53:6749–6761, 1996.

[76] Patrick R. Brady, Teviet Creighton, Curt Cutler, and Bernard F. Schutz. Searching for periodic sources with LIGO. *Phys. Rev.*, D57:2101–2116, 1998.

[77] Reinhard Prix. Search for continuous gravitational waves: Metric of the multi-detector F-statistic. *Phys. Rev.*, D75:023004, 2007. [Erratum: Phys. Rev.D75,069901(2007)].

[78] Drew Keppel. The multi-detector F-statistic metric for short-duration nonprecessing inspiral gravitational-wave signals. *Phys. Rev.*, D86:123010, 2012.

[79] Drew Keppel. Metrics for multi-detector template placement in searches for short-duration nonprecessing inspiral gravitational-wave signals. 2013.

[80] Reinhard Prix. Template-based searches for gravitational waves: Efficient lattice covering of flat parameter spaces. *Class. Quant. Grav.*, 24:S481–S490, 2007.

[81] J. H. Conway and N. J. A Sloane. *Sphere Packings, Lattices and Groups*. Springer-Verlag, New York/Berlin, 1998.

[82] C. Messenger, R. Prix, and M. A. Papa. Random template banks and relaxed lattice coverings. *Phys. Rev.*, D79:104017, 2009.

[83] Badri Krishnan, Alicia M. Sintes, Maria Alessandra Papa, Bernard F. Schutz, Sergio Frasca, and Cristiano Palomba. The Hough transform search for continuous gravitational waves. *Phys. Rev.*, D70:082001, 2004.

[84] B. Abbott et al. First all-sky upper limits from LIGO on the strength of periodic gravitational waves using the Hough transform. *Phys. Rev.*, D72:102004, 2005.

[85] B. Abbott et al. All-sky search for periodic gravitational waves in LIGO S4 data. *Phys. Rev.*, D77:022001, 2008. [Erratum: Phys. Rev.D80,129904(2009)].

[86] Patrick R. Brady and Teviet Creighton. Searching for periodic sources with LIGO. 2. Hierarchical searches. *Phys. Rev.*, D61:082001, 2000.

[87] Curt Cutler, Iraj Gholami, and Badri Krishnan. Improved stack-slide searches for gravitational-wave pulsars. *Phys. Rev.*, D72:042004, 2005.

[88] M. A. Papa, Bernard F. Schutz, and A. M. Sintes. Searching for continuous gravitational wave signals: The hierarchical Hough transform algorithm. In *Gravitational waves: A challenge to theoretical astrophysics. Proceedings, Trieste, Italy, June 6-9, 2000*, pages 431–442, 2000.

[89] Alicia M. Sintes and Badri Krishnan. Improved hough search for gravitational wave pulsars. *J. Phys. Conf. Ser.*, 32:206–211, 2006.

[90] Vladimir Dergachev. Description of PowerFlux algorithms and implementation. Technical report, LIGO-T050186-00-Z, 2005.

[91] Gregory Mendell and Karl Wette. Using generalized PowerFlux methods to estimate the parameters of periodic gravitational waves. *Class. Quant. Grav.*, 25:114044, 2008.

[92] B.P. Abbott et al. LIGO: The Laser interferometer gravitational-wave observatory. *Rept.Prog.Phys.*, 72:076901, 2009.

[93] T. Accadia et al. Virgo: a laser interferometer to detect gravitational waves. *JINST*, 7:P03012, 2012.

[94] Pau Amaro-Seoane, Sofiane Aoudia, Stanislav Babak, Pierre Binetruy, Emanuele Berti, et al. Low-frequency gravitational-wave science with eLISA/NGO. *Class.Quant.Grav.*, 29:124016, 2012.

[95] Seiji Kawamura et al. The Japanese space gravitational wave antenna: DECIGO. *Class. Quant. Grav.*, 28:094011, 2011.

[96] Masaki Ando, Koji Ishidoshiro, Kazuhiro Yamamoto, Kent Yagi, Wataru Kokuyama, et al. Torsion-Bar Antenna for Low-Frequency Gravitational-Wave Observations. *Phys.Rev.Lett.*, 105:161101, 2010.

[97] Savas Dimopoulos, Peter W. Graham, Jason M. Hogan, Mark A. Kasevich, and Surjeet Rajendran. An Atomic Gravitational Wave Interferometric Sensor (AGIS). *Phys. Rev.*, D78:122002, 2008.

[98] D. Friedrich, M. Nakano, H. Kawamura, Y. Yamanaka, S. Hirobayashi, and S. Kawamura. Juggled interferometer for the detection of gravitational waves around 0.1-10 Hz. *Class. Quant. Grav.*, 31(24):245006, 2014.

[99] Jan Harms and Ho Jung Paik. Newtonian-noise cancellation in full-tensor gravitational-wave detectors. *Phys. Rev.*, D92(2):022001, 2015.

[100] K. Ishidoshiro. *Search for low-frequency gravitational waves using a superconducting magnetically-levitated torsion antenna*. PhD thesis, University of Tokyo, 2010.

[101] Koji Ishidoshiro, Masaki Ando, Akiteru Takamori, Hirotaka Takahashi, Kenshi Okada, et al. Upper Limit on Gravitational Wave Backgrounds at 0.2 Hz with Torsion-bar Antenna. *Phys.Rev.Lett.*, 106:161101, 2011.

[102] Ayaka Shoda, Masaki Ando, Koji Ishidoshiro, Kenshi Okada, Wataru Kokuyama, et al. Search for a Stochastic Gravitational-wave Background using a pair of Torsion-bar Antennas. *Phys.Rev.*, D89:027101, 2014.

[103] Ayaka Shoda. *Development of a High-Angular-Resolution Antenna for Low-Frequency Gravitational-Wave Observation*. PhD thesis, Tokyo U., 2015-03-24.

[104] Ayaka Shoda, Yuya Kuwahara, Masaki Ando, Kazunari Eda, Kodai Tejima, Yoichi Aso, and Yousuke Itoh. Ground Based Low-Frequency Gravitational-wave Detector With Multiple Outputs. 2016.

[105] Curt Cutler. Angular resolution of the LISA gravitational wave detector. *Phys.Rev.*, D57:7089–7102, 1998.

[106] Bernard F. Schutz. Lighthouses of gravitational wave astronomy. 2001.

[107] Linqing Wen and Yanbei Chen. Geometrical Expression for the Angular Resolution of a Network of Gravitational-Wave Detectors. *Phys.Rev.*, D81:082001, 2010.

[108] Y. Guersel and M. Tinto. Near optimal solution to the inverse problem for gravitational wave bursts. *Phys.Rev.*, D40:3884–3938, 1989.

[109] B. Abbott et al. The Einstein@Home search for periodic gravitational waves in LIGO S4 data. *Phys. Rev.*, D79:022001, 2009.

[110] B. Abbott et al. All-sky LIGO Search for Periodic Gravitational Waves in the Early S5 Data. *Phys. Rev. Lett.*, 102:111102, 2009.

[111] B. P. Abbott et al. Einstein and Home search for periodic gravitational waves in early S5 LIGO data. *Phys. Rev.*, D80:042003, 2009.

[112] J. Abadie et al. All-sky Search for Periodic Gravitational Waves in the Full S5 LIGO Data. *Phys. Rev.*, D85:022001, 2012.

[113] J. Aasi et al. Einstein@Home all-sky search for periodic gravitational waves in LIGO S5 data. *Phys. Rev.*, D87(4):042001, 2013.

[114] J. Aasi et al. Application of a Hough search for continuous gravitational waves on data from the fifth LIGO science run. *Class. Quant. Grav.*, 31:085014, 2014.

[115] J. Aasi et al. Implementation of an $\mathcal{F}$-statistic all-sky search for continuous gravitational waves in Virgo VSR1 data. *Class. Quant. Grav.*, 31:165014, 2014.

[116] J. Aasi et al. First low frequency all-sky search for continuous gravitational wave signals. *Phys. Rev.*, D93(4):042007, 2016.

[117] Yuya Kuwahara, Ayaka Shoda, Kazunari Eda, and Masaki Ando. Search for a stochastic gravitational wave background at 1-5 Hz with Torsion-bar Antenna. *Phys. Rev.*, D94(4):042003, 2016.

[118] LIGO Scientific Collaboration. LAL/LALApps: FreeSoftware (GPL) tools for data-analysis. https://wiki.ligo.org/DASWG/LALSuite, LALSuite-6.39 released on 12 October 2016.

[119] Reinhard Prix. The F-statistic and its implementation in ComputeFstatistic_v2. Technical report, LIGO-T0900149-v5, 2011.

[120] Andrzej Krolak, Massimo Tinto, and Michele Vallisneri. Optimal filtering of the LISA data. *Phys. Rev.*, D70:022003, 2004. [Erratum: Phys. Rev.D76,069901(2007)].

[121] Reinhard Prix and John T. Whelan. F-statistic search for white-dwarf binaries in the first Mock LISA Data Challenge. *Class. Quant. Grav.*, 24:S565–S574, 2007.

[122] John T. Whelan, Reinhard Prix, and Deepak Khurana. Improved search for galactic white-dwarf binaries in Mock LISA Data Challenge 1B using an F-statistic template bank. *Class. Quant. Grav.*, 25:184029, 2008.

[123] John T. Whelan, Reinhard Prix, and Deepak Khurana. Searching for Galactic White Dwarf Binaries in Mock LISA Data using an F-Statistic Template Bank. *Class. Quant. Grav.*, 27:055010, 2010.

[124] Kentaro Somiya. Detector configuration of KAGRA: The Japanese cryogenic gravitational-wave detector. *Class. Quant. Grav.*, 29:124007, 2012.

[125] Yoshio Saito. KAGRA location. Technical report, JGW-G1503824-v1, 2015.

[126] S. Miyoki et al. The CLIO project. *Class. Quant. Grav.*, 23:S231–S237, 2006.

[127] Seiji Kawamura. Report of iKAGRA run. Technical report, JGW-G1605294-v1, 2016.

[128] Yuta Michimura. Summary of iKAGRA Run. Technical report, JGW-G1605545-v2, 2016.

[129] LIGO and Virgo collaborations. The Frame Library. http://lappweb.in2p3.fr/virgo/FrameL/, Version 8 released on 17 May 2015.

[130] Hideyuki Tagoshi. Summary of iKAGRA proc data. Technical report, JGW-T1605260-v5, 2016.

[131] Jameson Graef Rollins. Distributed state machine supervision for long-baseline gravitational-wave detectors. *Rev. Sci. Instrum.*, 87(9):094502, 2016.

[132] Yuta Michimura. Summary of iKAGRA Test Run April 2016. Technical report, JGW-T1605177-v3, 2016.

[133] LCGT Special Working Group. Study report on lcgt interferometer observation band. http://gwcenter.icrr.u-tokyo.ac.jp/en/researcher/parameter, 2009.

[134] J. Aasi et al. Directed search for continuous gravitational waves from the Galactic center. *Phys. Rev.*, D88(10):102002, 2013.

[135] Berit Behnke, Maria Alessandra Papa, and Reinhard Prix. Postprocessing methods used in the search for continuous gravitational-wave signals from the Galactic Center. *Phys. Rev.*, D91(6):064007, 2015.

[136] Piotr Jaranowski and Andrzej Krolak. Data analysis of gravitational wave signals from spinning neutron stars. 3. Detection statistics and computational requirements. *Phys. Rev.*, D61:062001, 2000.

[137] Bernard F. Schutz and M. Alessandra Papa. End-to-end algorithm for hierarchical area searches for long duration GW sources for GEO-600. In *Proceedings, 34th Rencontres de Moriond gravitational waves and experimental gravity*, 2000.

[138] Holger J. Pletsch and Bruce Allen. Exploiting global correlations to detect continuous gravitational waves. *Phys. Rev. Lett.*, 103:181102, 2009.

[139] Holger J. Pletsch. Parameter-space metric of semicoherent searches for continuous gravitational waves. *Phys. Rev.*, D82:042002, 2010.

[140] Reinhard Prix and Miroslav Shaltev. Search for Continuous Gravitational Waves: Optimal StackSlide method at fixed computing cost. *Phys. Rev.*, D85:084010, 2012.

[141] David Keitel, Reinhard Prix, Maria Alessandra Papa, Paola Leaci, and Maham Siddiqi. Search for continuous gravitational waves: Improving robustness versus instrumental artifacts. *Phys. Rev.*, D89(6):064023, 2014.

[142] David Keitel and Reinhard Prix. Line-robust statistics for continuous gravitational waves: safety in the case of unequal detector sensitivities. *Class. Quant. Grav.*, 32(3):035004, 2015.

[143] David Keitel. Robust semicoherent searches for continuous gravitational waves with noise and signal models including hours to days long transients. *Phys. Rev.*, D93(8):084024, 2016.

[144] Bruce Allen. A chi**2 time-frequency discriminator for gravitational wave detection. *Phys. Rev.*, D71:062001, 2005.

[145] Y. Itoh, M. A. Papa, B. Krishnan, and X. Siemens. Chi-square test on candidate events from CW signal coherent searches. *Class. Quant. Grav.*, 21:S1667–S1678, 2004.

[146] Llucia Sancho de la Jordana and Alicia M. Sintes. A chi**2 veto for continuous wave searches. *Class. Quant. Grav.*, 25:184014, 2008.

[147] Holger J. Pletsch. Parameter-space correlations of the optimal statistic for continuous gravitational-wave detection. *Phys. Rev.*, D78:102005, 2008.

[148] Yuri Levin and Maarten van Hoven. On the excitation of f-modes and torsional modes by magnetar giant flares. *Mon. Not. Roy. Astron. Soc.*, 418:659, 2011.

[149] A. G. Lyne, S. L. Shemar, and F. Graham Smith. Statistical studies of pulsar glitches. *Mon. Not. Roy. Astron. Soc.*, 315:534, 2000.

[150] Reinhard Prix, Stefanos Giampanis, and Chris Messenger. Search method for long-duration gravitational-wave transients from neutron stars. *Phys. Rev.*, D84:023007, 2011.

[151] Lee S. Finn. Detection, measurement and gravitational radiation. *Phys.Rev.*, D46:5236–5249, 1992.

[152] Curt Cutler and Eanna E. Flanagan. Gravitational waves from merging compact binaries: How accurately can one extract the binary's parameters from the inspiral wave form? *Phys.Rev.*, D49:2658–2697, 1994.